MINISTRY OF EDUCATION AND RESEARCH

TECHNICAL UNIVERSITY
OF CLUJ-NAPOCA, ROMANIA

FACULTY OF ELECTRICAL ENGINEERING

PhD THESIS

Development and performance analysis platform for battery electric vehicles power trains

PhD Student:
Raul Octavian NEMEŞ

PhD Supervisor:
Prof. Dr. Eng Claudia MARŢIŞ

Examination committee:
Chair: Prof. Eng. **Daniel FODOREAN**, Technical University of Cluj-Napoca;

PhD Supervisor: Prof. Eng. **Claudia MARŢIŞ**, Technical University of Cluj-Napoca;

Members:
Prof. Eng. **Elena LOMONOVA**, University of Technology, Eindhoven, The Netherlands;

Prof. Eng. **Fei GAO**, University of Technology of Belfort Montbeliard, France;

Prof. Eng. **Lorand SZABO**, Technical University of Cluj-Napoca, Romania.

– Cluj-Napoca –
2021

str. Memorandumului nr. 28, 400114 Cluj-Napoca, România
tel. +40-264-401200, fax +40-264-592055, secretariat tel. +40-264-202209, fax +40-264-202280
www.utcluj.ro

ACKNOWLEDGMENTS

I would like to express my sincere gratitude to my thesis supervisor Prof. Claudia Steluta MARȚIȘ, for the encouragement, help and financial support. Newertheless, I would like to thank her for the guidance during bachelor and master's degree program.

I would like to express my deepest appreciation, thanks, and gratitude to Lecturer Mircea RUBA, mentor, and friend. I thank him for the encouragement, guidance, and the time he spends with me to share his knowledge.

I wish to thank my colleagues for their support, interesting discussions, and pleasant times we have spent together.

I would like to thank to Siemens Industry Software Brasov for their technical support, Simcenter Amesim software and the good collaboration in URBIVEL and PANDA projects.

This research was financially supported in the frame of the project URBIVEL, "Advanced technologies for intelligent urban electric vehicles", POC-A1-A1.2.3-G-2-15.

Lastly, but most importantly, I am deeply grateful for my family's unconditional, unequivocal, and loving support.

Finally, I would like to thank my girlfriend, Sorina Enachescu, for her support, patience, and encouragement during this time consuming, yet beautiful study.

TABLE OF CONTENTS

ABBREVIATIONS

BiL	Battery-in-the-loop
BMS	Battery management system
CC	Constant current
CMOS	Complementary metal–oxide–semiconductor
CV	Constant voltage
DLL	Dynamic-link library
DMA	Direct memory access
DoD	Depth-of-discharge
DP	Double polarization
ECM	Electrical equivalent circuit model
EIS	Electrochemical impedance spectroscopy
EV	Electric vehicles
FET	Field-effect transistor
FIFO	First-in-first-out
FOC	Field-oriented control
HESS	Hybrid energy storage system
HEV	Hybrid electric vehicle
HiL	Hardware-in-the-loop
IM	Induction machine
IPM	Interior permanent magnet
MiL	Model-in-the-loop
MOS	Metal–oxide–semiconductor
OCV	Open-circuit voltage
OM	Optimal modulus
OSM	Optimum symmetric method
PHEV	Plugged-in hybrid electric vehicle
PiL	Processor-in-the-loop
PMSM	Permanent magnet synchronous machine
PWM	Pulse width modulation
RMSE	Root mean square error
RTMiL	Real-time-model-in-the-loop
SiL	Software-in-the-loop
SOC	States of charge
SoH	State of health
SPM	Surface-mounted permanent magnet
SPWM	Sinusoidal pulse width modulation
SRM	Switched reluctance machine

SVM	Space-vector modulation
TDMS	Technical Data Management Streaming
VI	Virtual instrument
VSI	Voltage source inverter

1. Introduction

The sustainable development, defined as *development that meets the needs of the present without compromising the ability of future generation to meet their own needs* gained a lot of attention in the past few years [1]. In this concept, the sustainable mobility has an important role, 24% of global CO2 emissions being generated by the transportation sector [2].

The replacement of the internal combustion engine-based powertrains with hybrid-electric or electric ones is a complex and competitive challenge for both manufacturers and researchers. The total efficiency of a conventional powertrain is around 20% while for the electric one is about 60%, with an additional benefit of an eco-friendlier solution. However, the drawback of the electric powertrain is the battery as its energy density is about two times lower than the one of gasoline. A potential solution for the power storage system can be a combination of two or more energy storage technologies resulting a hybrid energy storage system (HESS) [3]. The classification of the energy storage systems technology is detailed in fig. 1.1. The electrified propulsion systems are divided in three main categories: hybrid electric vehicles (HEVs), plugged-in hybrid electric vehicles (PHEVs) and electric vehicles (EVs). For the HEVs and PHEVs the powertrain architecture can be series, parallel and series-parallel. Between HEVs and PHEVs the main difference is the battery size/rating and its charging possibility. The focus of this thesis is oriented towards complete electric vehicle-based powertrain analysis.

The main electrical machines considered as lucrative traction solutions in an electric powertrain are the DC machine, induction machine (IM), permanent magnet synchronous machine (PMSM) and switched reluctance machine (SRM) [4, 5, 6].

The DC machine is a good candidate for electric propulsion systems due of its torque-speed characteristics and its simple control. However, the drawbacks of this machine are the low efficiency, bulky construction, regular maintenance due to the mechanical commutator and electromagnetic interferences caused by the commutation process. The induction and synchronous machines drives are replacing the DC drives in traction applications due to the advances in the field of power

semiconductors. The commutatorless motor drives are more attractive for electric propulsion due to the maintenance-free operation and high reliability [5].

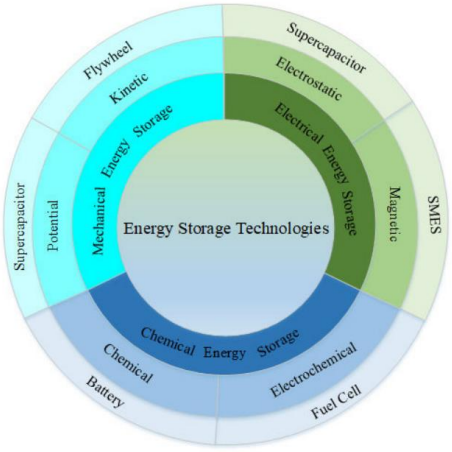

Fig. 1.1. Energy storage classifications [3]

The induction machine is used for EVs and series HEVs where a high-power machine is necessary. The technology for the induction machine production is mature and is relatively cheaper because they have a long production history. Low maintenance and weight are some of the benefits to use these machines in the propulsion systems. The field-oriented control for the IMs is well known and in case of inverter faults the machine is naturally de-excited. At higher speed and lower torque, maximum efficiency is reached as the copper and core losses are minimum. When the machine is operated at low speed, the efficiency drops due to increased rotor losses [7,8,9].

The switched reluctance machine is exceptionally robust with no permanent magnets, suitable for harsh environments operation. Structurally this machine is similar to the stepper motor, the difference being the stator phase currents that are switched function of the rotor position. The main advantages of this machine are the constant power region at extended speed, high efficiency operation at high speed, high power density and its fault tolerant nature. However, the disadvantages are the low power factor and the large acoustic noise [7, 9].

Permanent magnet synchronous machine is used for electric propulsion due to its high torque density and efficiency. Both surface-mounted permanent magnet (SPM) and interior permanent magnet (IPM) types are used for traction applications. Custom control algorithm is required for both configuration and the operating regime covers a wide speed range when flux-weakening operation is implemented [8]. The main disadvantage of this machine is the cost of the permanent magnets. Furthermore, the efficiency is reduced when operating in flux weakening because high d-axis current is needed [10]. Operating at high speeds the core losses are predominant and are increasing rapidly with the speed due to the current applied on d-axis [7].

1.1. Current state of knowledge

A basic powertrain schematic for electric propulsion where a Permanent Magnet Synchronous Machine (PMSM) is used as a traction motor is presented in fig. 1.2. The reference torque for the torque controller is obtained from the driver through the acceleration and braking pedal. This reference is taking into consideration the speed of the motor and the DC link voltage usually supplied by a battery. In the torque control block the reference currents for the d and q axis are computed and input to the current regulators. The references are compared with the measured currents and by appling the modulation technique the gate signals for the inverter are obtained and applied to the inverter feeding the traction motor. The three-phase currents feedback are needed for the current controller. To reduce the total cost of the traction system, an estimation algorithm can be applied for the speed and the position of the motor, resulting a sensorless drive system.

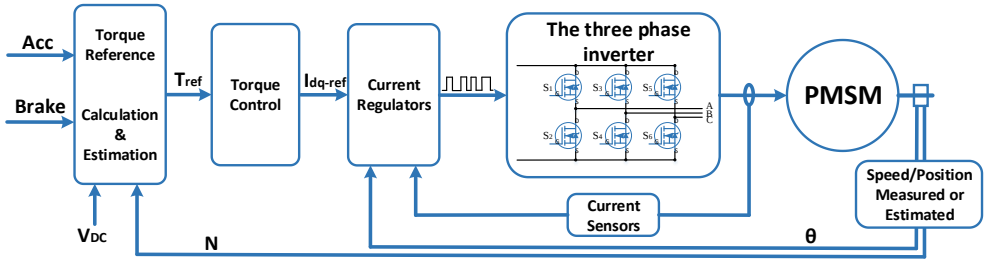

Fig. 1.2. The electric powertrain schematic with PMSM [3]

In the modern electric vehicles, there is a complex connection between mechanical, electric, and electronic components. Therefore, it is essential to test individual components and the subsystems independently in the early stage of the development, before the complete system exists. The researchers have developed the X-in-the-loop (XiL) testing procedure. XiL, where X represents model (M), software (S), processor (P) or hardware (H), are the closed loop testing setups used for the validation of a newly designed system, fig.1.3. A general schematic for an electric propulsion system where XiL can be applied is presented in fig. 1.4

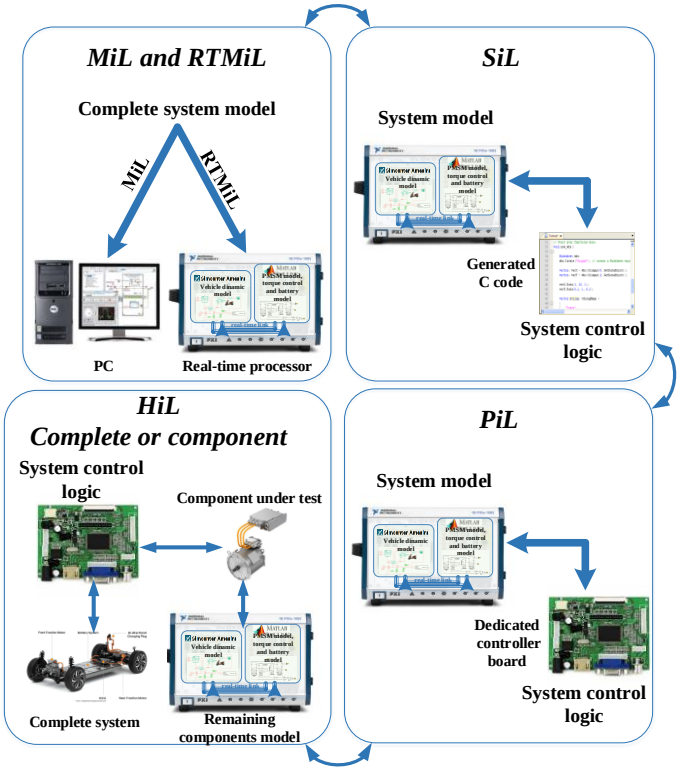

Fig. 1.3. XiL testing setups

The first step for a new system developing process is the model-in-the-loop (MiL) simulation. The complete system is developed using one or more simulation software and the first tests are taking place only in simulation. In this way the system feasibility is tested. For real-time-model-in-the-loop (RTMiL) testing of the system a real-time processor is

used to run the simulation. To model the system, different dedicated software can be utilized and coupled together to run in real-time.

The next level is the software-in-the-loop (SiL) where the controller model is validated and converted in code. In this simulation the controller block is replaced by the generated code and the rest of the model remains the same. Using this approach, one certifies if the control logic can be converted to code as for the real systems only code can be implemented to control the complete system.

In the processor-in-the-loop (PiL) step, the controller model becomes hardware, implemented in an embedded processor or FPGA board. In doing so, a closed loop simulation with the simulated system model and the control board is tested. This step will validate if the hardware used for the controller is capable to correctly operate the simulated system.

The last step is the hardware-in-the-loop (HiL) test. Here the simulated plant model or some of its components are replaced with the actual hardware and tested in different scenarios.

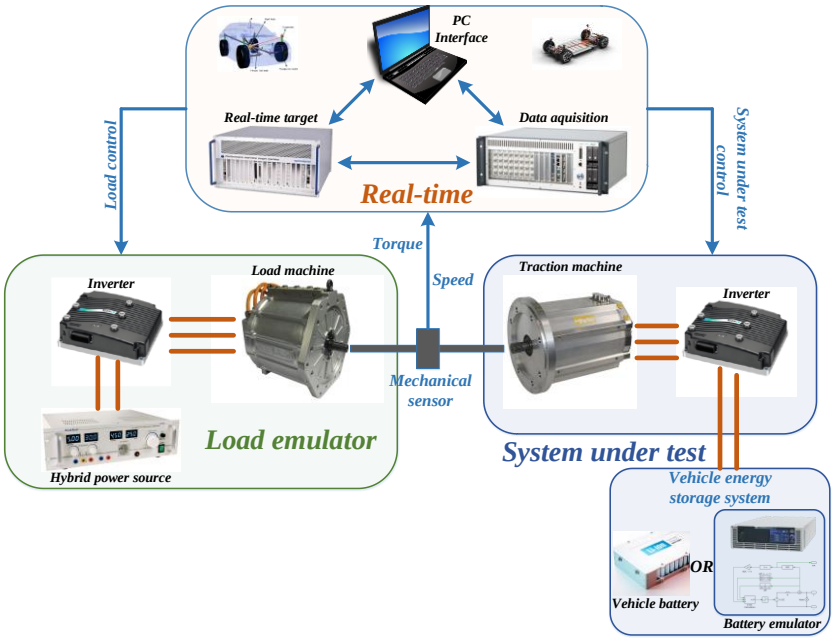

Fig. 1.4. XiL test setup for an electric propulsion system

The MiL testing for the power train of electric vehicles is the first step in the development of a new propulsion system. In many research papers, [11-16], this approach is applied for hybrid or full electric vehicles. The next step in the development process is to run the simulation on real-time processors, RTMiL (17-20). In (21-24) HiL testing is applied to validate the components or the complete propulsion system.

1.2. Objectives of the Thesis

The goal of the thesis is to develop a flexible and complex platform where the electric powertrain for an EV can be tested, using different XiL techniques for different operation scenarios. The flexibility of the platform lies in the ability to switch from real-time simulation to hardware testing of particular components and/or of the complete propulsion unit based on HiL testing.

The powertrain of an electric scooter, based on a PMSM drive, was considered as an application for the testing platform implemented in this work. This machine is an excellent candidate for the electric powertrains as presented in many research papers [7-8, 10].

Custom made assemblies and custom designed electronics add value to the platform offering the user the possibility to range between different types of tests, control algorithms and load scenarios. Seamless transition between hardware and model testing is an added value of the developed platform as well as its internal energy management. The latter is designed in order to test the machine in both motoring and breaking regimes sourcing/sinking power inside the electronic converters. The connection between the electronics and the control board has open-source nature, allowing transition between different brands of control development boards (dSPACE, National Instruments, Typhoon HiL, etc.) up to the designers decision.

1.3. Outline of the Thesis

In Chapter 1 the actual context of transportation electrification is presented. The classification of the energy storages for hybrid-electric or electric vehicles is provided. The electrical machines that can be used in traction applications and their advantages and disadvantages are described. The chapter concludes with the thesis goals.

In Chapter 2 the real-time simulation models are presented and validated. An Amesim model for the electric vehicle is developed and the vehicle parameters are provided. The models of the vehicle drivetrain assemblies are detailed starting with the Li-ion battery cell modelling and cell balancing. Two different models are implemented for the cell and validated through test bench measurements. The cell balancing procedures are presented and a novel active cell balancing technique and circuit is detailed, implemented, and tested on five cells. In the same chapter the model of the three-phase voltage source inverter is presented with its main losses quantified. The mathematical model for PMSM and the field-oriented control strategy with the PI controller's tunning are presented. Finally, the simulated control methods were applied to the real machine and the simulation results are compared with the measured ones proving the proper functionality of the system.

In Chapter 3, the design, building and testing of the HiL platform components are detailed. The chapter starts with the requirements of the three-phase inverter and continues with its design. Following this, the three-phase inverter was built and tested in different configurations and connected to several types of loads. The results are presented and discussed in this chapter. Further on, the cell balancing, and identification circuits are presented. The chapter ends with the vehicle battery unit configuration design.

In Chapter 4, the experimental results are presented and discussed. First, the real-time model in the loop results are analyzed. The hardware-in-the-loop tests are divided in order to test separately the platform components. In the battery-in-the-loop (BiL) setup, the battery of the electric vehicle is tested, and the results are compared with the simulation. The next step was to perform PMSM HiL, where the control

for the traction and load machines are experimentally validated. The chapter continues with the test where the traction motor is supplied by a bidirectional DC power supply used to emulate the real battery. The last test was the complete HiL where all the platform hardware components are connected. Finally, a comparative analysis of the results from RTMiL and HiL are subject of a debate.

Chapter 5 concludes the study and highlights personal contributions and future perspectives.

1.4. Conclusions

The sustainable mobility has an important role in the global strategy for reducing CO2 emissions. The main electrical machines to be used as traction solutions are presented in this chapter. A generic power train architecture is depicted togheter with the approached X-in-the-loop testing procedure. Here X stands for any closed loop testing method. All these setups are described based on a general schematic for an electric propulsion system where XiL can be applied.

REFERENCES

1. C. Perra, "A framework for the development of sustainable urban mobility applications," 2016 24th Telecommunications Forum (TELFOR), 2016, pp. 1-4, doi: 10.1109/TELFOR.2016.7818788.
2. A. Martínez-Navarro, V. -A. Cloquell-Ballester and S. Segui-Chilet, "Photovoltaic Electric Scooter Charger Dock for the Development of Sustainable Mobility in Urban Environments," in IEEE Access, vol. 8, pp. 169486-169495, 2020, doi: 10.1109/ACCESS.2020.3023881.
3. A. Adib et al., "E-Mobility — Advancements and Challenges," in IEEE Access, vol. 7, pp. 165226-165240, 2019, doi: 10.1109/ACCESS.2019.2953021.
4. M. Ehsani, Y. Gao, and A. Emandi, Modern Electric, Hybrid Electric, and Fuell Cell Vehicles: Fundamentals, Theory, and Design, 2nd ed. CRC Press, 2010
5. M. Zeraoulia, M. E. H. Benbouzid, and D. Diallo, “Electric motor drive selection issues for hev propulsion systems: A comparative study,” IEEE Transactions on Vehicular Technology., vol. 55, pp. 1756 – 1764, 2006.
6. A. Emadi, “Transportation 2.0,” IEEE Power and Energy Magazine, vol. 9, pp. 18–29, 2011.
7. S. Williamson, M. Lukic and A. Emadi, "Comprehensive drive train efficiency analysis of hybrid electric and fuel cell vehicles based on motor-controller efficiency modeling," in IEEE Transactions on Power Electronics, vol. 21, no. 3, pp. 730-740, May 2006, doi: 10.1109/TPEL.2006.872388.
8. G. Pellegrino, A. Vagati, B. Boazzo and P. Guglielmi, "Comparison of Induction and PM Synchronous Motor Drives for EV Application Including Design Examples," in IEEE Transactions on Industry Applications, vol. 48, no. 6, pp. 2322-2332, Nov.-Dec. 2012, doi: 10.1109/TIA.2012.2227092.
9. Z. Yang, F. Shang, I. P. Brown and M. Krishnamurthy, "Comparative Study of Interior Permanent Magnet, Induction, and Switched Reluctance Motor Drives for EV and HEV Applications," in IEEE Transactions on Transportation Electrification, vol. 1, no. 3, pp. 245-254, Oct. 2015, doi: 10.1109/TTE.2015.2470092.

10. X. Longya, Y. L. Lurongi, Z. Li, and A. El-Antably, “A new design concept of permanent magnet machine for flux weakening operation,” IEEE Trans. Ind. Appl., vol. 31, no. 2, pp. 373–378, Mar. 1995.
11. S. George, R. V. Chacho and K. Salitha, "Modelling and simulation of Electric Vehicle power train in SEQUEL," 2014 IEEE International Conference on Power Electronics, Drives and Energy Systems (PEDES), 2014, pp. 1-6, doi: 10.1109/PEDES.2014.7042149.
12. S. Yan, Z. Shishun, L. Sujun, Z. Daowei, X. Hui and Y. Gang, "Modeling and Simulation of Modular Hybrid Electric Tactical Vehicle," 2011 Fourth International Conference on Intelligent Computation Technology and Automation, 2011, pp. 834-837, doi: 10.1109/ICICTA.2011.216.
13. K. M. Sidorov, A. G. Grishchenko, B. N. Sidorov and V. I. Stroganov, "Electric Propulsion System Simulation as Basis for the Electric Vehicle Digital Twin Development," 2021 Systems of Signals Generating and Processing in the Field of on Board Communications, 2021, pp. 1-6, doi: 10.1109/IEEECONF51389.2021.9416111.
14. A. M. Omara and M. A. Sleptsov, "Comparative study of different electric propulsion system configurations based on IPMSM drive for battery electric vehicles," 2016 19th International Conference on Electrical Machines and Systems (ICEMS), 2016, pp. 1-6.
15. M. J. Akhtar, R. K. Behera and S. K. Parida, "Propulsion system design of electric vehicle," 2015 6th International Conference on Power Electronics Systems and Applications (PESA), 2015, pp. 1-5, doi: 10.1109/PESA.2015.7398900.
16. M. K. El-Nemr and A. M. Omara, "Design and simulation of a battery powered electric vehicle implementing two different propulsion system configurations," 2016 Eighteenth International Middle East Power Systems Conference (MEPCON), 2016, pp. 877-882, doi: 10.1109/MEPCON.2016.7836999.
17. M. Porru, A. Serpi, A. Floris and A. Damiano, "Modelling and real-time simulations of electric propulsion systems," 2016 International Conference on Electrical Systems for Aircraft, Railway, Ship Propulsion and Road Vehicles & International Transportation Electrification Conference (ESARS-ITEC), 2016, pp. 1-6, doi: 10.1109/ESARS-ITEC.2016.7841438.
18. K. Algarny, A. S. Abdelrahman and M. Youssef, "A novel platform for power train model of electric cars with experimental validation using real-time hardware in-the-loop (HIL): A case study of GM Chevrolet Volt 2nd generation," 2018 IEEE Applied Power

Electronics Conference and Exposition (APEC), 2018, pp. 3510-3516, doi: 10.1109/APEC.2018.8341610.
19. Y. Koraz and M. Youssef, "Rapid Prototyping Testing Technique for Electric Vehicle Propulsion Systems Utilizing Real-Time Hardware in-the-Loop (HIL) Device," 2019 IEEE Conference on Power Electronics and Renewable Energy (CPERE), 2019, pp. 228-231, doi: 10.1109/CPERE45374.2019.8980170.
20. S. Park, J. Yoon, J. Lee and J. Bin, "A study for prediction of propulsion motor performance using HILS(Hardware-In-the-Loop Simulation) system," The 2nd IEEE Conference on Power Engineering and Renewable Energy (ICPERE) 2014, 2014, pp. 181-184, doi: 10.1109/ICPERE.2014.7067208.
21. F. Marignetti, D. D'Aguanno and G. Volpe, "Design and experiments of a test equipment for hybrid and electric vehicle drivetrains," 2017 Twelfth International Conference on Ecological Vehicles and Renewable Energies (EVER), 2017, pp. 1-6, doi: 10.1109/EVER.2017.7935902.
22. J. A. López-Ibarra, H. Gaztañaga, A. S. d. Ibarra and H. Camblong, "Hardware-in-the-Loop Experimental Validation of a Learning based Neuro-Fuzzy Energy Management Strategy for Plug-in Hybrid Electric Buses," 2020 IEEE Vehicle Power and Propulsion Conference (VPPC), 2020, pp. 1-5, doi: 10.1109/VPPC49601.2020.9330911.
23. N. Sharma, Y. Liu, G. Mademlis and X. Huang, "Design of a Power Hardware-in-the-Loop Test Bench for a Traction Permanent Magnet Synchronous Machine Drive," 2020 International Conference on Electrical Machines (ICEM), 2020, pp. 1765-1771, doi: 10.1109/ICEM49940.2020.9270838.
24. T. Transi, P. G. Pereirinha, A. Bouscayrol, M. Degano and A. C. Henao-Munoz, "Hardware-In-the-Loop Emulation of a Small Electric Race Car Using Energetic Macroscopic Representation," 2019 IEEE Vehicle Power and Propulsion Conference (VPPC), 2019, pp. 1-6, doi: 10.1109/VPPC46532.2019.8952276.

2. The Real-time model in the loop system

The models of each assembly of the electric scooter are developed using two dedicated software, Simcenter Amesim and MATLAB/Simulink. In Amesim the electric vehicle dynamics are modelled, while Simulink is used to develop the models for the electric components of the drive train. NI VeriStand is used to couple the two software packages, to run tests as a complete system. In this chapter the developed real-time simulation models are presented, highlighting also the required changes applied to the PC simulation (MiL) models in order to run their analysis on the real-time processor (RTMiL).

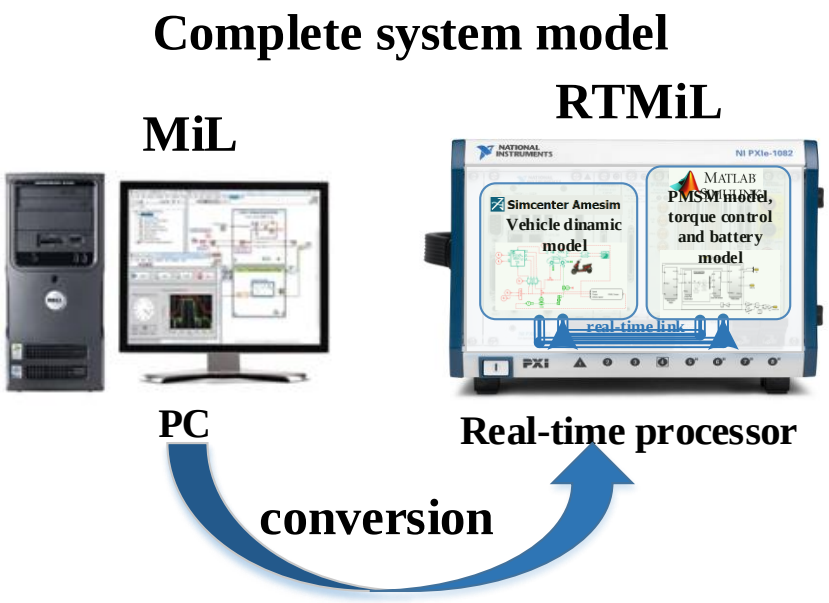

Fig.2.1. The conversion from MiL to RTMiL

2.1. Amesim model for the electric vehicle

In Amesim software the electric vehicle dynamics is implemented as depicted in Fig.2.2, where labels were added to ease the identification of the pictograms. The vehicle submodel contains the aerodynamic and rolling parameters, vehicle mass, wheel, and brake characteristics. The driving cycle is the refence for the driver. This submodel computes the

acceleration, braking control and gear lever used in the vehicle control unit (VCU ELEC) to compute the requested torque from the traction motor needed to maintain the reference speed. This torque signal is connected to VeriStand's interface to become reference to the torque controller in the real-time simulation and the one on the test bench. Either from the simulation or the test bench, the torque developed by the traction motor is transmitted via the interface block as torque signal connected to the rotary mechanical gear ratio. The reducer's speed input is measured using a rotary speed sensor connected to the vehicle control unit and the VeriStand interface. This speed is imposed in the real-time simulation and used as reference speed for the load machine on the test bench. In the same model the road slope, altitude and environmental conditions can be easily set up and adjusted.

To run this model on the real-time processor, some changes in the simulation settings must be accomplished. Fixed step integrator is mandatory while the simulation step must be set to ensure the system stability. Before the real-time file is generated, in the file generation for real-time tab, the platform type is selected to VeriStand.

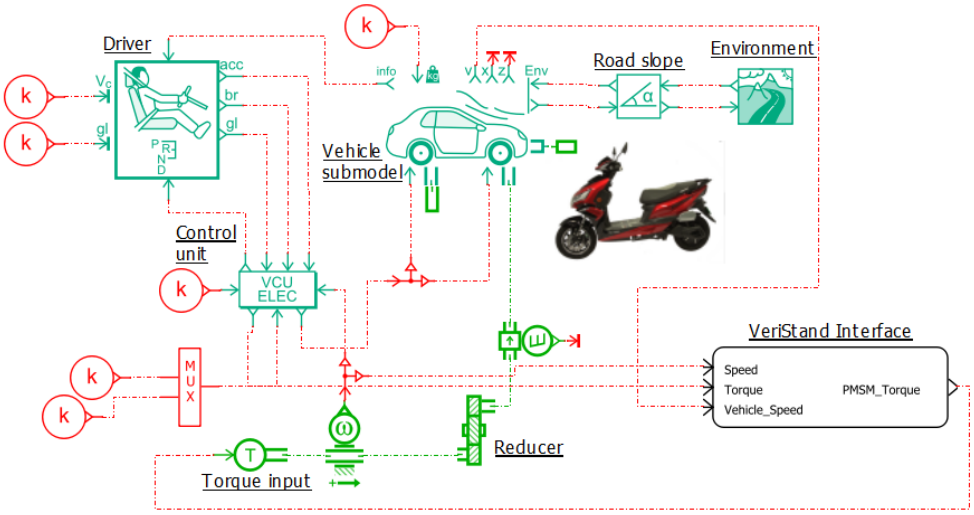

Fig.2.2. Electric scooter dynamic model

The main parameters of the electric scooter are listed up in table 2.1.

Table 2.1. Electric scooter model parameters

Total vehicle mass	250	kg
Rolling resistance coefficient	0.0206	-
Viscous friction coefficient	3.63*e-6	1/(m/s)
Air penetration coefficient	0.7	-
Active area for aerodynamic drag	0.65	m^2
Wheel rim diameter	14 (355.6)	in (mm)
Tire width	100	mm
Max speed	65	km/h
Vehicle range	50	km
Battery power	1.6	kW

2.2. Modelling of the vehicle drive train assemblies

In Fig.2.3 the schematic of the drive train components modelled in Simulink are pointed out. The first section of this subchapter begins by presenting the different types of electrical equivalent circuit models (ECMs) used for the battery cells analysis. Two types of ECMs are treated in detail together with their parametrization procedure. Different balancing circuits are also detailed, differentiated by their functional and design architectures. A novel active cell balancing circuit is implemented, functionally proved by the depicted results. In the second part, the three-phase inverter model with its losses, used to supply the traction motor is detailed. In the last part of the subchapter, the used permanent magnet synchronous machine model, its field-oriented control and PI regulators tunning steps are presented.

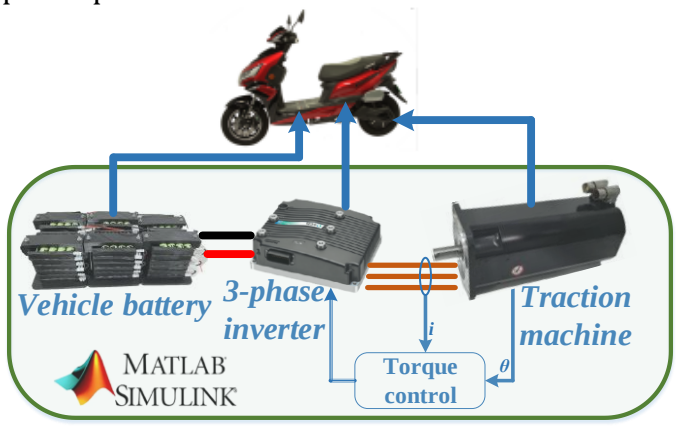

Fig.2.3. Drive train assemblies modelled in Simulink

2.2.1. Li-ion battery cell modelling and cell balancing

The literature presents a large number of different approaches for battery modelling [1-7]. Different physical domains of modelling contain electrical, thermal, electrochemical, or interdisciplinary models, while there are different levels of modeling such as complete system, pack, module or cell. Different approaches of modelling, based on equivalent electrical circuit, empirical, mathematical, or electrochemical impedance spectroscopy models are presented in detail in the review references. Using these types of models, the behavior under various operating conditions can be studied, the battery management system (BMS) can be optimized, and the operating boundaries can be identified. One of the goals of this chapter is to synthesize different approaches of Li-ion cell modelling based on several equivalent electrical circuits. Cell balancing process within an entire battery is key element of the BMS. Multiple cells connected in series become unbalanced, from their voltages' point of view, after a few discharging/charging cycles and the battery capacity decreases. To obtain maximum capacity, as well as for increasing the lifetime of the battery pack, the voltages across all cells must be frequently equalized. Different approaches are presented while one genuine voltage balancing circuit was implemented and tested.

2.2.1.1 Equivalent Electrical Circuit Models for battery cells (ECMs)

Equivalent electrical circuits are used to electrically describe the Li-ion cell's behavior under different operating conditions. ECMs, also referred as Thevenin based electrical models, are composed of voltage sources, resistances and depending on the desired accuracy, different numbers of resistance-capacitor (RC) networks. By using these types of models, the accuracy that describes the electrical performance is high, yelling errors less than 5% [1]. The model's accuracy and the cell voltage are dependent on the resistance-capacitor networks [6-8]. Larger number of RC network in the model will increase its fidelity with the price of longer computation time.

For the parameterization of ECMs for Li-ion cells experimental measurements must be performed. DC current pulses are applied to the Li-ion cell and the voltage variation is measured and recorded; this approach is engaged in this chapter. Another method for parameters

determination is the electrochemical impedance spectroscopy (EIS), presented in detail in [2-5].

Model accuracy can be improved by rigorous parametrizations of the ECMs if DC pulses are applied at different states of charge (SOCs), load currents and ambient temperatures because the cell parameters are dependent on the operating conditions [9, 10]. Using this technique to obtain the parameters for the ECMs, a full parametrization is not possible because at high SOC a high charging current pulse cannot be applied as the maximum cell voltage will be exceeded, the same phenomena will happen if a high discharge pulse is applied when the SOC is low. For an accurate parametrization, if needed, the EIS is used, but in this work the error obtained using DC pulses method was considered satisfactory for the targeted studies.

The Rint Model

The Rint ECM is depicted in fig 2.4. This is one of the simplest circuits, consisting of an ideal voltage source V_{OCV} that defines the cell open-circuit voltage (OCV) function of state of charge (SOC) and the cell resistance R_0. The cell voltage is V_C and I_C is the load current. To increase the model's accuracy, the OCV and cell resistance should take into consideration the temperature and the cell state of health (SoH).

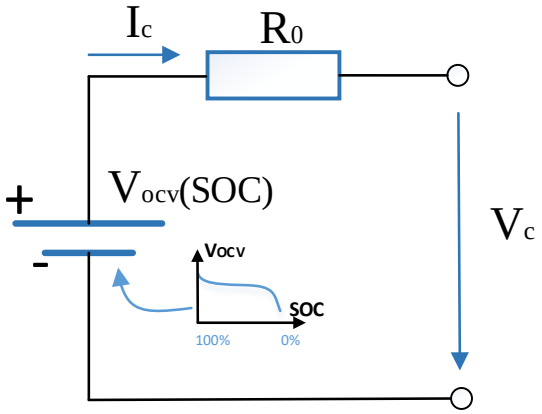

Fig.2.4. Rint electrical equivalent circuit model

$$V_c = V_{OCV}(SOC) - I_c R_0 \quad (1)$$

The RC Model

The RC model is depicted in Fig.2.5, being a topology used for high-power Li-ion batteries. R_0 is the internal cell resistance or, so called terminal resistance. The R_s-C_s components are used to model the electrode surface region while the R_b-C_b ones represents the inside volume of the electrode. The largest electric charge is stored in bulk electrodes so the C_b has a capacity much larger than C_s [11]. The state-space model of the circuit is given in equation (2), with the states u_1 representing the voltage drop on the bulk capacitor (C_b) while u_2 represents the voltage drop on the surface capacitor (C_s).

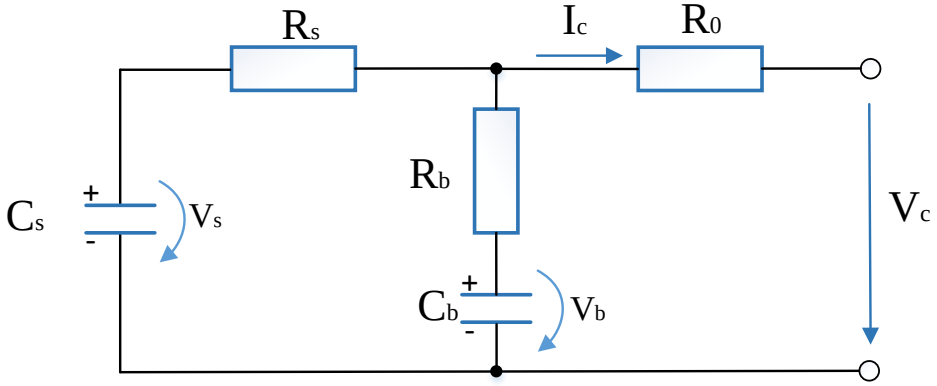

Fig.2.5. RC electrical equivalent circuit model

$$\begin{bmatrix}\dot{u}_1\\ \dot{u}_2\end{bmatrix} = \begin{bmatrix}-\frac{1}{C_b(R_b+R_s)} & \frac{1}{C_s(R_b+R_s)}\\ \frac{1}{C_b(R_b+R_s)} & -\frac{1}{C_s(R_b+R_s)}\end{bmatrix}\begin{bmatrix}u_1\\ u_2\end{bmatrix} + \begin{bmatrix}\frac{-R_s}{C_b(R_b+R_s)}\\ \frac{-R_b}{C_s(R_b+R_s)}\end{bmatrix}[I_c] \quad (2)$$

$$[V_c] = \begin{bmatrix}\frac{R_s}{R_b+R_s} & \frac{R_b}{R_b+R_s}\end{bmatrix}\begin{bmatrix}u_1\\ u_2\end{bmatrix} + \left[-R_0 - \frac{R_bR_s}{R_b+R_s}\right][I_c]$$

The first-order RC model (Thevenin)

The Thevenin model, also called first-order RC model is a Rint model with an additional RC network. In the RC parallel network, R is the polarization resistance and C the polarization capacitance, which describes the transient response of the cell voltage during the charging or discharging process. The open circuit voltage function of SOC is

represented by an ideal voltage source in series with the internal cell resistance by R_0.

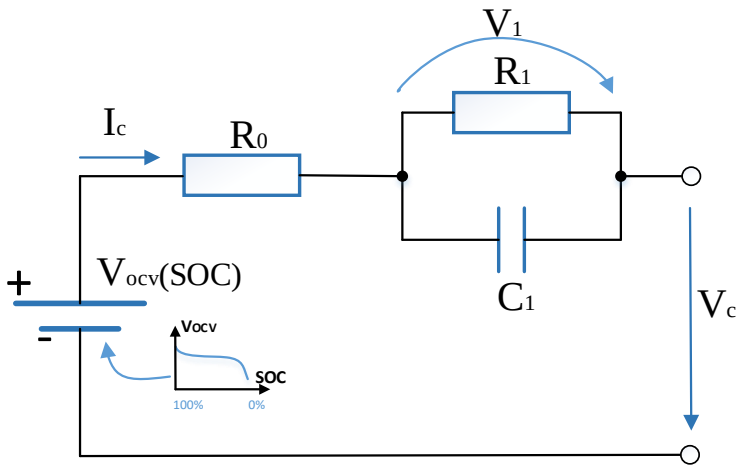

Fig.2.6. First order RC model

The state space model for the circuit is detailed below, where the state parameter u_1 is de voltage drop on the RC network, u_2 is the SOC, and Q is the cell capacity in Ah.

$$\begin{bmatrix}\dot{u}_1\\ \dot{u}_2\end{bmatrix} = \begin{bmatrix}-\frac{1}{R_1 \cdot C_1} & 0\\ 0 & 0\end{bmatrix}\begin{bmatrix}u_1\\ u_2\end{bmatrix} + \begin{bmatrix}\frac{1}{C_1}\\ \frac{1}{Q}\end{bmatrix}[I_c]$$

$$[V_c] = V_{OCV}(u_2) + [1 \quad 0]\begin{bmatrix}u_1\\ u_2\end{bmatrix} + R_0 I_c \tag{3}$$

$$\frac{du_2}{dt} = \frac{I_c}{Q}$$

The second-order RC model (Thevenin based)

The second-order RC model is also known as double polarization (DP) model, as the two RC networks represent the behavior of the activation polarization (R_1, C_1) and the concentration polarization (R_2, C_2) [12, 13]. The RC parallel networks represent the overvoltage behavior during the charging/discharging process and the transient voltage variation during

relaxation [14, 15]. In the present work, the model with two RC networks is considered to be of interest, however more networks can be added, reaching larger order models. By each newly added network, the accuracy of the model is increasing.

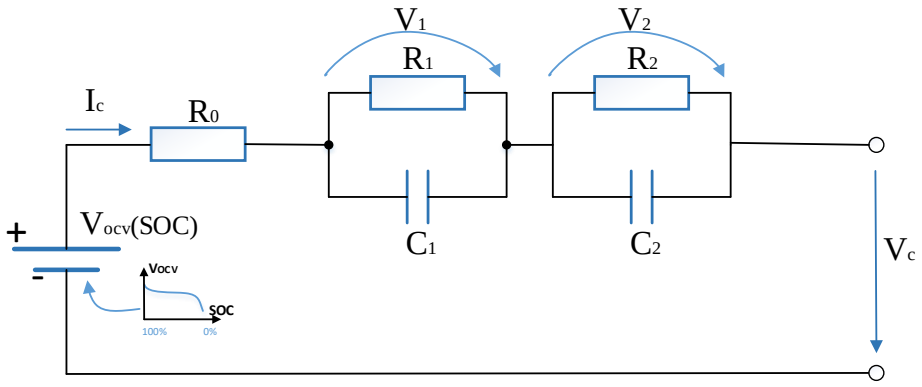

Fig.2.7. Second order RC model

In the state space model, the state u_1 is the voltage drop on the activation polarization network (V_1) and u_2 is the voltage drop on the concentration polarization network (V_2) while u_3 is the cell SOC.

$$\begin{bmatrix}\dot{u}_1\\ \dot{u}_2\\ \dot{u}_3\end{bmatrix} = \begin{bmatrix}-\frac{1}{R_1C_1} & 0 & 0\\ 0 & -\frac{1}{R_2C_2} & 0\\ 0 & 0 & 0\end{bmatrix}\begin{bmatrix}u_1\\ u_2\\ u_3\end{bmatrix} + \begin{bmatrix}\frac{1}{C_1}\\ \frac{1}{C_2}\\ \frac{1}{Q}\end{bmatrix}[I_c] \tag{4}$$

$$[V_c] = V_{OCV}(u_3) + [1 \quad 1 \quad 0]\begin{bmatrix}u_1\\ u_2\\ u_3\end{bmatrix} + R_0 I_c$$

$$\frac{du_3}{dt} = \frac{I_c}{Q}$$

2.2.1.2 Identification Procedure

The electrical equivalent circuit models are parametrized based on test bench measurements carried out on the actual cell under study. The cell engaged is Li-ion NCR18650B manufactured by Panasonic with the specification presented in the table below.

Table 2.2. NCR18650B Li-ion Cell Specification

Rated capacity (20^{0}C)	3200	mAh
Nominal Capacity (25^{0}C)	Min. 3250	mAh
	Typ. 3350	mAh
Nominal Voltage	3.6	V
Charging Method	CC-CV	
Charging Voltage	4.2	V
Charging Current	1625	mA
Min. discharge	2.5	V
Full charge current cut	65	mA

The test bench configuration for the battery cell measurements is depicted in Fig.2.8.

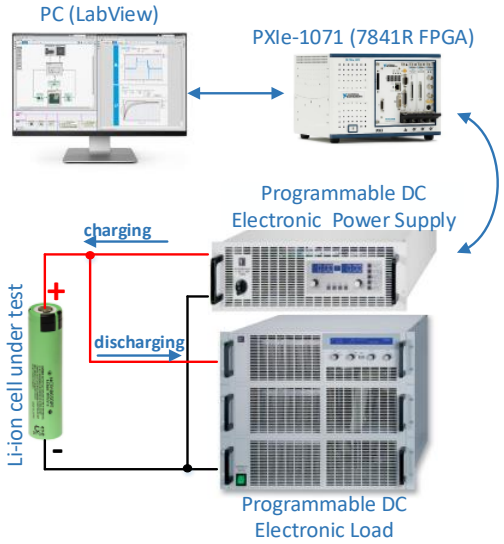

Fig.2.8. Test bench configuration for cell parameters commissioning

For charging the Li-ion cell by applying constant current then constant voltage (CC-CV) method, a programmable DC Electronic Power Supply (EA.PS 8400-70) is used, while for discharging the same cell, a Programmable DC Electronic Load (EA.EL. 9400-150) was engaged. The DC load was controlled using the integrated Analog Interface by the NI PXIe-1071 chassis with the module PXIe-8135 Embedded Controller and FPGA module PXI-7841R. To control the discharge current drained by the electronic load, the embedded controller and the FPGA module was programed using LabVIEW installed on the host computer. It has to be mentioned that all the measurements were carried out at the room temperature. The real-time data acquisition was implemented using the same modules by connecting the current and voltage sensors to the FPGA analog input channels. All the measured data is recorded into a TDMS file (Technical Data Management Streaming) format. The measurements procedure is presented in Fig.2.9.

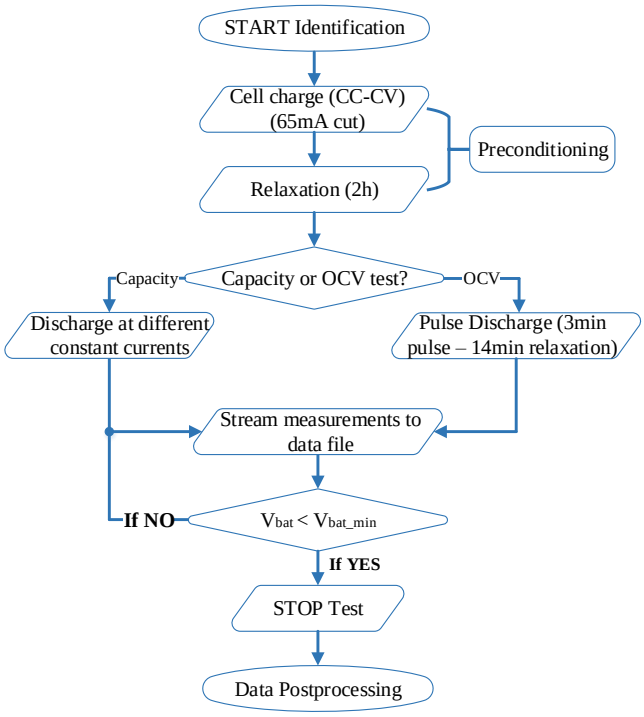

Fig.2.9. The step-by-step measurements procedure

a. In the preconditioning phase, the cell under test is charged first with a constant current (CC), 1625 mA, until the voltage drop between cell and

power supply voltage is high enough to ensure the functionality of the CC method; when this condition is not respected any more, the charging procedure moves to constant voltage (CV) setting 4.2 V as maximum cell voltage. The charging is completed when the cell drains from the supply a current smaller than 65mA. After the charging is finished, a relaxation time of at least two hours is mandatory for the cell to reach the steady state voltage.

b. The cell capacity is one of the most important parameters needed in the ECM, describing cell's energy content mandatory for calculation of the cell state of charge using the Coulomb Counting method [16, 17] also known as current integration method. This method computes the cell state of charge by integrating the current function of time. A drawback of this method is the long-term drift (error) requiring periodical recalibration of the state of charge using different methods. For the identification process, different C discharge rates are applied to fully drain the cell to be able to correctly calculate the capacity. These results are depicted in Fig.2.10. For a cell with a capacity of 3.2Ah, 1C discharge rate means 3.2A discharge current. For the electrical equivalent circuit model, the cell capacity is obtained by calculating the mean value of all the obtained capacity values during measurements.

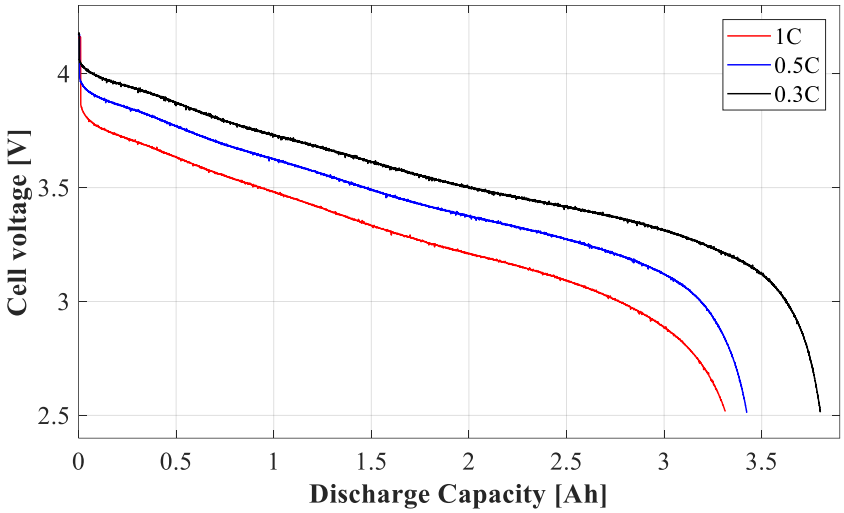

Fig.2.10. Cell Capacity

c. In the current pulse or OCV test, the cell is discharge by repeatedly applying constant current pulses, recording the resulted cell voltage as depicted in Fig.2.11. This test is performed from 100% to 0% SOC, in order to fully parametrize the ECM. The applied current pulses are presented in Fig.2.12.

The discharging current pulses are 3.2A, 1C, applied for 3 minutes followed by a rest period of 14 minutes between pulses. During the 3 minutes the cell is discharged by 5%, repeating the process till the lowest voltage threshold of 2.5V is reached. The cell open circuit voltage is highlighted on the voltage characteristic, Fig.2.11 with blue dots. The OCV is the established cell voltage after the relaxation time, just before the new discharge current pulse is applied. The recorded OCV is the information describing the internal voltage source of the ECM being depending on the cell SOC. The accuracy of the OCV is influenced by the longevity of the relaxation time; larger period will return more accurate open circuit voltage values. Using 15-minute relaxation time, the OCV's error can reach values as low as 0.37% [20].

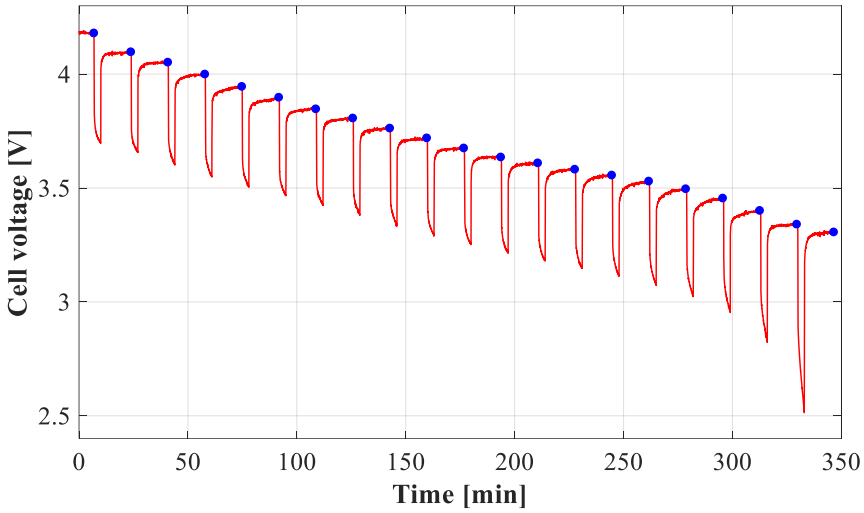

Fig.2.11. Cell voltage for current pulse test

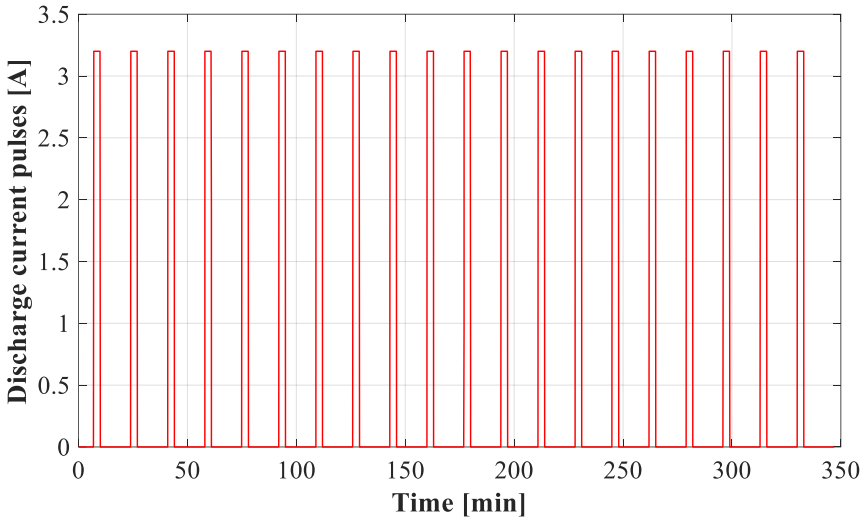

Fig.2.12. The discharging current pulses

2.2.1.3 Electrical Equivalent Circuit Model Parameters Extraction

The ECM parameters are obtained based on the applied current pulses. For each discharge pulse a set of parameters can be obtained and can be saved in a table depending on the SOC. Another approach is to compute only one set of parameters for the whole cell's SOC range. In the present study, the latter method is engaged, being proved in several papers that the reached accuracy is more than satisfactory [18, 19]. Hence, the parameters are fetched at SOC 60%, proved to be the value at which one set of ECM parameters is able to describe the correct cell behavior covering the entire range of SOC.

First-order RC model parameter extraction

The variation of the cell voltage during one discharge current pulse is depicted in Fig.2.13. Using this voltage variation, the ECM parameters can be extracted.

The internal cell resistance R_s is calculated from the instantaneous voltage drop exactly when the current pulse is applied, or it can be

calculated exactly at the end of the current pulse period (when the relaxation period just starts). The parallel resistance is calculated from the voltage variation from the beginning and the end of each current pulse. τ is the pulse period, in seconds, also called polarization time constant.

$$R_s = \frac{V_1 - V_2}{I}$$

$$R_p = \frac{V_2 - V_3}{I} \qquad (5)$$

$$\tau = R_p C_p$$

The voltage variation (Fig. 2.13) in-between the marked points 1 to 3 can be expressed by an exponential function equation (6). In this equation the first parameter describes the instantaneous voltage drop when the discharging pulse is applied (from 1 to 2) while the rest of the equation describes the voltage variation from 2 to 3 expressed by an exponential equation.

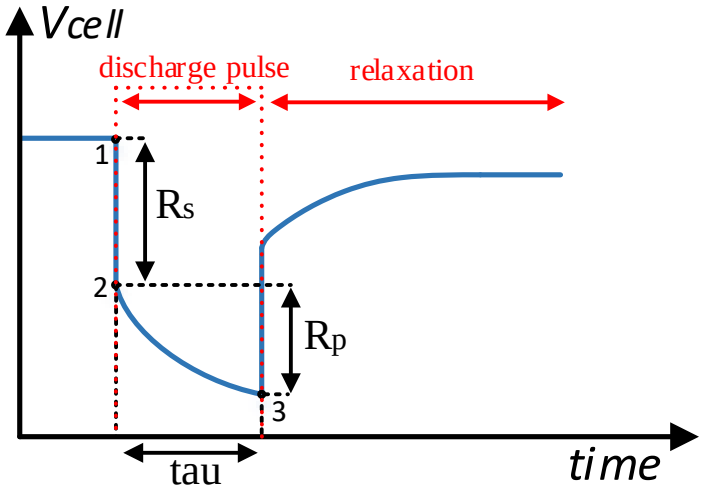

Fig.2.13. First-order ECM parameters identification using the cell voltage variation during one discharge current pulse

$$V_{bat} = k_0 - k_1 e^{-a \cdot t} \tag{6}$$

$$k_0 = V_1 - R_0 I_c \qquad k_1 = \frac{R_1}{I_s} \qquad a = \frac{1}{R_1 C_1} \tag{7}$$

Using MATLAB environment, a curve fitting procedure using a bounded-parameters non-linear least-square algorithm, was applied, where the voltage variation in between points 1 to 3 was fitted by equation (6). In doing so, three unknown parameters, k_0, k_1, and a are computed.

Second-order RC model parameter extraction

The parameters for the second-order ECM are obtained using the same procedure applied for the first-order ECM presented above. In equation (8) the exponential equation which describes the cell voltage variation during the discharge pulse, from points 1 to 3 (the same equation can be used to describe the voltage variation during the rest period, from points 3 to 5) is represented. The smallest error of the results obtained from the second-order ECM compared to experimentally measured results is obtained when the fitting process is applied during the relaxation period.

$$V_{bat} = k_0 - k_1 e^{-a \cdot t} - k_2 e^{-b \cdot t} \tag{8}$$

$$k_0 = V_1 - R_0 I_c \qquad k_1 = \frac{R_1}{I_c} \qquad a = \frac{1}{R_1 C_1} \qquad k_2 = \frac{R_2}{I_c} \qquad b = \frac{1}{R_2 C_2} \tag{9}$$

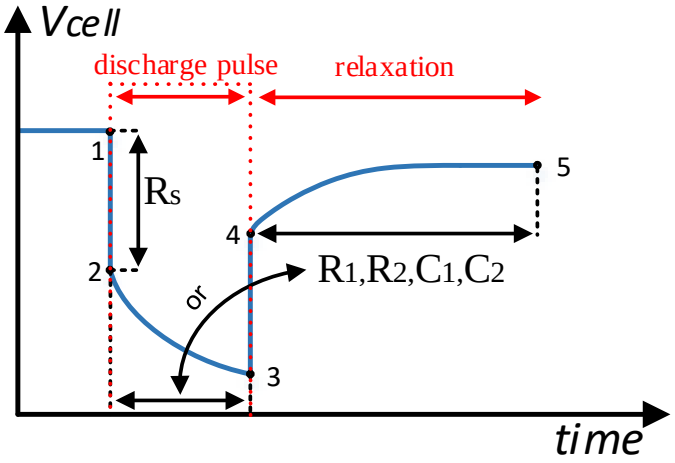

Fig.2.14. Second-order ECM parameters identification based on the voltage variation for one current pulse discharge

2.2.1.4 Model validation

The state-space equations for the ECM for the first and second-order models are implemented in MATLAB/Simulink, equation (3) and (4). In Fig.2.15 the schematic of the ECM implementation in simulation model is presented. The inputs for these models are the electric parameters required by the equivalent circuit and the open circuit voltage, recorded in a look-up table depending on the cell state of charge. The outputs of the ECM are the cell voltage and its SOC.

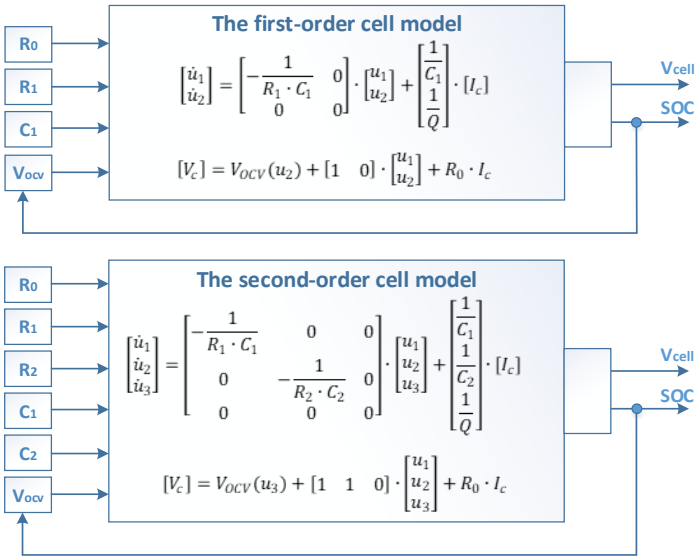

Fig.2.15. Schematic diagram of the ECM implementation in MATLAB/Simulink

To validate the analytical model, the voltage variations caused by the applied discharge pulses are compared for both simulation models (first and second order ECMs) versus experimental measurements (see Fig.2.16).

The best fidelity is obtained for the second-order equivalent circuit model.

The constant current pulse discharging procedure is performed from 100% to 0% SOC in order to extract the open circuit voltage depending on the cell SOC, however, the cell is operated usually from 90% to 10% to protect it from over-charging and over-discharging. To highlight the discharge percent relative to the capacity, the term depth-of-discharge (DoD) is used. The EV cell has a typical DoD of 70-80%, due to cycling it from 90% to 10%, in doing so, increasing its service life. If this DoD is used to cycle the cell, the first two and the last two discharging pulses are not taken into consideration, thus the absolute error is less than 0.05V for both models.

For a better comparison of the two ECMs, the root mean square error (RMSE) is calculated, using equation (10), where T is the time period.

$$RMSE = \sqrt{\frac{1}{T}\int_0^T [V_{meas}(t) - V_{sim}(t)]^2 dt} \tag{10}$$

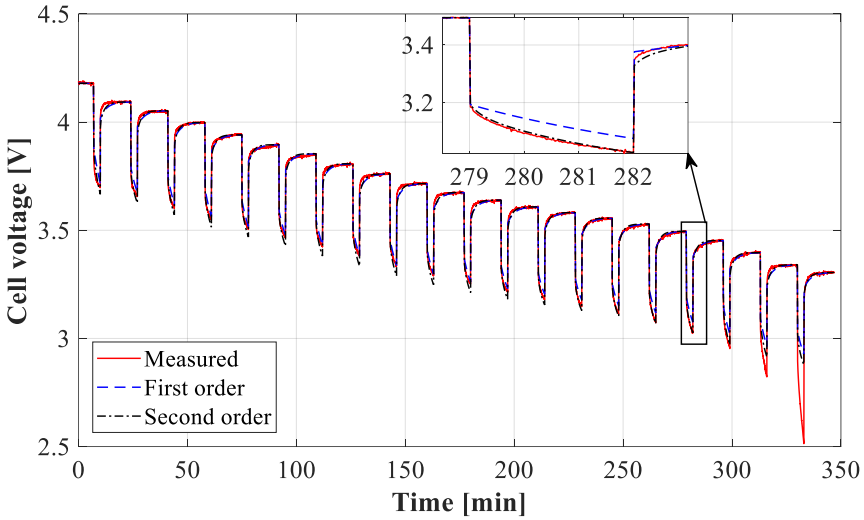

Fig.2.16. Cell voltage variation during discharge pulses for simulation

(first and second order ECMs) versus measured data

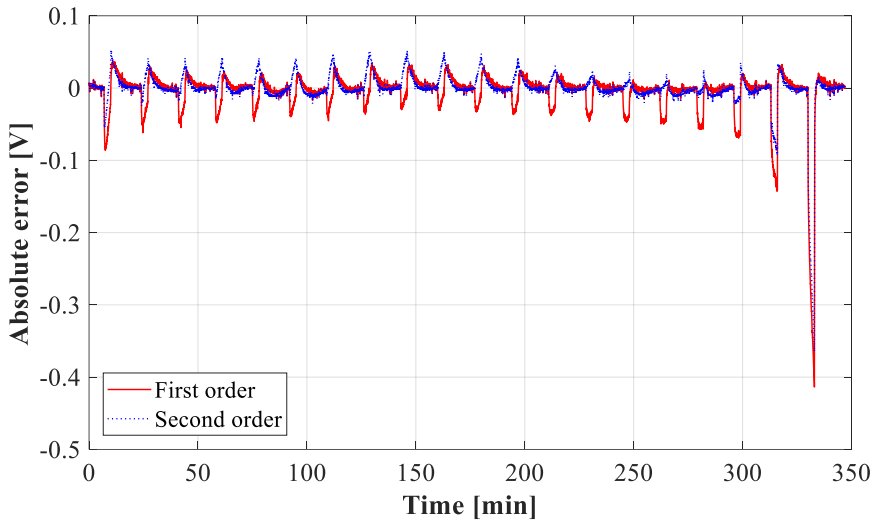

Fig.2.17. The absolute error for the first and second order ECM

The results of the RMSE for the first-order ECM is 34.3 mV for the full cycle and 14.6 mV for 80% DoD. The error for the second-order ECM is approximatively 25%, less compared with the error from the firs-order ECM, with 27.65 mV full range and 11.07 mV from 90-10% SOC.

2.2.1.5 Battery Management System

The battery management system (BMS) is a fundamental component of the energy storage system where rechargeable battery cells are used [23]. The main role of this system is to protect the cell for overcharging and under discharging, prolong its life, protect its users and estimate different cell states such as the state of charge (SOC), state of health (SOH) and power capability. The BMS requires voltage monitoring of each cell and current measurement to be able to estimate the SOC and the SOH. Temperature sensors are used to avoid thermal runaway or lithium plating [24].

In this chapter different passive and active cell voltage balancing procedures and their corresponding circuits are presented. The central interest in this section of the thesis is a novel circuit proposed by the author for active cell balancing. This circuit's operational concept is

tested and proved using five unbalanced Li Ion cells. The obtained results are presented to highlight the circuit's performances. The balancing procedure's flowchart was implemented in LabVIEW and loaded on the NI PXIe-8135 Embedded Controller. For the voltage measurements analog inputs are used, while the circuit's relays (see Fig.2.21) are controlled with digital output ports. The voltage source is controlled via analog output ports of the NI PXI-7841R R Series FPGA. The acquired measurements data from the FPGA are transmitted through a FIFO (first-in-first-out) to the real-time processor where the measurements are logged in a Technical Data Management Streaming (TDMS) file format.

Passive cell balancing

In passive cell balancing method, the excess energy from the cells with the highest voltage is dissipated as heat resulting in a low efficiency balancing method. This method is best suited for low current charging/discharging rates.

The simplest cell balancing circuit is depicted in Fig.2.18. In this topology for each cell, there is a dissipative resistor in parallel. The circuit can operate in two modes: continuous and detecting. In the first mode all switching elements are controlled by the same signal. When charging, all will be turned on and the cell with the highest voltage will have less charging current than the cell with lower voltage. The advantage of this method is the simplicity of the implementation and control. In detecting mode, each cell voltage is monitored, and the balancing controller decides if the dissipative resistor should be activated or not [21].

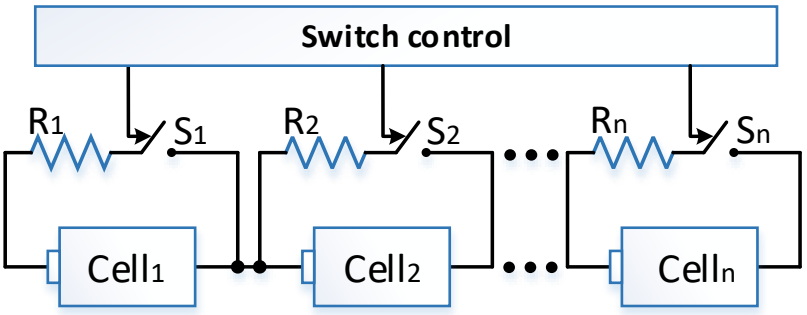

Fig.2.18. Passive balancing using dissipative resistor

Active cell balancing

In active cell balancing technique, the accumulated power is redistributed between cells during the charge or discharge process, resulting a more complex balancing technique. Each cell voltage in the battery pack is monitored in order to perform the balancing procedure. The simplest mode to redistribute the energy is to use capacitors, the circuit being depicted in Fig.2.19 In the literature there is a variety of circuits topologies that can be used for active cell balancing, such as buck-boost converter, flyback converter-based cell balancing circuit, switched transformer or multi-winding transformer [21].

Switched Capacitor based balancing circuit

The switched capacitor based balancing circuit is shown in Fig.2.19. Using the external storage device, in this circuit the capacitors are engaged to transport the energy from the cell with the highest voltage to the one with the lowest voltage [21]. For example, if cell 1 has higher voltage than cell 2, the C1 capacitor is charged by placing it in parallel with cell 1 connecting S1 and S2 switches accordingly. After the capacitor is charged the switches are controlled to connect the capacitor in parallel with cell no.2 to shuttle the energy from the first to the second cell.

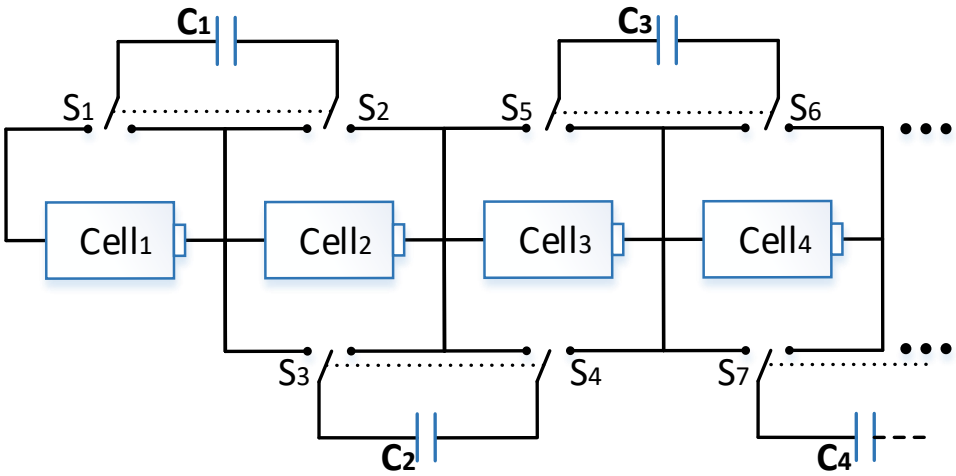

Fig.2.19. The switched capacitor balancing circuit

The shunt inductor circuit topology

The shunt inductor balancing circuit is operating based on two steps. During the first step, the cell with the highest voltage is detected and is connected in parallel with the inductor by controlling the corresponding switches. In doing so, the energy is transferred from the cell to the inductor. During the second step, the previously activated switches are opened and the main SWa and SWb are closed, driving the energy stored in the inductor to the entire pack. This type of balancing is also called cell-to-pack balancing circuit due to the energy transfer philosophy from the cell with the highest voltage to the entire pack [22].

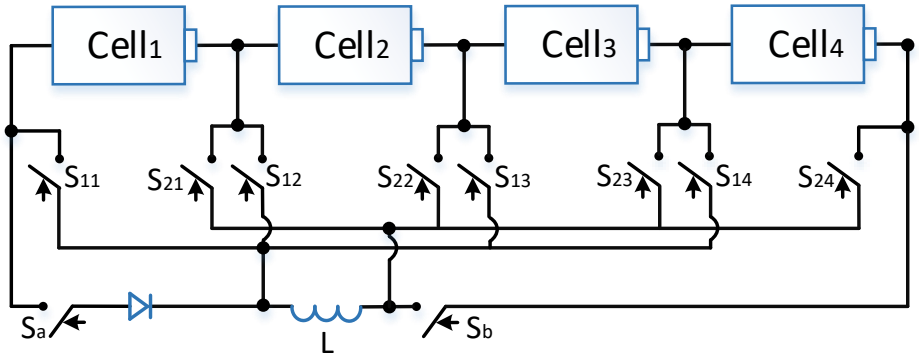

Fig.2.20. Shunt inductor balancing circuit

The switched cells during charging circuit topology

A new approach of cell balancing based on switching cells during charging is implemented and tested. For charging and balancing the cells a controlled voltage source is used where the output current is imposed by the charging/balancing controller. In Fig.2.21 the switched cell during charging active balancing circuit architecture is depicted. To charge each cell at a time the polarity of the DC bus must be changed depending on which cell needs to be connected to the voltage source. This decision is handled by controller. The DC bus is represented with two thick black lines. An H-bridge configuration is used to change the polarity, using two relays with normal open (NO) and normal closed (NC) contacts. On default mode, when the relays coils are not energized the top DC buss is the positive polarity and only the odd cells can be charged. To charge the even cells, the H-bridge relays are activated, thus the DC bus polarity is

reversed. Now the controlled voltage source can be connected to charge the cells.

The flow-chart of the balancing procedure using the switched cells during charging circuit is depicted in Fig.2.22. For the implementation of the balancing logic, each cell's voltage is measured. The balancing strategy starts by charging the complete battery pack with a current of 2.5 A until one of the cells reaches the maximum threshold voltage. The latter is set to 4.2V. After this step, the current is decreased and applied again to the pack. The applied current values are decreased in the following sequence: 2, 1.5, 1, 0.75 A. If one cell reaches the maximum cell voltage when the applied charging current to the entire pack is 0.75 A, that cell is considered fully charged and only the rest of the cells are now charged with the same current (0.75A) till those reach 4.2V. If any of cells 1,2 4 or 5 reaches the maximum threshold voltage, then the remaining ones can be grouped in formations of 3-cells to be charged at 0.75A current. The process is stopped when any of them reaches the established threshold voltage. The last step consists in connecting the remaining cells one by one to the controlled voltage source to be charged with the constant current until all reach the maximum voltage threshold. These first steps of charging/balancing the battery cells are called raw charging process. Immediately after this process, a relaxing period of 10 minutes is applied before passing towards the fine charging process.

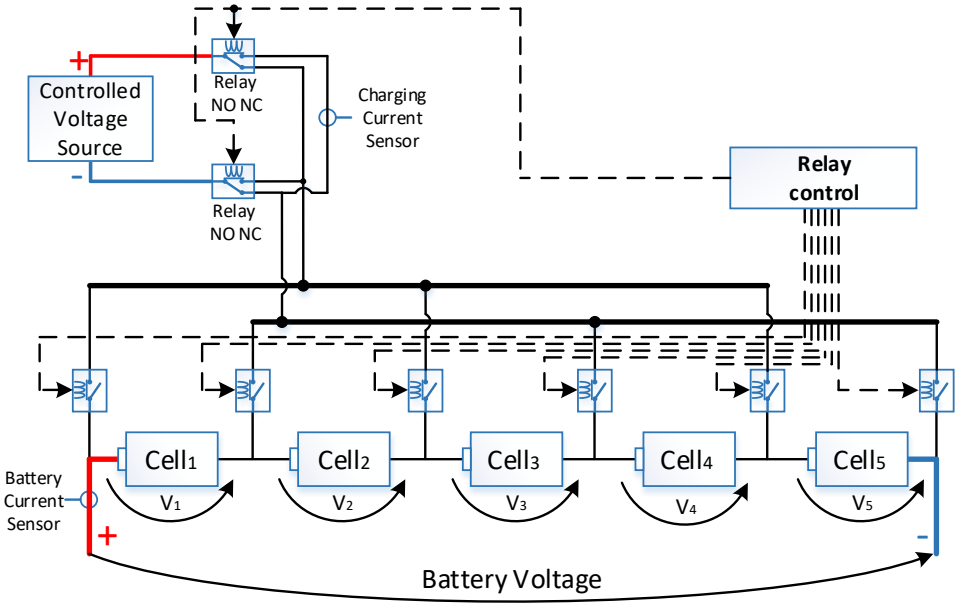

Fig.2.21. The switched cells during charging balancing circuit architecture

During the fine charging/balancing procedure, the same logic is applied as presented above using lower current values such as: 0.7, 0.5, 0.35, 0.3 and 0.2A. Then the last cell reaches the maximum voltage during charging at 0.2A (the lowest current). It is considered that all the cells are charged, and their voltage is equalized, hence both the charging and the balancing processes are finished.

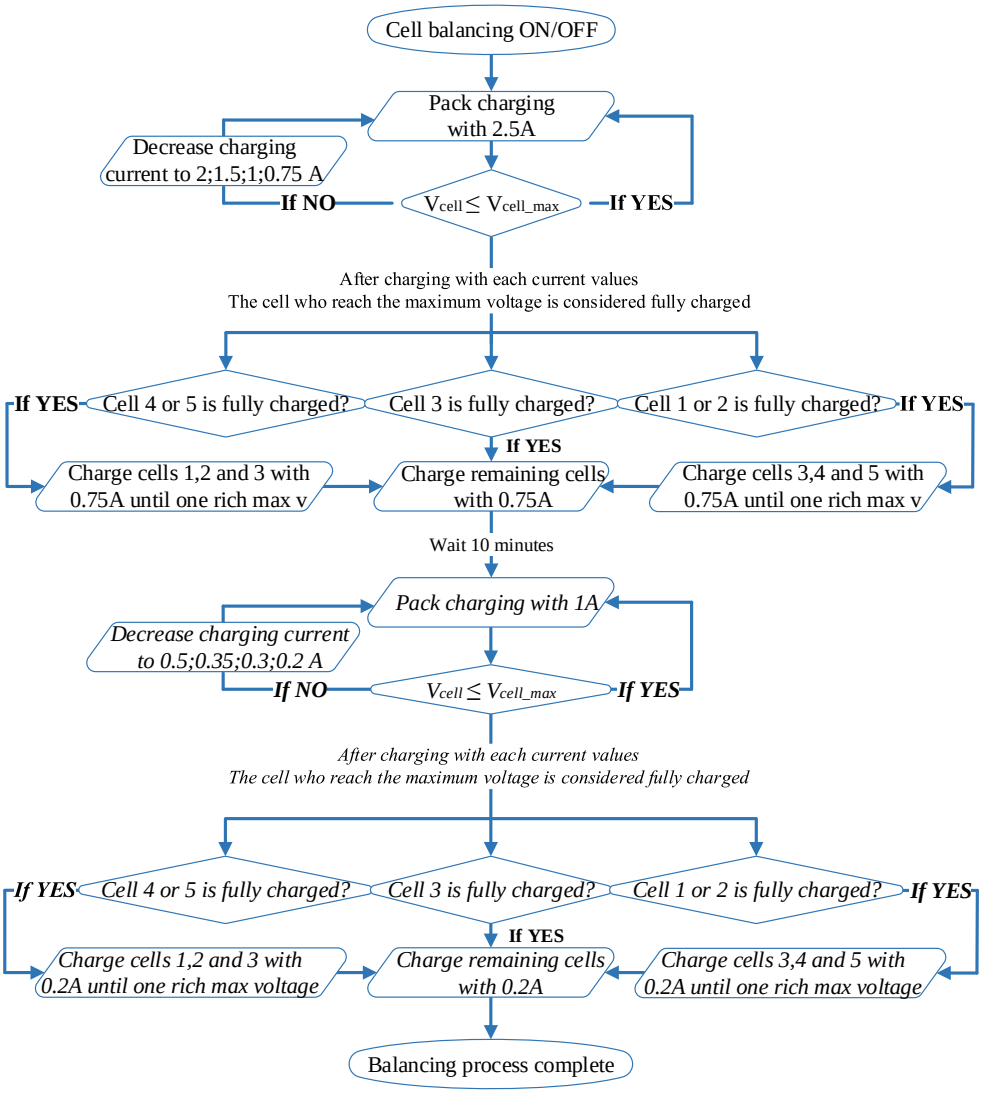

Fig.2.22. The schematic diagram of the rule-based balancing procedure

Experimental validation of the switched cells during charging active balancing circuit

Each cell's voltage was measured using operational amplifiers connected to the analog input ports of the NI PXI-7841R R Series FPGA. The cell voltage was calculated as mean value during ten-time samples, to reduce the measurement noise. The charging current is measured with a current transducer LA 55-P from LEM. This sensor is used because it

incorporates galvanic separation between its primary and secondary circuit. Its output is connected to an analog input port of the FPGA previously mentioned. In LabVIEW a project was created using direct memory access (DMA) and first-in-first-out (FIFO) data structures, the latter being used to transfer data between a FPGA processor and the real-time processor or the host computer. After the DMA FIFO was created, in LabVIEW FPGA a virtual instrument (VI) block diagram was used to write the measurement data into the buffer. The manipulated data type must be fixed-point to be compatible with the requirements of the FPGA. On the real-time processor a LabVIEW VI block diagram was uploaded to read the data from the Host Buffer. In the same VI, the human interface was created plotting the measurement data on a graph. For further analysis of the results, a TDMS type file was created in which the acquired data was saved.

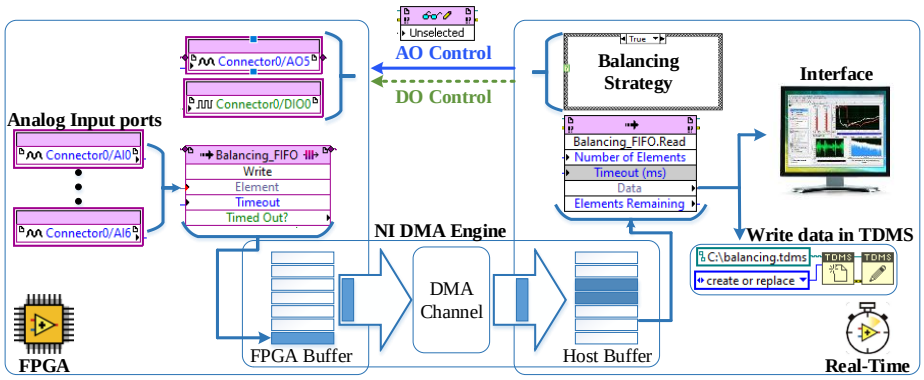

Fig.2.23. LabVIEW implementation of the balancing strategy

In Fig.2.22 the balancing strategy is presented as a diagram being divided in different cases. This strategy was implemented in the real-time LabVIEW VI using Case Structure programing sequence. The input of this structure is the case selector, which selects the case to be executed. This selection is performed based on the measured cell voltages. In each of the different cases the relays of the balancing circuit are triggered using digital output ports of the FPGA. The boolean signals are transmitted from the real-time VI to the FPGA VI using a read/write control function. This function can access a control or indicator instrument from the VI running on the FPGA target. The analog data from the balancing strategy is transmitted in the same manner but converted in fixed-point data type. The analog data is used to set the controlled voltage source used to

charge and balance the cells. The used hardware source is ELEKTRO-AUTOMATIK EA-PS 8400-70, controlled through the analog interface while the output power, current and voltage are adjusted by the analog signals imposed by the FPGA via its analog output ports.

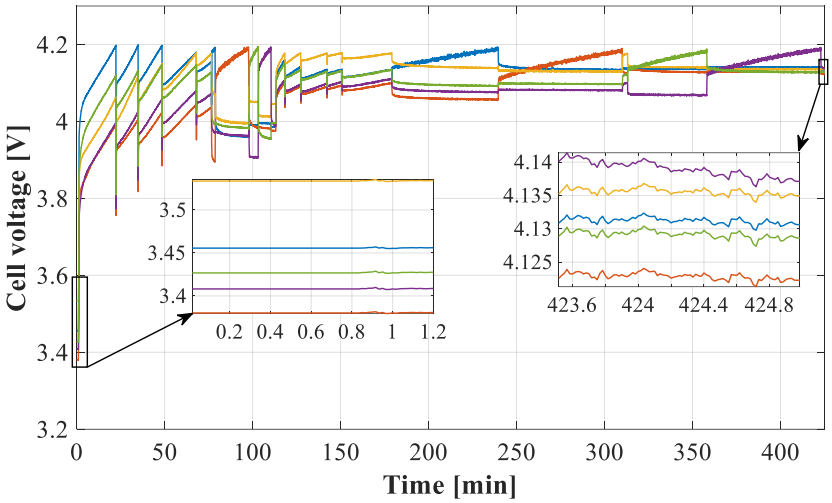

Fig.2.24. The 5 cells voltage variations during the balancing process

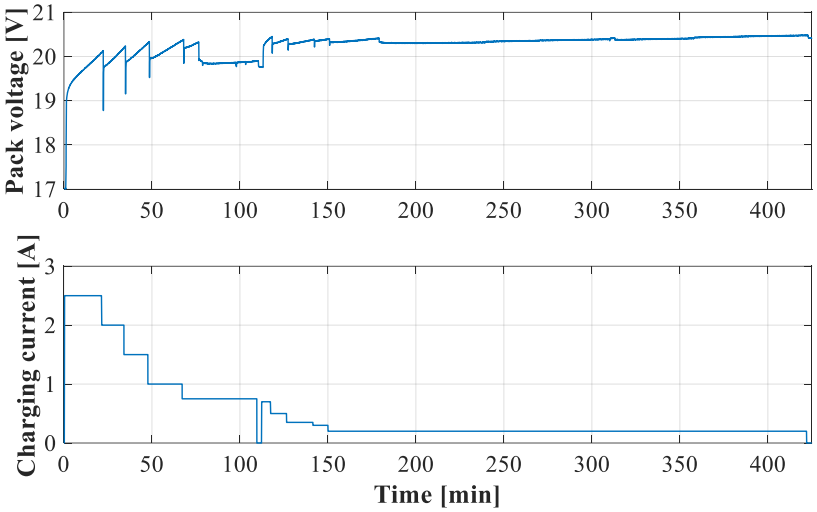

Fig.2.25. The battery pack voltage and the applied charging current

Each of the 5 cells voltages variation is presented in Fig.2.24. When starting the balancing process, the difference between the cell with the highest and lowest voltage is 0.154V. The rule-based balancing strategy is applied and by its end the difference is mitigated to 0.0145V. At this point the cells are considered balanced. In Fig.2.25 the battery pack voltage and the charging current are presented.

2.2.2. Three-phase voltage source inverter model

In AC drives the voltage source inverters (VSI) are used to supply the machine with variable voltage and variable frequency obtained from the DC supply. Different modulation techniques can be applied to the inverter. The most popular ones are the sinusoidal pulse width modulation (SPWM) and space-vector modulation (SVM) [25]. In this thesis SPWM was implemented. The three-phase voltage source inverter is presented in Fig.2.26. Power MOSFET's are used as switching elements.

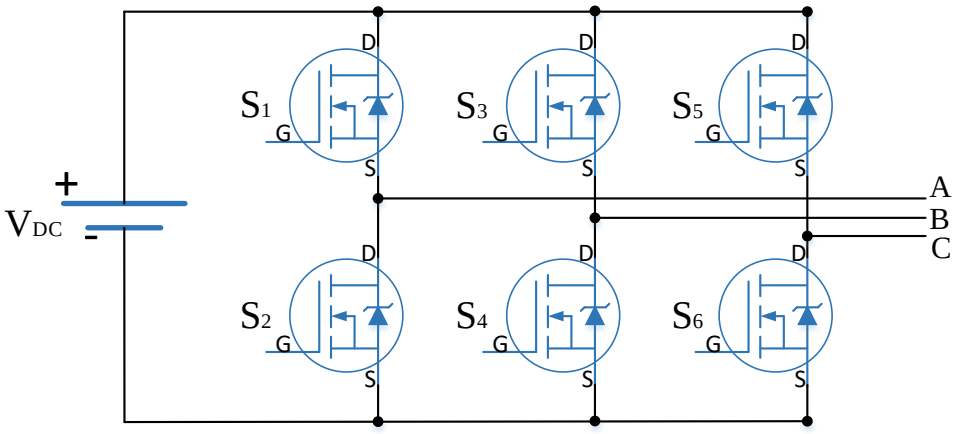

Fig.2.26. Three phase invert topology

The output frequency of the voltage is given by the reference signal frequency. The modulation index is the ratio calculated between the reference signal, also called modulated wave, and the carrier signal. If the modulation index exceeds 1, over modulation occurs and a special control strategy must be implemented. In this implementation, the overmodulation zone is not reached. In Fig.2.27 the SPWM waveform

generation is presented. The top signal is the carrier, while the bottom one is the reference or modulated wave. These two signals are continuously compared. When the carrier is lower than the reference signal the PWM output is ON, otherwise is OFF. If this reference signal is the voltage for phase A, the switch S1 is ON and complementary, S2 is OFF while the carrier is lower than the sinusoidal wave, otherwise S1 is OFF and S2 is ON.

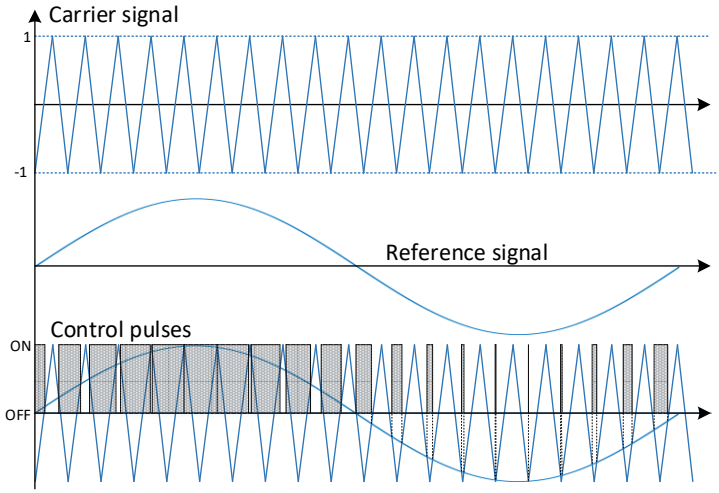

Fig.2.27. Sinusoidal PWM

The phase-to-neutral voltage equations are presented below. These equations are implemented in MATLAB/Simulink to model a three-phase inverter [26]. The maximum output phase-to-neutral voltage is VDC/2 for the SPWM.

$$v_a(t) = \frac{V_{DC}}{3}(2S_A - S_B - S_C)$$

$$v_b(t) = \frac{V_{DC}}{3}(2S_B - S_A - S_C) \qquad (11)$$

$$v_c(t) = \frac{V_{DC}}{3}(2S_C - S_A - S_B)$$

Three-phase inverter losses

The main power losses in any three-phase inverter are due to the MOSFETs and reverse diodes. The power loss in a MOSFET is divided into two categories: switching and conduction losses. For the reverse diode the total losses consist of conduction, switching and reverse leakage losses. The conduction losses are dependent on the duty cycle and the switching frequency [27]. MOSFET power losses are described in equation (12). The MOSFET parameters engaged in the calculations are labeled and valued in Table 2.3. These are obtained from the datasheet of the IRFP4668PbF used to build the actual inverter for the test bench. The current through the MOSFET is denoted by i_M being the rms value for one phase.

$$P_{loss\_M} = P_{conduction\_M} + P_{switching\_M}$$
$$P_{conduction\_M} = {i_M}^2 R_{ds} D \tag{12}$$
$$P_{switching\_M} = \frac{V i_M}{2}\left(T_{on} + T_{off}\right)F_{sw} + C_{oss}V^2 F_{sw}$$

Table 2.3. The IRFP4668PbF parameters from the datasheet

Drain to source resistance	Rds	0.008	Ω
Forward voltage	V	20	V
Turn on time	Ton	41e-9	s
Turn off time	Toff	64e-9	s
Switching Frequency	Fsw	10	kHz
Output Capacitance	Coss	810e-12	F
Duty cycle (mean)	D	0.5	-

For the reverse diode, the losses are computed using equation (13) and its parameters are listed in Table 2.4.

$$P_{loss\_D} = P_{conduction\_D} + P_{reverse\_D} + P_{switching\_D}$$

$$P_{conduction\_D} = i_f V_f D$$
$$P_{reverse\_D} = i_r V_r (1 - D) \quad (13)$$
$$P_{switching\_D} = \frac{T_{rr} i_{rrm} V_r F_{sw}}{2}$$

Table 2.4. IRFP4668PbF diode parameters

Forward voltage drop	V_f	1.3	V
Reverse voltage	V_r	20	V
Reverse Leakage current	i_r	0.00025	A
Reverse Recovery Time	T_{rr}	135e-9	s
Max Recovery Current	i_{rrm}	8.7	A
Output Capacitance	C_{oss}	810e-12	F
Duty cycle (mean)	D	0.5	-

2.2.3. Permanent magnet (non-salient pole) synchronous machine analysis and control

The electrical machine considered as the solution for the light EV under study in this thesis is a PMSM. For propulsion applications, both interior and surface-mounted permanent-magnet configurations can be adopted. Compared to other types of machines, permanent-magnet (PM) machines have larger torque density and higher efficiency [28, 29]. AC machines are usually controlled via two methods: scalar and vector control. The first one describes a good steady-state response but low dynamic response. On the contrary, vector control method in closed loop is used to achieve good dynamics [26].

2.2.3.1 Machine Equations in rotor reference frame

In rotor reference frame the d-axis of the stator field is aligned with the rotor permanent magnet flux while the q-axis is displaced 90^0 ahead in the direction of rotation. This frame rotates with the speed of the rotor, measured in electrical radians. The flux linkages and stator d-q voltage equations are presented below:

$$\lambda_{sd} = L_{sd} i_{sd} + \lambda_{fd} \tag{14}$$

$$\lambda_{sq} = L_{sq} i_{sq} \tag{15}$$

$$v_{sd} = R_s i_{sd} + \frac{d}{dt}\lambda_{sd} - \omega_r \lambda_{sq} \tag{16}$$

$$v_{sq} = R_s i_{sq} + \frac{d}{dt}\lambda_{sq} + \omega_r \lambda_{sd} \tag{17}$$

In equations (14-15), d and q axes flux linkages are λ_{sd}, λ_{sq} while λ_{fd} is the permanent magnet flux. The winding inductances are L_{sd}, L_{sq}, R_s being the phase resistance. The rotor speed is ω_r, measured in electrical rad/s [30]. In equation (18), the electromagnetic torque for a salient pole machine is represented:

$$T_{em} = \frac{3}{2} p\left(\lambda_{sd} i_{sq} - \lambda_{sq} i_{sd}\right) \tag{18}$$

$$\frac{d}{dt}\omega_{mech} = \frac{T_{em} - T_{load}}{J} \tag{19}$$

The rotor acceleration is calculated by subtracting the load torque from the electromagnetic torque and dividing this difference with the rotor inertia, J. The mechanical speed of the rotor, ω_{mech}, is represented in rad/s. To convert to electrical speed, the mechanical speed is multiplied by the motor pole pairs, p.

2.2.3.2 Implementation schematic in MATLAB/Simulink

In MATLAB/Simulink equations (14-19) are implemented to model the PMSM and in Fig.2.28 the implementation diagram block is depicted. The parameters of the machine required for its modeling are listed in Table 2.5.

Table 2.5. PMSM Parameters

DC bus voltage	120	V
RMS current	21	A
Nominal speed	2000	rpm
Nominal torque	12	Nm
Phase resistance (R_s)	0.2	Ω
D axis inductance (L_d)	0.002817	H
Q axis inductance (L_q)	0.002817	H
Permanent magnet flux (λ_{fd})	0.1025	Wb
Pole pairs (p)	3	-

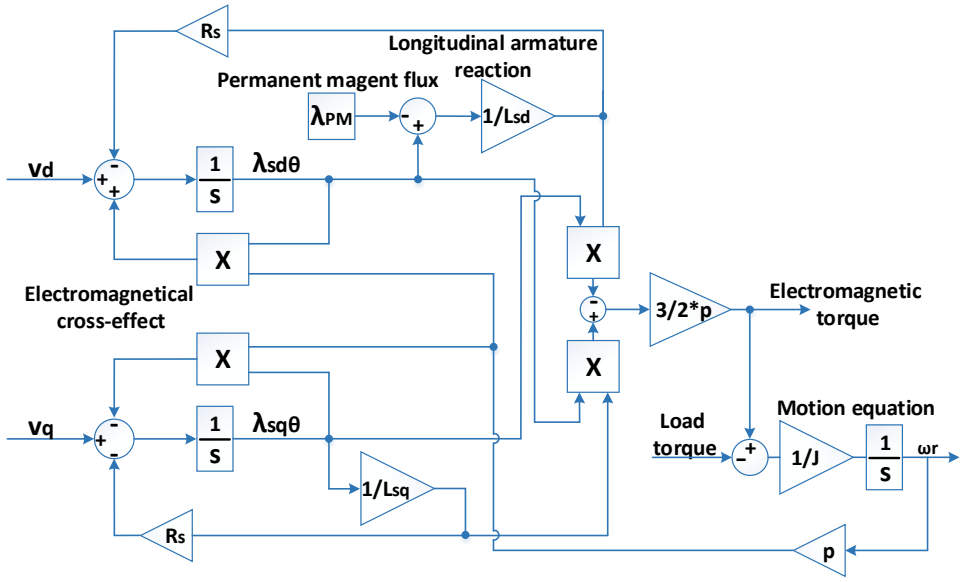

Fig 2.28. Diagram block of PMSM simulation model

2.2.3.3 Field oriented control of PMSM

Vector control, also known as field-oriented control (FOC) is a variable frequency control where the mathematically described three-phase PMSMs are represented in a similar approach to separately excited DC machines where the torque production and machine flux are decoupled. Using this approach high performance AC drives can be developed. The basic scheme for FOC is presented in Fig.2.29.

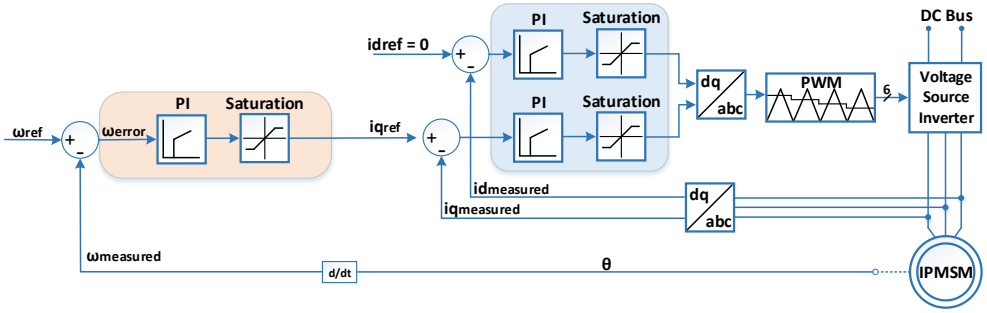

Fig.2.29. Generic FOC control scheme

In the final simulation platform both speed and torque controls are implemented as the test bench is built using two coupled PMSMs, one controlled in speed control and the other one, in torque control. The latter represents the motor used for vehicle propulsion. For the torque control the same scheme is implemented, as detailed in Fig.2.29, eliminating however the speed control loop (represented in orange frame) and the reference current on q-axis is calculated from the reference torque. In the speed control, from the reference, the actual rotor velocity is subtracted, and the error is input in the PI speed regulator. The output of the regulator is the reference q-axis current saturated by the maximum limit of the machine, the implementation being highlighted in the orange frame. The reference current on d-axis is set to zero as no field-weakening is applied. From these currents the measured d and q currents are subtracted, and the errors are the input signals for the two PI current regulators. These output the reference voltages, saturated at the DC link value. The reference voltages are transformed in three-phase voltages and the pulse width modulation is applied to obtain the control signals for the three-phase voltage source inverter.

2.2.3.4 Current and speed PI controller's design

The speed, the d and q-axis current control loops are presented in Fig.2.30.

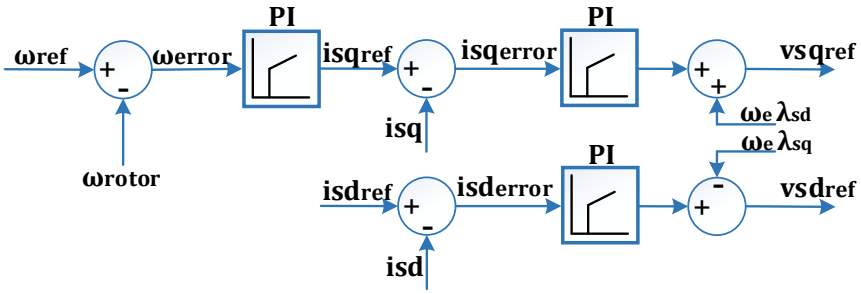

Fig.2.30. FOC control loops

In the above schematic to the output of the current regulators, the decoupling terms derived from the d-q voltage equations are added.

q-axis current controller

The current control loop for the q-axis is presented in Fig.2.31.

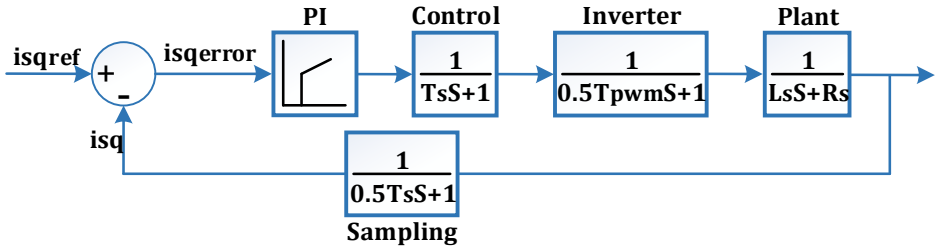

Fig.2.31. Current loop structure for the q-axis

In Fig.2.31 the control block is the delay introduced by the loop calculation frequency represented such as a first order transfer function. The loop frequency is 10 kHz resulting the control time constant, Ts of 0.1 [ms]. The next block introduces the delay due to the PWM inverter. The switching frequency is 10 kHz, the time constant, 0.5T is the inverse of the frequency, 0.1 [ms]. The sampling block represents the delay introduced by the digital to analog conversion, the time constant is half of the control time constant.

The PI transfer function is [31]:

$$PI = k_p(1 + \frac{1}{T_i s}) = k_p \frac{1 + T_i s}{T_i s} \tag{20}$$

In equation (20), kp, is the proportional gain and Ti, is the integral time constant.

For the plant model, the transfer function is given in equation (21).

$$\frac{i_{sq}}{v_{sq}} = \frac{1}{R_s + sL_{sq}} = \frac{1}{R_s} \frac{1}{1 + s\frac{L_{sq}}{R_s}} = \frac{K}{1 + s\tau_q}$$
$$K = \frac{1}{R_s} \tag{21}$$
$$\tau_q = \frac{L_q}{R_s}$$

The open loop transfer function of the q-axis control loop is:

$$G_{iq}(s) = k_{piq} \frac{1 + T_i s}{T_i s} \frac{K}{\tau_q s + 1} \frac{1}{T_s s + 1} \frac{1}{0.5T_s s + 1} \frac{1}{0.5T_{pwm} s + 1} \tag{22}$$

An equivalent time constant for the loop can be calculated to simplify the transfer function:

$$T_{si} = 1.5T_s + T_{pwm} = 0.2\ [ms] \tag{23}$$

$$G_{iq}(s) = k_{piq} \frac{1}{T_{iq} s} K \frac{1}{T_{si} s + 1} \tag{24}$$

The slowest pole of the transfer function is the machine pole, Tiq=τq=8 [ms] thus the zero of the controller is used to cancel this pole. The PI proportional gain is determined using the optimal modulus (OM) criterion [32]. Equation (25) is the standard form of a second order system.

$$G_{OM} = \frac{1}{2\tau s(\tau s + 1)} \tag{25}$$

$$\frac{k_{piq} K}{T_{iq}} = \frac{1}{2T_{si}} \rightarrow k_{piq} = \frac{T_{iq} R_s}{2T_{si}} = 0.107 \tag{26}$$

Equation (26) is obtained by making the analogy between the equations (24) and (25). In Fig.2.32 the Bode plot of the q-axis current controller is depicted. The minimum stability margins are represented on the plot and their magnitude and phase margins indicate the closed loop system's stability.

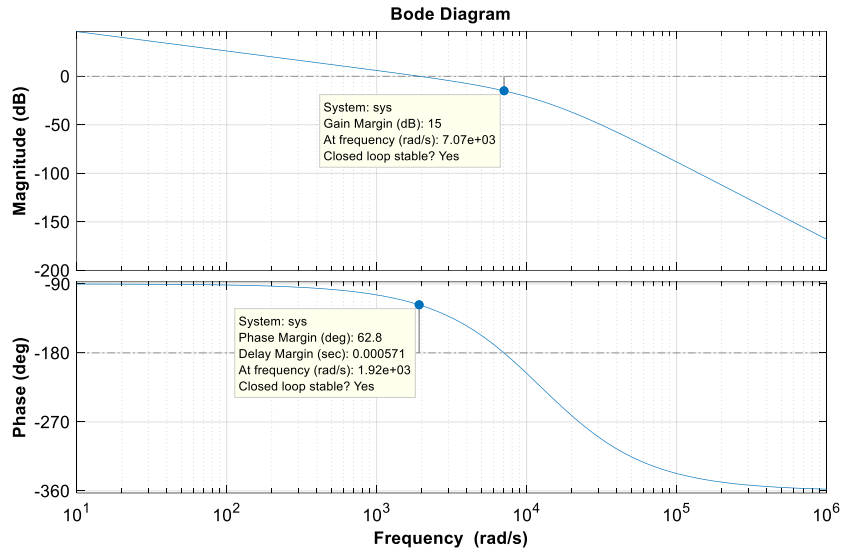

Fig.2.32. Bode plot of the current controller for q-axis

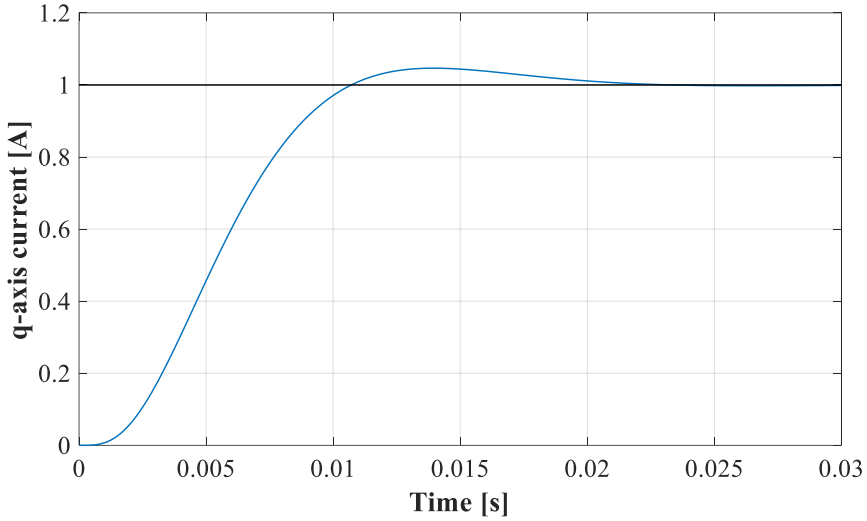

Fig.2.33. Step response of the current controller for q-axis

The step response of the q-axis current closed loop controller is presented in Fig.2.33. It can be observed that a very small overshoot occurs, and the settling time is approximatively 2.5 [ms]. For the d-axis current controller the same approach was used to calculate the PI gains.

PI speed controller

The speed loop is detailed in Fig.2.34. The delay introduced by the q-axis current controller is represented as a first order transfer function. The time constant of the transfer function is expressed in equation (27). The plant model is approximated to be the electromagnetic torque equation for a non-salient pole machine. In the last block the mechanical equation of the machine is represented. On the feedback loop, the delay of the filter applied to the measured speed is introduced. For a filter with 100 Hz cut-of frequency, the time constant is 1.6 [ms].

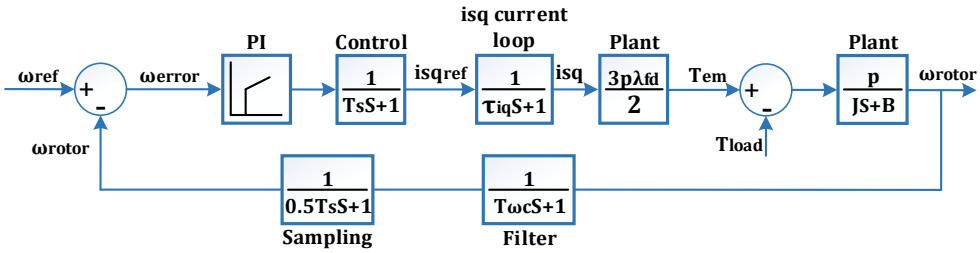

Fig.2.34. Speed control loop structure

The open loop transfer function and the equivalent time constant of the loop are presented in equation (28) and (29).

$$\tau_{iq} = \frac{T_{iq}}{k_{piq}K} \tag{27}$$

$$G_\omega(s) = \\ = \frac{1}{0.5T_s+1}\frac{1}{T_{\omega c}s+1}k_{p\omega}\frac{T_\omega s+1}{T_\omega s}\frac{1}{T_s+1}\frac{1}{\tau_{iq}s+1}\frac{3}{2}p\lambda_{fd}\frac{p}{Js} \tag{28}$$

$$T_{s\omega} = 1.5T_s + \tau_{iq} + T_{\omega c} \tag{29}$$

$$\text{If } K_T = \frac{3}{2}p\lambda_{fd} \rightarrow G_\omega(s) = \frac{p\,k_{p\omega}\,K_T(T_\omega s+1)}{JT_\omega s^2(T_\omega s+1)} \tag{30}$$

The speed regulator is tuned according to Optimum Symmetric Method (OSM) [33]. This method is used when a disturbance can be applied to the system, in this case represented by the load torque. The expression of the OSM in case of open loop transfer function is presented below.

$$G_{OSM}(s) = \frac{K_1 K_p T_I s + K_1 K_p}{s^2(T_1 T_I s + T_I)} \tag{31}$$

The open loop transfer function of the speed controller is modified to be similar to the standard OSM form.

$$G_{\omega}(s) = \frac{\frac{pK_T}{J} k_{p\omega} T_{\omega} s + \frac{pK_T}{J} k_{p\omega}}{s^2(T_{s\omega} T_{\omega} s + T_{\omega})} \tag{32}$$

From equations (31) and (32), by making the analogy, the proportional gain and the integral time constant are calculated.

$$k_{p\omega} = \frac{1}{2K_1 T_1} = \frac{1}{2p\frac{K_T}{J} T_{s\omega}} = 0.165 \tag{33}$$

$$T_{\omega} = 4T_1 = 4T_{s\omega} = 9\ [ms] \tag{34}$$

The Bode plot of the system is presented in Fig.2.35. The closed loop system is stable. Fig.2.36 depicts the step response of the speed controller. There is a large overshoot that will cause a high current in the q-axis. To reduce this overshoot, the current is limited to the maximum value accomplished by the antiwindup implemented for the PI controllers.

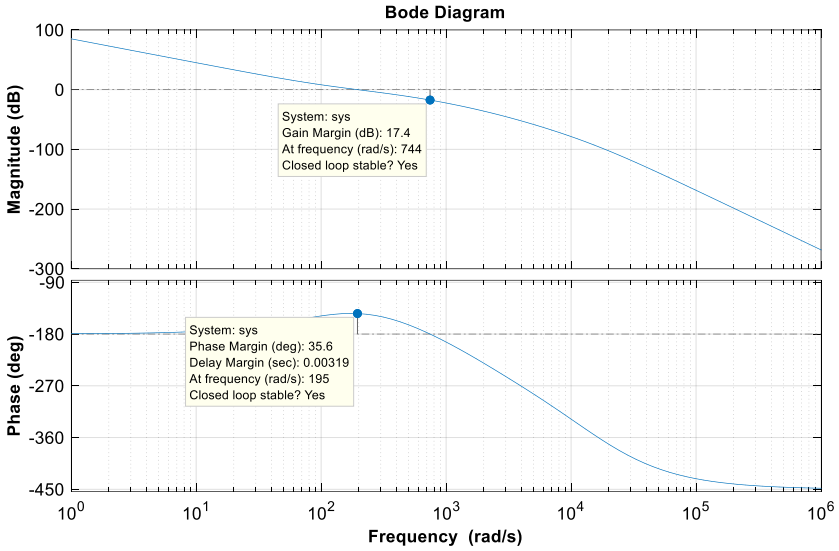

Fig.2.35. Bode plot of the speed controller

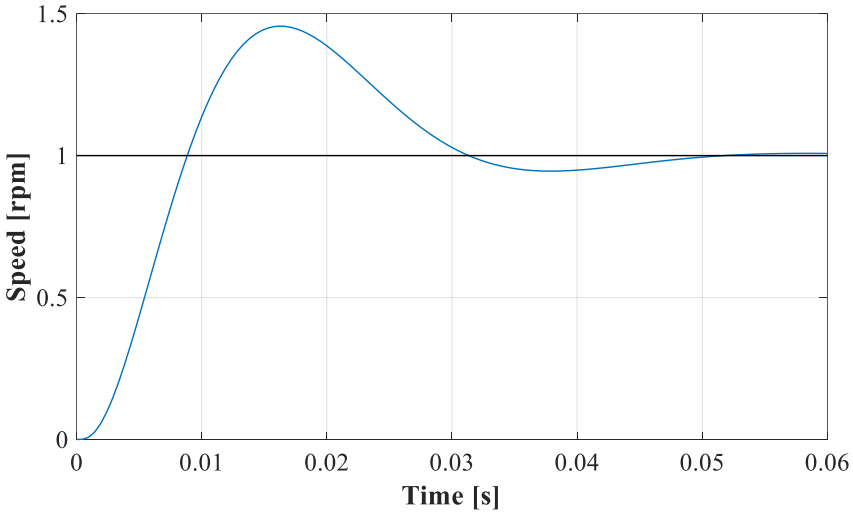

Fig.2.36. Step response of the speed controller

2.2.3.5 Speed controller validation

After the PI tunning process, the step response was applied in simulation and for the testbench to compare the results. In Fig.2.37 is depicted the speed variation. A very small disagreement can be noticed because for the test bench the tested motor was coupled with another motor used as load for other tests.

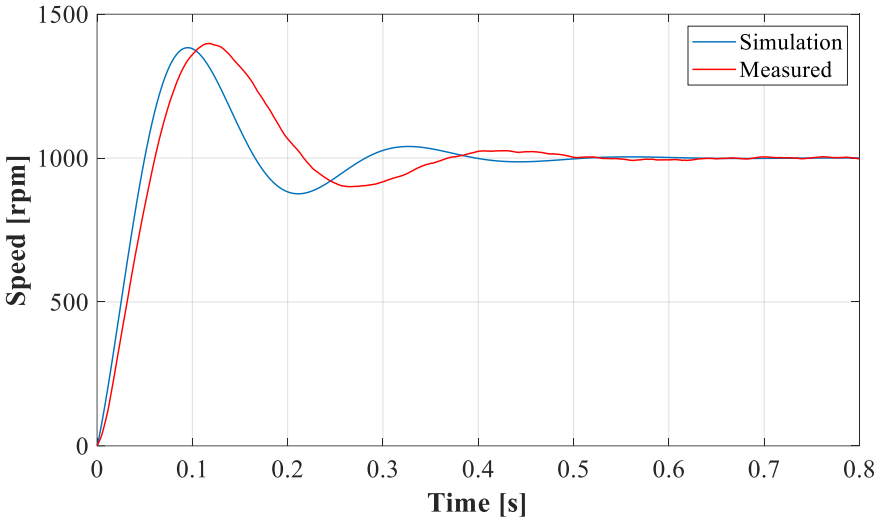

Fig.2.37. Speed step response (no load)

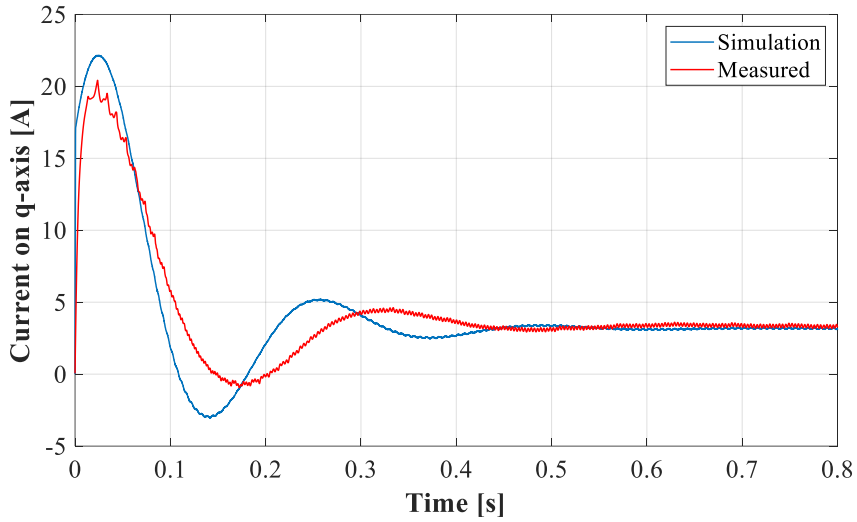

Fig.2.38. q-axis current for speed step response (no load)

The same difference is in the q-axis current, Fig.2.38, but for both characteristics the steady state was reached at the same time.

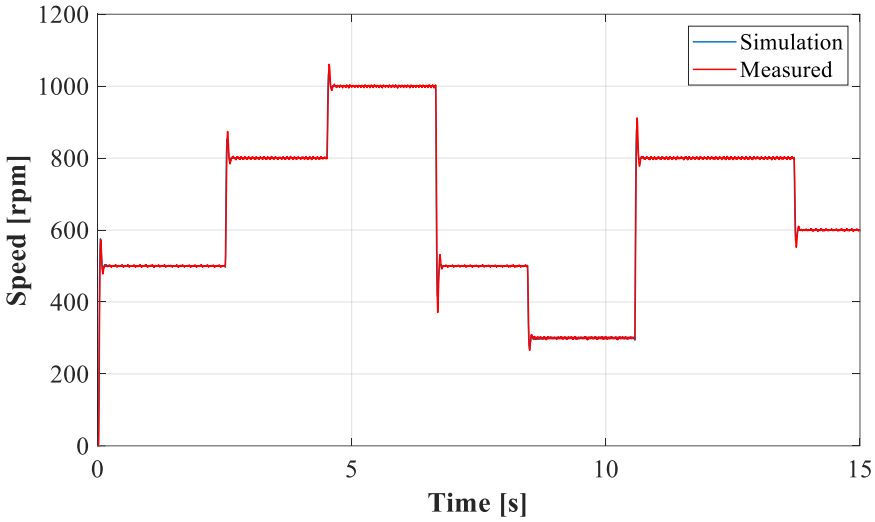

Fig.2.39. Speed response comparison

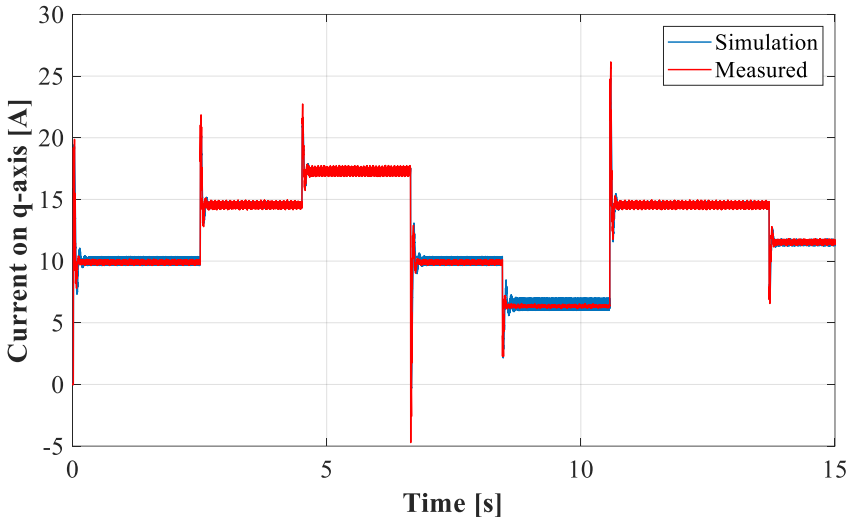

Fig.2.40. q-axis current variation

In the last test for the PI-controller, a constant load was applied to the machine and the reference speed was varied in steps, Fig.2.39. The current for the q-axis is depicted in Fig.2.40 and in Fig.41 is the d-axis current. From these results can be conclude that the results from the simulation and from the test bench are approximatively the same.

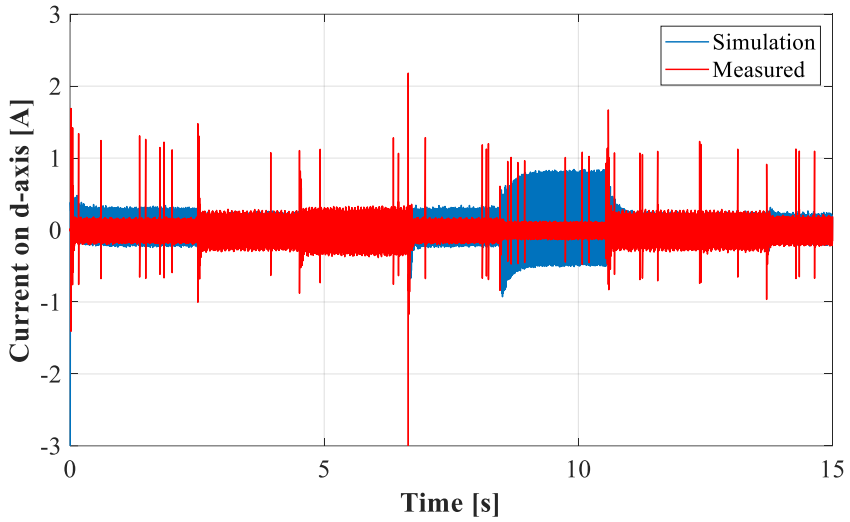

Fig.2.41. d-axis current variation

2.3. Conclusions

This chapter reviewed different electrical equivalent circuit models used to model Li-ion cells, several balancing circuit topologies and presents in detail the developed models of the platform components.

For the Li-ion cell, two ECM's are implemented and experimentaly validated. An innovative active cell balancing circuit was developed and practically tested for five cells. The depicted results for the balancing procedure prove the good functionality of the circuit and the balancing logic.

The three-phase inverter is implemented in simulation using the phase-to-neutral voltage equations. For this inverter the main losses, in MOSFET and reverse diode, are calculated.

Next, the PMSM is modelled using the machine equations in rotor reference frame (d-q). Speed and torque control methodes are developed, and their PI regulators' tunning process is presented. The chapter finishes with the validation of the speed control model.

REFERENCES

1. Min Chen and G.A. Rincon-Mora. Accurate electrical battery model capable of predicting runtime and i-v performance. Energy Conversion, IEEE Transactions on, 21(2):504--511, June 2006.

2. F. Huet. A review of impedance measurements for determination of the state-of-charge or state-of-health of secondary batteries. Journal of Power Sources, 70(1):59 -- 69, 1998.

3. E. Brasoukov and J.R. Macdonald, editors. Impedance Spectroscopy. Theory, Experiment and Applications. Wiley, 2 edition, 2005.

4. E. Karden, S. Buller, and R. W. De Doncker. A frequency-domain approach to dynamical modeling of electrochemical power sources. Electrochimica Acta, 47(13–14):2347 -- 2356, 2002.

5. D. Andre, M. Meiler, K. Steiner, Ch. Wimmer, T. SOCzka-Guth, and D.U. Sauer. Characterization of high-power lithium-ion batteries by electrochemical impedance spectroscopy. i. experimental investigation. Journal of Power Sources, 196(12):5334 -- 5341, 2011.

6. H. Zhang and M.-Y. Chow. Comprehensive dynamic battery modeling for phev applications. In Power and Energy SOCiety General Meeting, 2010 IEEE, pages 1--6, July 2010.

7. R. Jackey, M. Saginw, P. Sanghvi, J. Gazzari, T. Huria, and M. Ceraolo. Battery model parameter estimation using a layered technique: An example using a lithium iron phosphate cell. In SAE World Congress, 2013.

8. R. O. **Nemes**, S. Maria Ciornei, M. Ruba and C. Martis, "Parameters identification using experimental measurements for equivalent circuit Lithium-Ion cell models," 2019 11th International Symposium on Advanced Topics in Electrical Engineering (ATEE), Bucharest, Romania, 2019, doi: 10.1109/ATEE.2019.8724878.

9. V. Sangwan, A. Sharma, R. Kumar and A. K. Rathore, "Equivalent circuit model parameters estimation of Li-ion battery: C-rate, SOC and temperature effects," 2016 IEEE International Conference on Power Electronics, Drives and Energy Systems (PEDES), Trivandrum, 2016, pp. 1-6, doi: 10.1109/PEDES.2016.7914369.

10. J. Gomez, R. Nelson, E. Eric Kalu, M.H. Weatherspoon, Jim P. Zheng, "Equivalent circuit model parameters of a high-power Li-ion battery: Thermal and state of charge effects", May 2011, Journal of Power Sources 196(10):4826-4831, May 2011Journal of Power Sources 196(10):4826-4831 DOI: 10.1016/j.jpowsour.2010.12.107.

11. H. Fanga, C. Depcika, Vadim Lvovich, "Optimal Pulse-Modulated Lithium-Ion Battery Charging: Algorithms andSimulation" February 2018The Journal of Energy Storage 15:359-367, DOI: 10.1016/j.est.2017.11.007

12. K. Li and K. J. Tseng, "An equivalent circuit model for Li-ion batteries used in energy storage systems in building environment," 2016 IEEE Innovative Smart Grid Technologies - Asia (ISGT-Asia), Melbourne, VIC, 2016, pp. 504-510, doi: 10.1109/ISGT-Asia.2016.7796436.

13. H. He, R. Xiong, X. Zhang, F. Sun and J. Fan, "State-of-Charge Estimation of the Lithium-Ion Battery Using an Adaptive Extended Kalman Filter Based on an Improved Thevenin Model," in IEEE Transactions on Vehicular Technology, vol. 60, no. 4, pp. 1461-1469, May 2011, doi: 10.1109/TVT.2011.2132812.

14. S. Lee, J. Kim, J. Lee, and B. H. Cho, "State-of-charge and capacity estimation of lithium-ion battery using a new open-circuit voltage versus state-of-charge," J. Power Sources, vol. 185, pp. 1367–1373, 2008.

15. J. Lee et al., "Modeling and Real Time Estimation of Lumped Equivalent Circuit Model of a Lithium Ion Battery," 2006 12th International Power Electronics and Motion Control Conference, Portoroz, 2006, pp. 1536-1540, doi: 10.1109/EPEPEMC.2006.4778621.

16. I. Baccouche, A. Mlayah, S. Jemmali, B. Manai and N. Essoukri Ben Amara, "Implementation of a Coulomb counting algorithm for SOC estimation of Li-Ion battery for multimedia applications," 2015 IEEE

12th International Multi-Conference on Systems, Signals & Devices (SSD15), Mahdia, 2015, pp. 1-6, doi: 10.1109/SSD.2015.7348255.

17. K. S. Ng, C.-S. Moo, Y.-P. Chen, and Y.-C. Hsieh, “Enhanced coulomb counting method for estimating state-of-charge and state-of-health of lithium-ion batteries,” Applied energy, vol. 86, no. 9, pp. 1506–1511, 2009.

18. M. Ruba, S. Ciornei, R. Nemeș and C. Martis, "Detailed Design of Second Order Model of Lithium-Ion Battery Simulator Based on Experimental Measurements," 2019 11th International Symposium on Advanced Topics in Electrical Engineering (ATEE), Bucharest, Romania, 2019, pp. 1-6, doi: 10.1109/ATEE.2019.8724890.

19. Mircea Ruba, Raul Nemeș, Sorina Ciornei and Claudia Marțiș “Parameter Identification, Modeling and Testing of Li-Ion Batteries Used in Electric Vehicles”, Applied Electromechanical Devices and Machines for Electric Mobility Solutions, Adel El-Shahat and Mircea Ruba, IntechOpen, DOI: 10.5772/intechopen.89256.

20. Stroe, Daniel-Ioan; Swierczynski, Maciej; Stroe, Ana-Irina; Knudsen Kær, Søren. 2016. "Generalized Characterization Methodology for Performance Modelling of Lithium-Ion Batteries." Batteries 2, no. 4: 37.

21. J. Cao, N. Schofield and A. Emadi, "Battery balancing methods: A comprehensive review," 2008 IEEE Vehicle Power and Propulsion Conference, Harbin, 2008, pp. 1-6, doi: 10.1109/VPPC.2008.4677669

22. Rui Xiong, Weixiang Shen, "Advanced Battery Management Technologies for Electric Vehicles", February 2019, ISBN: 978-1-119-48164-5

23. M. Cherukuri and M. Kanthi, "Battery Management System Design for Electric Vehicle," 2019 IEEE International Conference on Distributed Computing, VLSI, Electrical Circuits and Robotics (DISCOVER), Manipal, India, 2019, pp. 1-6, doi: 10.1109/DISCOVER47552.2019.9008088.

24. Gregory Plett, Battery Management Systems, Volume II: Equivalent-Circuit Methods, Artech, 2015, ISBN:9781630810283.

25. K. Vinoth Kumar, Prawin Angel Michael, Joseph P. John and S. Suresh Kumar, Simulation And Comparison Of SPWM And SVPWM Control For Three Phase Inverter, ARPN Journal of Engineering and Applied Sciences, ISSN 1819-6608, Vol.5, No. 7, July 2010.

26. H. Abu-Rub, A. Iqbal and J. Guzinski "High performance control of ac drives with MATLAB/simulink models "John Wiley & Sons, 2012, ISBN: 978-0-470-97829-0.

27. S. Shuvo, E. Hossain, T. Islam, A. Akib, S. Padmanaban and M. Z. R. Khan, "Design and Hardware Implementation Considerations of Modified Multilevel Cascaded H-Bridge Inverter for Photovoltaic System," in IEEE Access, vol. 7, pp. 16504-16524, 2019, doi: 10.1109/ACCESS.2019.2894757.

28. G. Pellegrino, A. Vagati, B. Boazzo and P. Guglielmi, "Comparison of Induction and PM Synchronous Motor Drives for EV Application Including Design Examples," in IEEE Transactions on Industry Applications, vol. 48, no. 6, pp. 2322-2332, Nov.-Dec. 2012, doi: 10.1109/TIA.2012.2227092.

29. K. T. Chau, C. C. Chan and C. Liu, "Overview of Permanent-Magnet Brushless Drives for Electric and Hybrid Electric Vehicles," in IEEE Transactions on Industrial Electronics, vol. 55, no. 6, pp. 2246-2257, June 2008, doi: 10.1109/TIE.2008.918403.

30. Mohan, N. Advanced electric drives: analysis, control, and modeling using MATLAB/Simulink. John Wiley & Sons; Inc., Hoboken, New Jersey, Canada, 2014, ISBN: 978-1-118-48548-4.

31. Kiam Heong Ang, G. Chong and Yun Li, "PID control system analysis, design, and technology," in IEEE Transactions on Control Systems Technology, vol. 13, no. 4, pp. 559-576, July 2005, doi: 10.1109/TCST.2005.847331.

32. M.P. Kawmierkowski, H. Tunia, Automatic Control of Converter-Fed Drives, Elsevier, ISBN 0-7803-1101-9, 1995

33. R. Mizera Modification of Symmetric Optimum Method, ASR 2005 Seminar, Instruments and Control, Ostrava, April 29, 2005

3. Hardware in the Loop (HiL) testing facility

The complete testing facility is composed of two identical, off the shelf, PMSMs, one being the traction machine while the other is the load emulator. The two machines are supplied using two three-phase inverters, designed, builded and tested in this chapter. The traction machine's inverter is supplied by a Li-ion battery pack detailed in the last section while the load emulator's inverter is supplied from a bidirectional programable DC power supply. The circuits used for the battery balancing and identification procedures are included in the same chapter as part of the testing facility.

The first section of this chapter deals with sizing, designing, and testing of a three-phase inverter used to supply the PMSM engaged for the traction application. Also, the requirements and device ratings for the three-phase inverter are listed for the design methodology. Further on, the gate drive, the bootstrap and current measurement circuits are described. The first section ends with the inverter testing procedure using different configurations and different loads types. In the second part the cell balancing, and cell identification circuits are presented. The chapter ends with the battery configuration used as power supply.

3.1 Three phase inverter design

3.1.1 Requirements and device ratings

The traction motor used is rated at 2.5 kW and delivers 12 Nm at 2000 rpm base speed. Its rated current is 21 Arms at a DC link voltage of 120 V. For a short period of time the machine can develop twice its rated torque and a peak-power of 5 kW. The DC-bus voltage is ensured by a battery pack with the nominal voltage of 126V and 1.6 kW rated power.

The minimum voltage rating, V_{d_min}, of the power electronic device must be equal to the maximum of the DC-bus voltage, supplied by the battery, 147V. This voltage increases during the regenerative braking or sudden voltage spikes and a safety margin of 50V is added to the minimum value of the voltage rating.

$$V_d = V_{d\_min} + \Delta_{safe} \tag{31}$$

The rms current at maximum power is 42A, resulting approximatively 60A peak current. At this value a safety margin is added resulting a peak current for the power switch at least 120A.

$$I_d = (1.5 \div 2.5) I_{peak} \tag{32}$$

Considering the power switch ratings, the MOSFET IRFP4668 is used to build the three-phase inverter. Its main parameters are listed in Table 3.1.

Table 3.1. MOSFET IRFP4668 ratings

Continuous Drain Current (25^0C)	130	A
Continuous Drain Current (100^0C)	92	A
Drain-to-Source Breakdown Voltage	200	V
Maximum Power Dissipation	520	W
Diode Continuous Source Current	130	A
Diode Forward Voltage	1.3	V

3.1.2 The gate drive requirement and the bootstrap components

The principal gate drive requirements for a power MOSFET used as a high-side switch, Fig. 3.1:

- The gate voltage must be 10 to 15V higher than the source voltage. In the high-site configuration this voltage must be higher than the the highest voltage available in the system.
- The gate voltage must be controllable from the logic, normally referenced to ground.
- The power absorbed by the gate drive circuit should not significantly affect the overall efficiency.

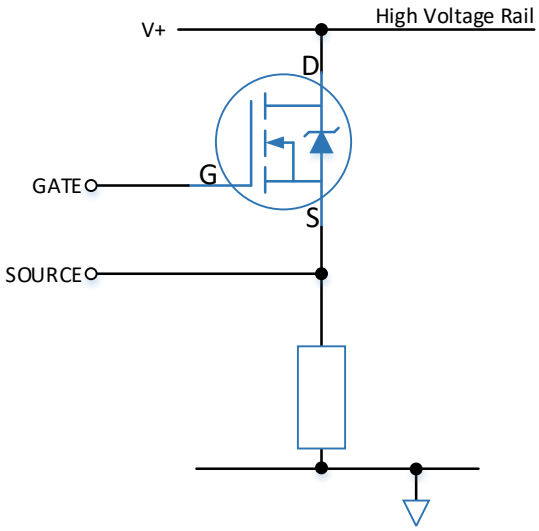

Fig.3.1. The power MOSFET in the high-side configuration

Taking into consideration the requirements of the gate drive, the half bridge driver IR2111 is used to perform this function. This driver integrates most of the functions required to switch one high-side and one low-side power MOSFETs in a compact, high performance package. The logic input is compatible with standard CMOS (complementary metal–oxide–semiconductor) outputs, dependent high and low side referenced output channels with internally set deadtime of 650 ns to avoid shoot-trough in the power half-bridge. Bootstrap principle can be applied and can operate up to hundreds of kHz switching frequency. The floating channel can be used in high side configuration for MOSFETs which operates up to 600V.

In half-bridge configuration the bootstrap circuit is used to supply bias to the high-side MOSFET. When the high-side FET (field-effect transistor) is off and the low-side FET is on, and the V_S pin is pulled to ground. The bootstrap capacitor is charged through the bootstrap diode from the V_{CC} bias supply [1]. Fig. 3.2 shows the charging and discharging path of a bootstrap circuit in a half-bridge configuration using IR2111 half-bridge driver.

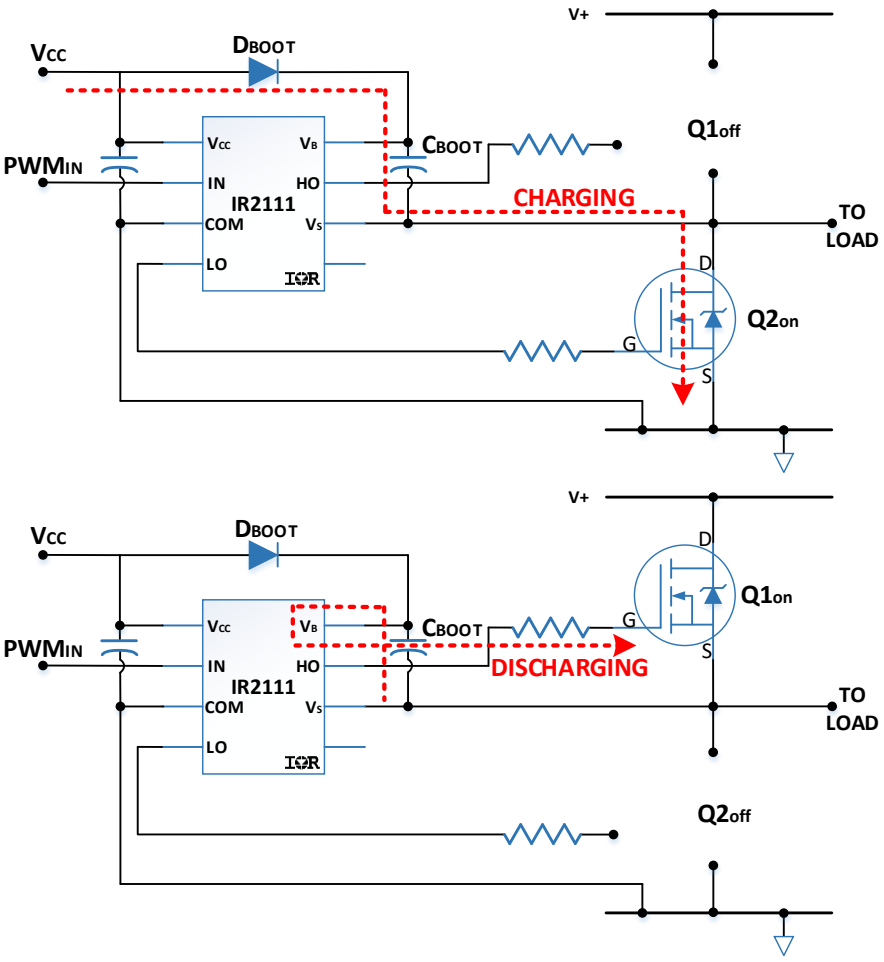

Fig.3.2. Bootstrap charging and discharging path

The bootstrap capacitor and diode are the only external components required for standard PWM applications. The voltage on the bootstrap capacitor is V_{CC}. Its capacitance must meet the following constraints:

- Gate voltage required to enhance MOS Gated Transistor (MGT)
- I_{QBS} – quiescent current for the high-side driver circuitry
- Currents within the level shifter of the control IC
- MGT gate-source forward leakage current

- Bootstrap capacitor leakage current (if bootstrap capacitor is an electrolytic capacitor)

To calculate the minimum charge which needs to be supplied by the bootstrap capacitor equation (33) is applied [2].

$$Q_{bs} = 2Q_g + \frac{I_{qbs(max)}}{f} + Q_{ls} + \frac{I_{Cbs(leak)}}{f} \tag{33}$$

where:

Q_g – gate charge of high side FET;

I_{Cbs} – bootstrap capacitor leakage current;

f – frequency of operation;

Q_{ls} – level shift charge required charge per cycle (5nC for 500V);

For the IRFP4668 MOSFET the minimum calculated charge reaches 497 nC. This charge must be supplied by the bootstrap capacitor and ensure its full voltage. If the voltage is not maintained, the undervoltage lockout can be triggered due to the ripple causing the HO output to stop functioning. This leads to a charge in the bootstrap capacitor at least two times the minimum calculated charge from above, equation (34), [2,3].

$$C \geq \frac{2\left[2Q_g + \frac{I_{qbs(max)}}{f} + Q_{ls} + \frac{I_{Cbs(leak)}}{f}\right]}{V_{cc} - V_f - V_{LS} - V_{Min}} \tag{34}$$

where:

V_f – forward voltage drop across the bootstrap diode;

V_{LS} – voltage drop across the low side FET;

V_{Min} – minimum voltage between V_B and V_S;

The value of the capacitor obtained from equation (34) is 135 nF this being the lowest required value. To minimize the risk of overcharging and reduce ripple on the V_{bs}, the minimum value of the bootstrap capacitor is multiplied by a factor of 15, considering also the

commercially available ratings. Hence, the capacitor selected is 2.2 uF multilayer ceramic capacitor.

The bootstrap diode must be able to block the full voltage rail when the high side device is switched on. A fast recovery diode is needed to minimize the charge feedback from the bootstrap capacitor into the V_{CC} supply. The diode used is MUR160 with super-fast recovery time, high efficiency, and low forward voltage drop.

3.1.3 The gate resistance and the current measurement circuits

Between the PWM signal from the controller and the half-bridge driver an optocoupler is used to provide galvanic isolation. In this configuration the inverter controller can't be damaged by any faults that can occur in the circuit. The complete circuit's schematic for one inverter leg is represented in Fig. 3.3. In Appendix A.1 the schematic and the PCB design for the driver circuit is detailed while in Appendix A.2 the power stage of the inverter is presented.

When the gate signal is turn-on, the power MOSFET's gate capacitance is charged through the R_{GATE} and the turn-off is secured by the D_{OFF} diode and R_{OFF} resistor.

The equations presented below are used to size the turn-on and off gate resistors for the IRFP4668 MOSFET and IR2111 half-bridge driver.

Turn-on gate resistance [4]:

$$I_{q(avr)} = \frac{Q_{gs} + Q_{gd}}{t_{sw}} = \frac{54 + 52\ (nC)}{500\ (ns)} = 212\ [mA]$$

$$R_{total} = \frac{V_{CC} - V_{gs(th)}}{I_{g(avr)}} = \frac{15 - 5}{0.212} = 47.2\ [\Omega] \tag{35}$$

$$R_{DRV(ON)} = \frac{V_{CC}}{I_{source}} = \frac{15\ (V)}{400\ (mA)} = 37.5\ [\Omega]$$

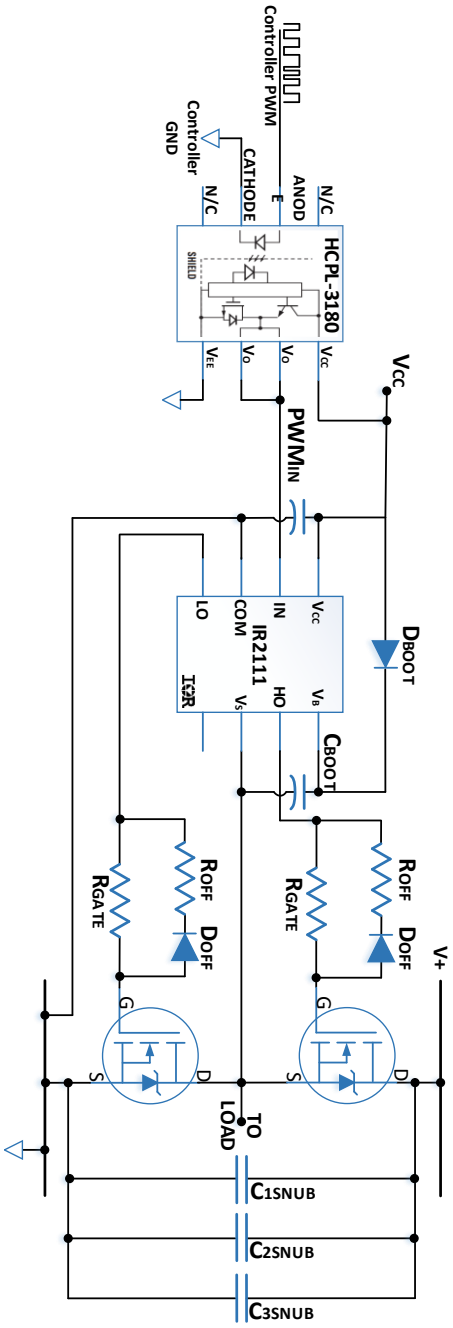

Fig.3.3. The schematic for one inverter leg

The turn-off gate resistance [4]:

$$R_{DRV(OFF)} = \frac{V_{CC}}{I_{sink}} = \frac{15\ (V)}{500\ (mA)} = 30\ [\Omega]$$

$$R_{g(off)} \leq \frac{V_{gs(th)min}}{C_{gd} \cdot \frac{dV_{out}}{dt}} - R_{DRV(OFF)} = \frac{3}{80 \cdot 10^{-12} \cdot 0.5 \cdot 10^{9}} - 30 = 7.5\ [\Omega] \quad (36)$$

where:

I_{source} – output low short circuit pulse current (driver)

$C_{gd(off)}$ – the Miller effect capacitor

dV_{out}/dt – voltage output slope

Snubbers are used in parallel with each inverter leg to smooth out any voltage spikes caused by the circuit's inductance when a semi-conductor opens. Three snubbers are mounted on the inverter to cover a wide range of ringing frequencies. The values of the snubber capacitances are 2.2, 0.22 and 0.01 pF.

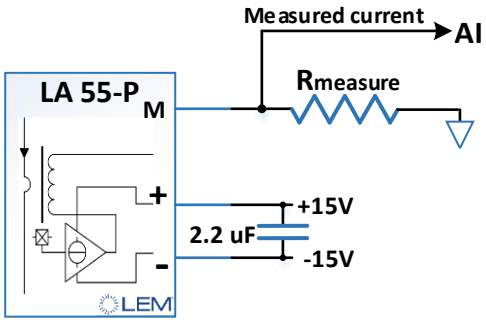

Fig.3.4. Schematic for current measurement

For each electrical machine phase, the circuit from Fig. 3.4 is used to measure the current. The Hall effect type current transducer mounted is LEM LA55-P. The maximum current measured by it is ±70A. The measuring resistance used in the circuit is a high precision 200Ω one. In Appendix A.3 the schematic of the complete circuit and PCB design used for the current measurement is presented.

3.1.4 Inverter testing protocols

Going forward with the development process of the inverter, the next step was to test it in different configurations connected to different load types. Preliminary, each leg was tested individually for different current ratings and load types. Next, the H-bridge configuration testing was carried out followed by the ultimate challenge, complete inverter testing under three-phase load.

a. Single inverter leg testing

Using the configuration from Fig. 3.5, only one inverter leg is used. Each leg was tested separately using the same load. For the first measurements a 680Ω resistor loaded the leg to ensure small current flow to check the voltage signals. The MOSFETs gate to source and drain to source voltages are measured to check the commutation process, Fig. 3.6 and 3.7. The switching frequency of the inverter is 10 kHz and the DC link voltage 120V, supplied from an external supply.

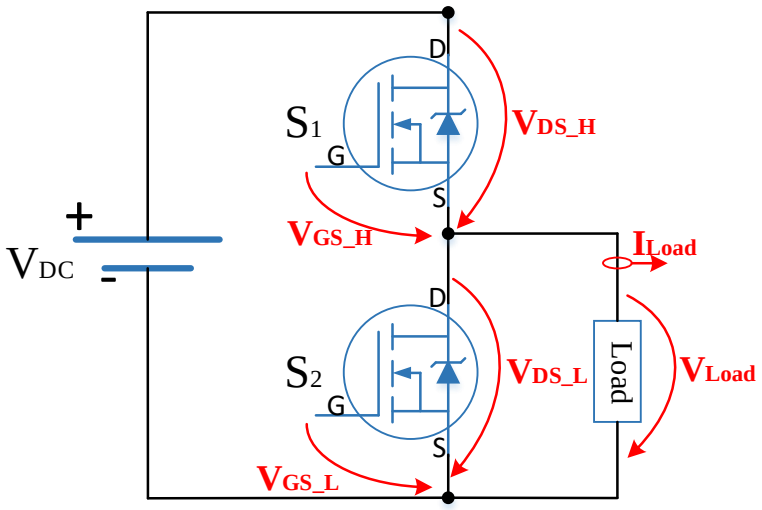

Fig.3.5. One leg test

In Fig. 3.6 a small difference between the high and low side gate voltages MOSFET can be noticed. This is caused by the voltage drop on the fast diode of the boot circuit. The drain to source voltage is depicted in Fig. 3.7 proving that no voltage spikes occur during the switching.

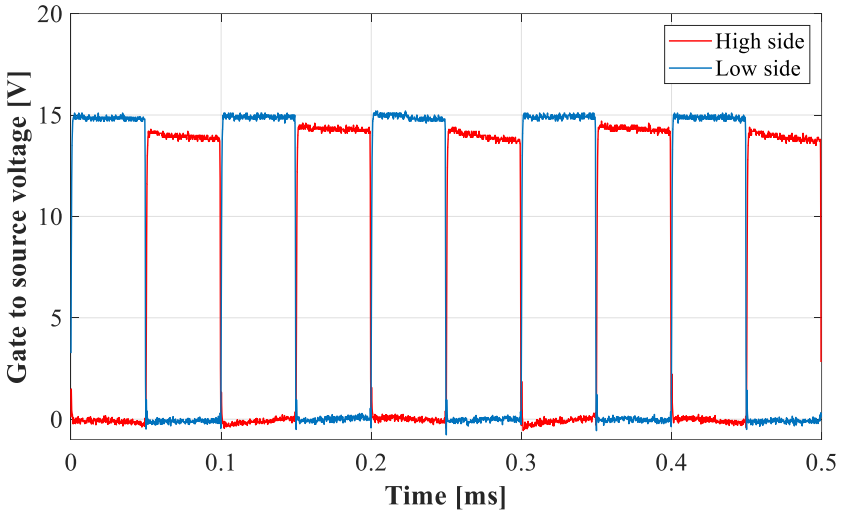

Fig.3.6. Gate to source signal

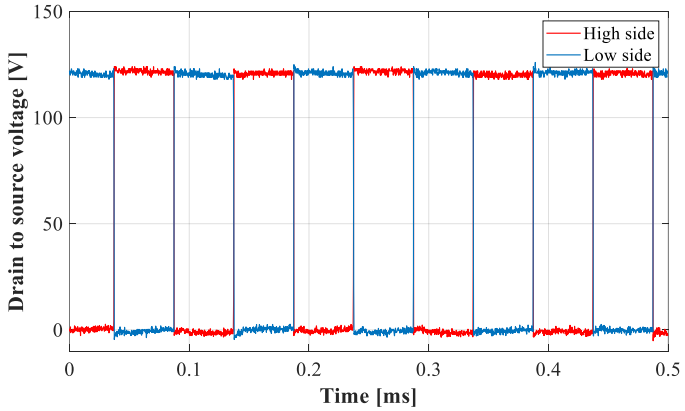

Fig.3.7. Drain to source signal

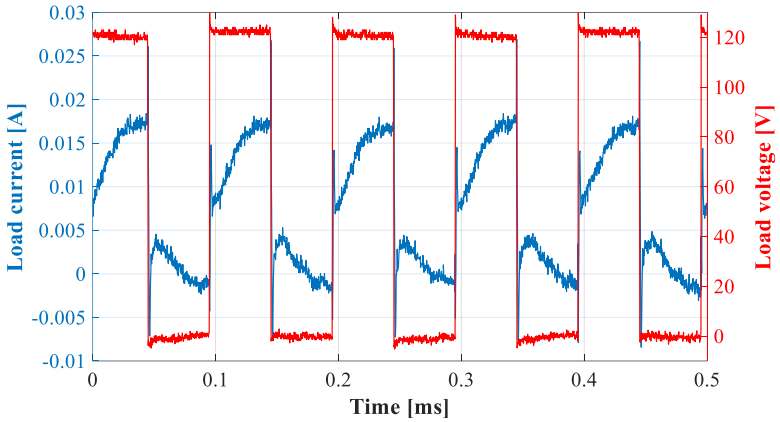

Fig.3.8. Load current and voltage

In Fig.3.8 both load current and voltage are superimposed. After this preliminary validation, a smaller resistive load was connected to the inverter leg, 2.2 Ω. This will push to higher current flow through the circuit. In Fig.3.9 the voltage on both top and bottom MOSFET's is depicted. Compared to Fig. 3.7 where the current was close to zero (practically no load situation), here a very small disturbances can be noticed on the voltage due to the 2.2 Ω load that is not purely resistive. This proves that the inverter leg is working correctly. The current and voltage through the load are depicted in Fig. 3.10. The mean value of the current through the load was 20A obtained for 40% duty cycle at 120V DC link voltage. In the next setup a resistive-inductive load of 2.344mH and 0.2 Ω resistance was used. The DC link voltage was kept the same, however the current through the load increased in this condition to 32A. The drain to source voltages on both FETs are depicted in Fig.3.11 and due to the inductive load, a ringing effect can be observed in the voltage. In Fig.3.12 the load current and voltage are depicted.

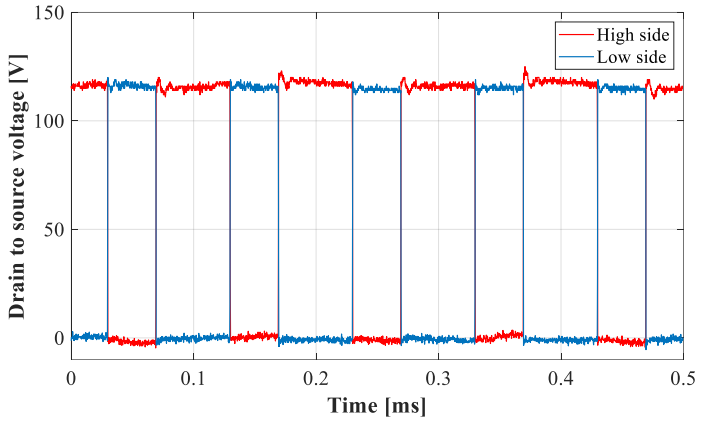

Fig.3.9. Drain to source voltage

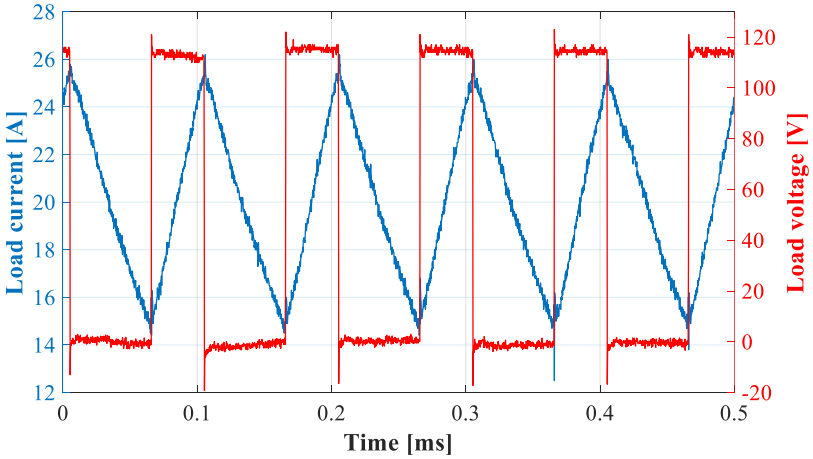

Fig.3.10. The load current and voltage

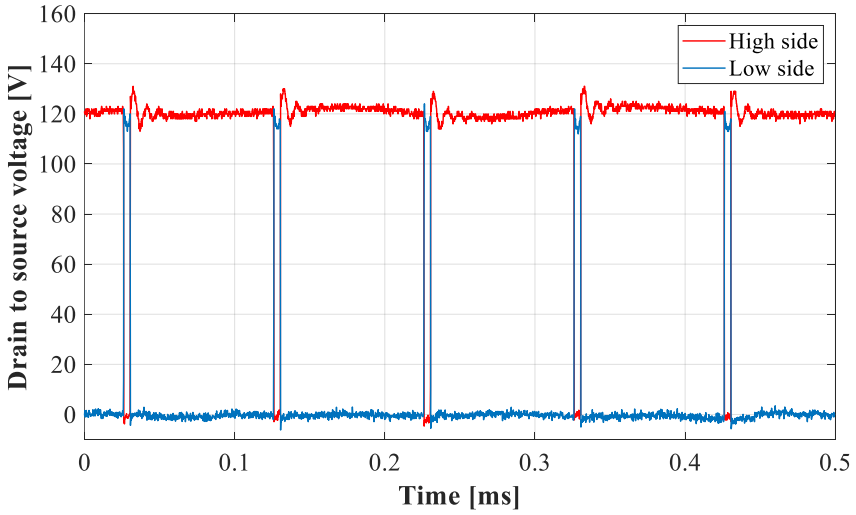

Fig.3.11. The voltage across the power FET's using an inductive load

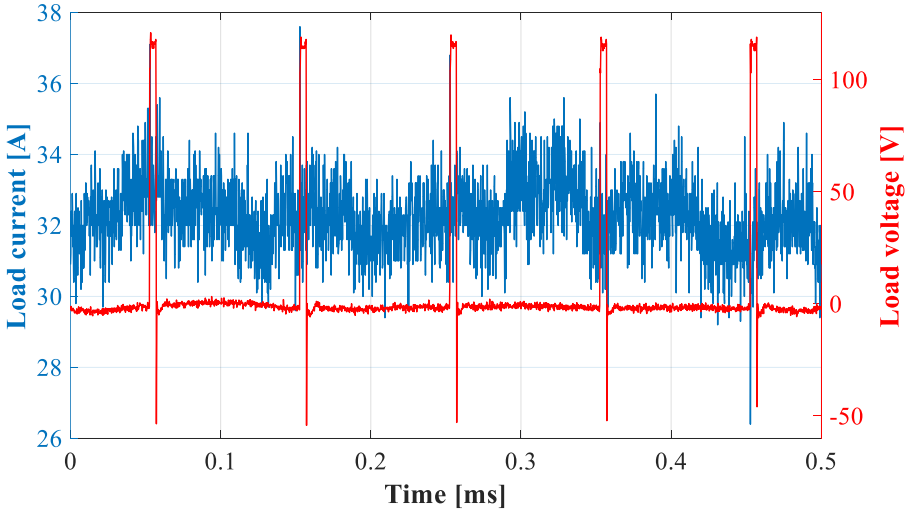

Fig.3.12. The voltage across the power FET's using an inductive load

b. H-bridge configuration testing

In H-bridge configuration, two legs of the inverter are engaged, as it can be seen in Fig. 3.13. The same inductive load is used for testing, rated at 2.344mH and 0.2 Ω. PWM technique was used for this test, switching at

10kHz frequency while the reference signal for the modulation was a sinusoidal wave with a frequency of 55Hz, in order to obtain a wide range of load currents and voltages in a single test. In Fig. 3.14 the gate to source signal for one leg of the H-bridge is depicted, emphasizing the inductive nature of the load. On the same leg the voltage across de FETs was measured and plotted in Fig.3.15.

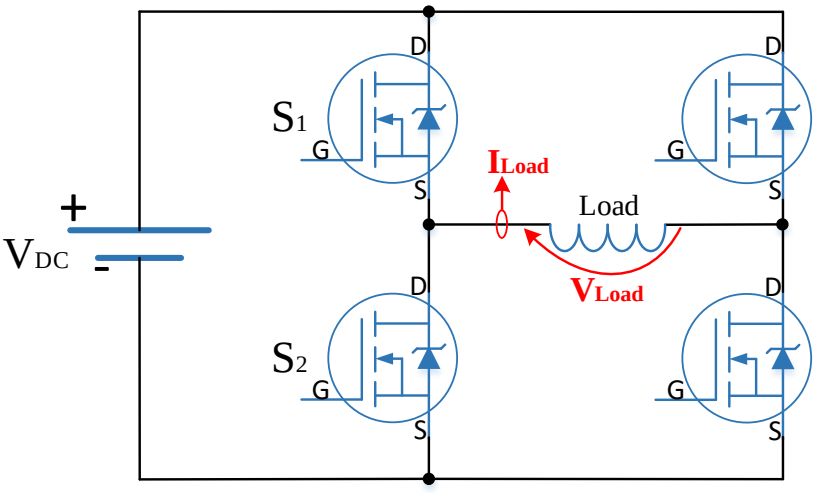

Fig.3.13. The H bridge circuit

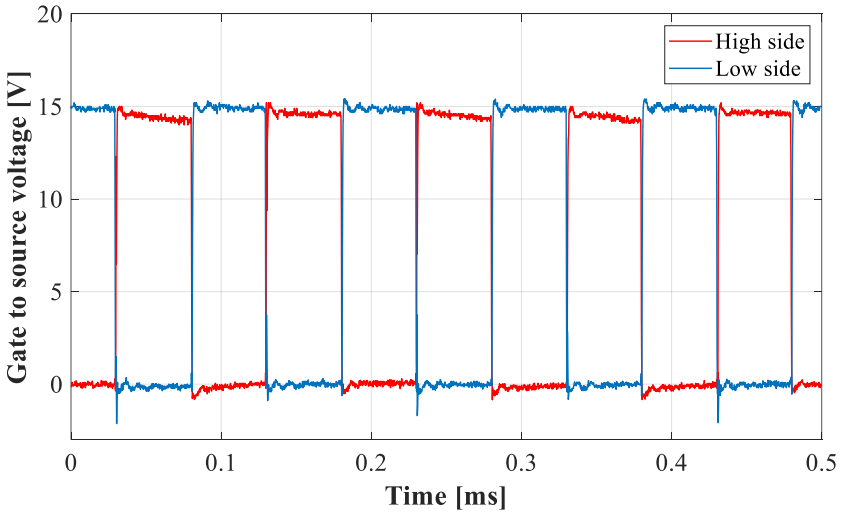

Fig.3.14. The gate to source signals for one leg

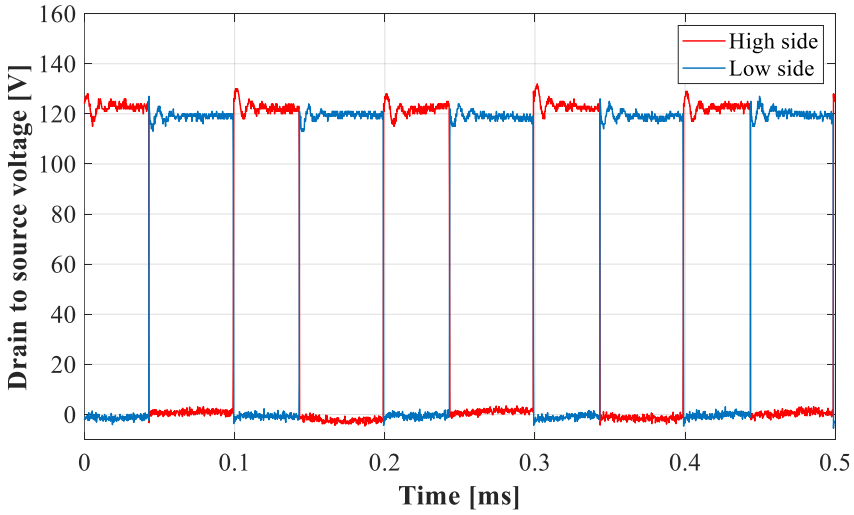

Fig.3.15. The drain to source voltage for one leg

The current flowing through the inductive load is depicted in Fig. 3.16, with no filter applied to the measured signal. This value was the maximum that can be reached as for larger ones the magnetic circuit will saturate and distorte the sinusoidal current shape. In the load voltage, Fig. 3.17, spikes and ringing effects can be seen due to the load inductance.

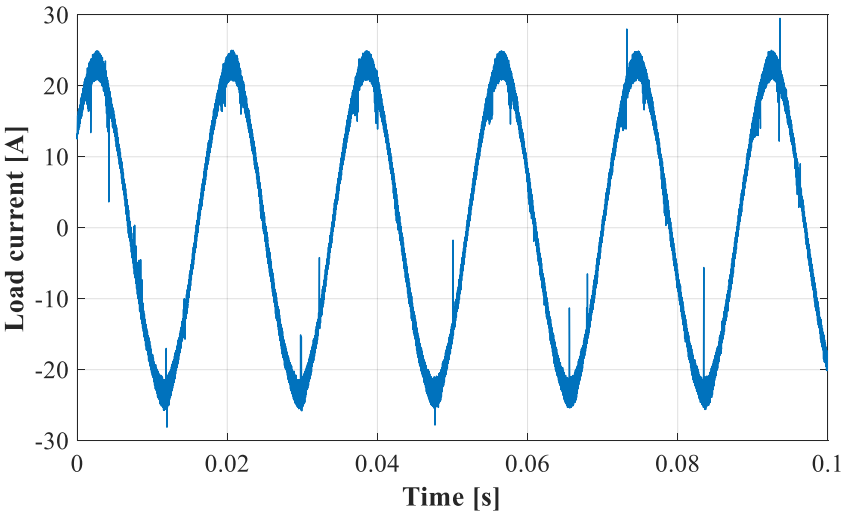

Fig.3.16. The load current

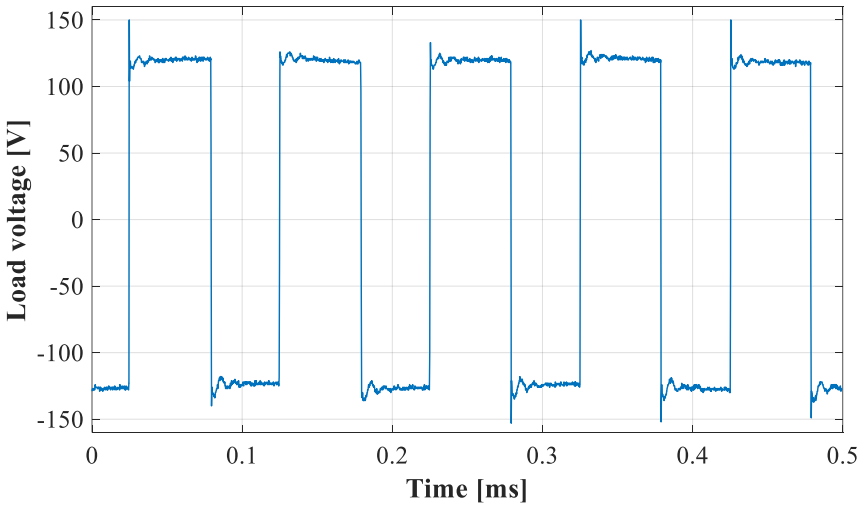

Fig.3.17. The load voltage

c. Complete inverter testing

For the final test the inverter was connected to a three-phase inductor used as a load (Fig. 3.18). Each inductor coil (each inductor phase) has 2.344mH and 0.2 Ω. The DC link voltage was kept at 120V and the switching frequency 10kHz. A three-phase reference voltage was applied to the PWM at a frequency of 55Hz.

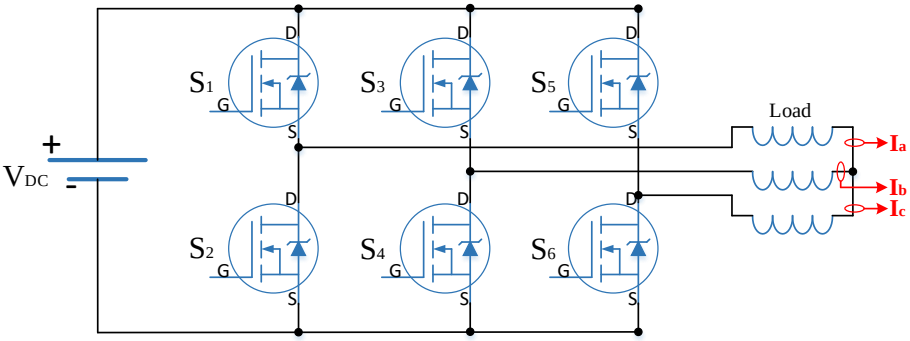

Fig.3.18. The three-phase inverter connected on the inductive load

The drain to source voltage for the high and low side FETs are depicted separately in Fig. 3.19 and Fig. 3.20. In the last figure, Fig. 3.21, the three-phase load currents are superimposed.

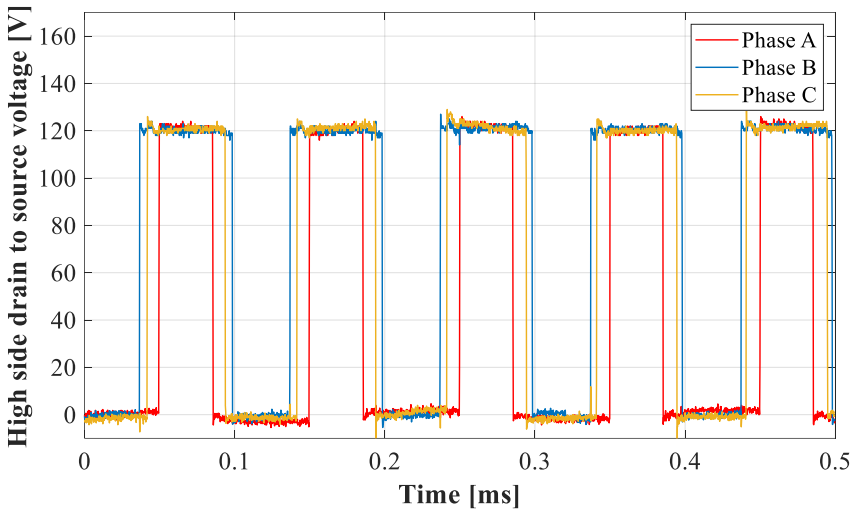

Fig.3.19. Drain to source voltage for the high-side FETs

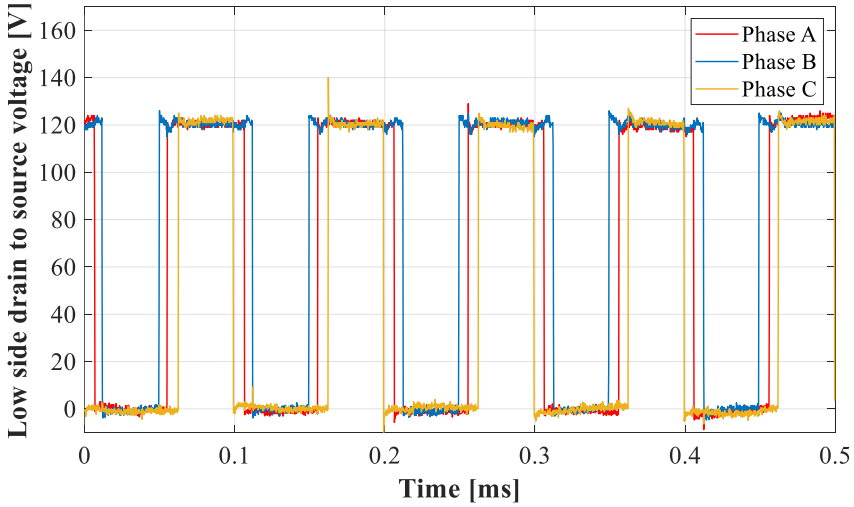

Fig.3.20. Drain to source voltage for the low-side FETs

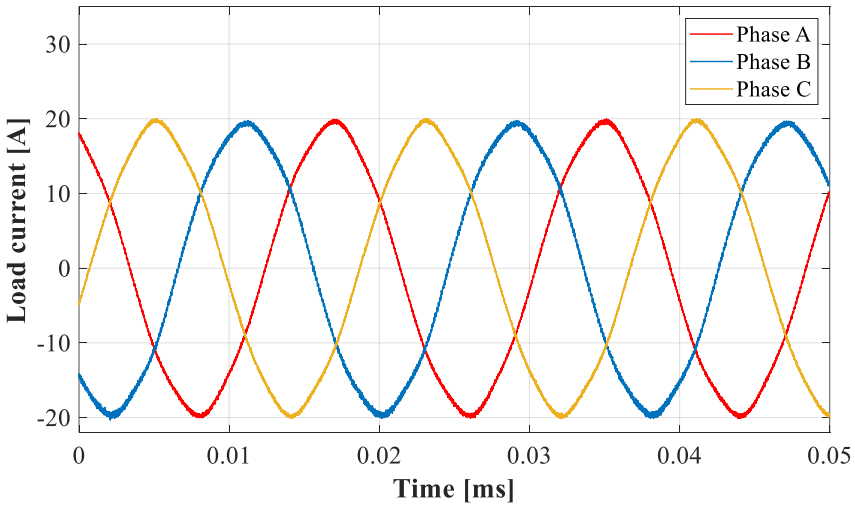

Fig.3.21. The load three-phase current

The general conclusion of all the above-mentioned testing procedures is that the inverter operates as expected. In close to pure resistive load there is no significant voltage or current signal distortion. On the other hand, in inductive load condition there are spikes, ringing and other parasitic effects that are phenomena accompanying the characteristic behavior. Even so, these values are acceptable and there is no need to consider these as abnormalities issues that can create worries.

3.2 The cell balancing and identification circuit

3.2.1 The cell balancing circuit

The cell balancing circuit's operation and architecture is presented in chapter 2.2. Modelling of electric vehicle drive train assemblies, page 42. To switch the cell connections, automotive relays are used because there was no space limitation, no high switching frequency, and the goal was to build a circuit to prove the balancing concept/operation. The used relays are TE V23086 rated at 30A. To energize the coil's relay a BC107 bipolar NPN transistor was used, controlled from the digital output ports (3.3V) of the balancing controller. It is not possible to switch the relays directly from the digital ports because the coil's rated current is higher than the maximum output current of the digital ports. The circuit's schematic is presented in Fig. 3.22. The BC107 transistor was used as the maximum current is 0.2A, enough to energize the relay coil. The transistor's operation areas are the cut-off region (fully-OFF) and saturated one (fully-ON). In the cut-off region the input base current and output collector current is zero and the collector-emitter voltage is maximum, therefore the transistor is switched fully-OFF. For the saturation region, maximum base current is applied to have maximum collector current, and the minimum collector-emitter voltage drop. In this condition the maximum current is flowing through the transistor because is switched fully-ON. To operate the transistor in these regions the base resistance is calculated using equation (37). The minimum base current is 0.25 mA to have 50 mA current through the collector enough to energize the relay's coil. For the base resistor a safety margin was taken into consideration and the base current was increased at 0.4 mA.

$$I_B = \frac{I_C}{\beta} = \frac{0.05}{20} = 0.25\ [mA]$$
$$R_B = \frac{V_{in} - V_{BE}}{I_B} = \frac{3.3 - 0.7}{0.004} = 650\ [\Omega] \quad (37)$$

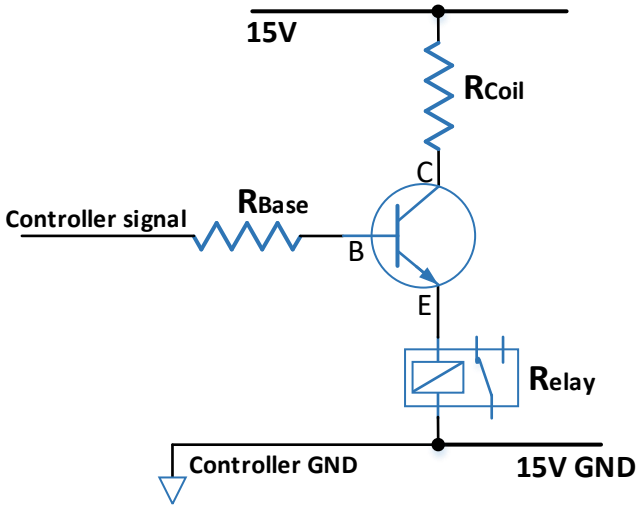

Fig.3.22. One relay circuit schematic

To limit the current through the relay's coil a 60 Ω resistance was connected in series because the voltage used to supply the coil is 15V and the nominal voltage from datasheet is 10V.

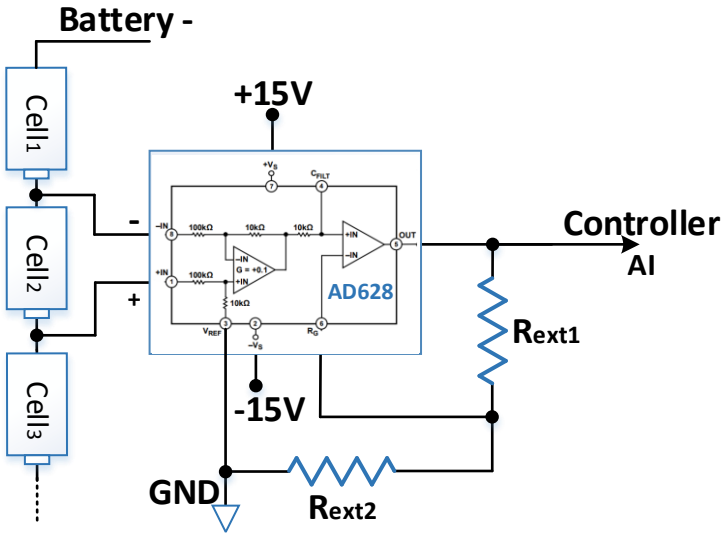

Fig.3.23. Battery cell voltage measurement

In Fig. 3.23 is the circuit designed to measure the cell voltage using an operational amplifier AD628. To set the amplifier's output gain to 1, the additional resistances, R_{ext1} and R_{ext2} must be equal to 100kΩ and11kΩ,

respectively. This amplifier is used as there is a high common-mode voltage difference amplifier with the voltage range of ±120V when supplied with ±15V. The common-mode rejection is the ability of the differential amplifier to eliminate the common-mode voltage applied to both inputs from the output. In the cell balancing circuit, five cells can be balanced. The problem occurs when the voltage for the fifth cell is measured because the common mode voltage exceeds 15V and its measurement is not accurate if a high common-mode voltage difference amplifier is not used. The complete schematic of the balancing circuit and its PCB design are presented in Appendix B.

3.2.2 The cell parameters identification circuit

To identify the battery cell parameters, the circuit to measure the voltage, current and temperature is given in Fig. 3.24. In this circuit for the voltage measurement an operational amplifier is used, while for the current measurement a hall effect current transducer is engaged. For the temperature quantification thermistors-based measurement is approached.

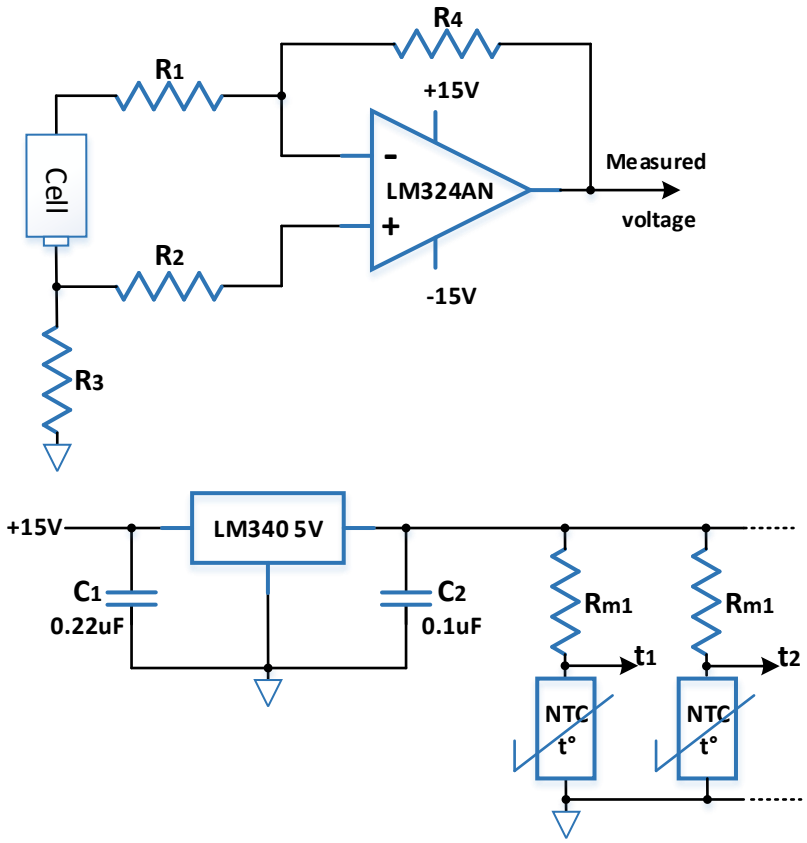

Fig.3.24. Identification circuit, voltage and temperature measurement

For the voltage measurement the LM324AN operational amplifier is used, and the circuit architecture is presented in Fig. 3.24-top. The amplification gain is calculated by dividing R_1 or R_2 by R_3 or R_4 resistors value. For R_3 and R_4, three different resistor values are mounted on the

circuit and using a jumper, any one of the three can be manually selected to set the amplification gain. To supply the temperature measurement circuit with 5V, a voltage regulator (LM340) is connected to the 15V voltage supply, Fig. 3.24 bottom. NTC thermistors are used for the temperature measurement. This circuit can be used to identify a complete battery and twelve thermistors that can be placed in different regions of the battery pack for thermal monitoring. The circuit for the current measurement was described above, in the inverter current measurement section on page 75. In Appendix C the schematic and the PCB design for the cell parameters identification circuit are presented.

As mentioned above, the circuit can monitor twelve different temperatures. To reduce the number of analog input channels a multiplexer it is engaged, as presented in Fig. 3.25. Using this circuit only one analog input is required to fetch all the temperatures and using four digital channels (to create the selection code), any one of the twelve temperature is selected to be displayed/measured.

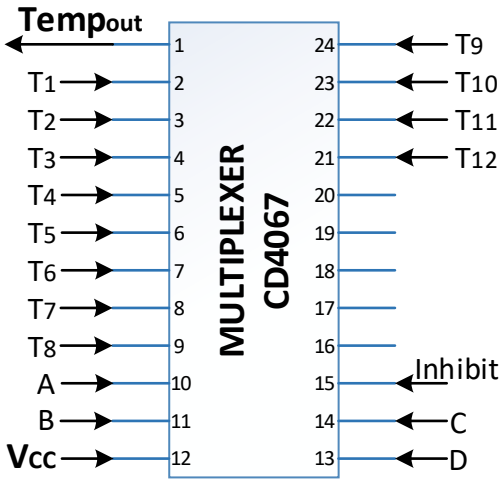

Fig.3.25. The multiplexer for the temperature measurement

3.3 The battery unit

The battery pack consists of Li-Ion NCR18650B cells produced by Panasonic. To reach the desired voltage level of the DC link, 120V, 35 cell packs are connected in series. To ensure the needed capacity, each cell pack contains 4 parallel connected cells. The final battery configuration is depicted in Fig. 3.26.

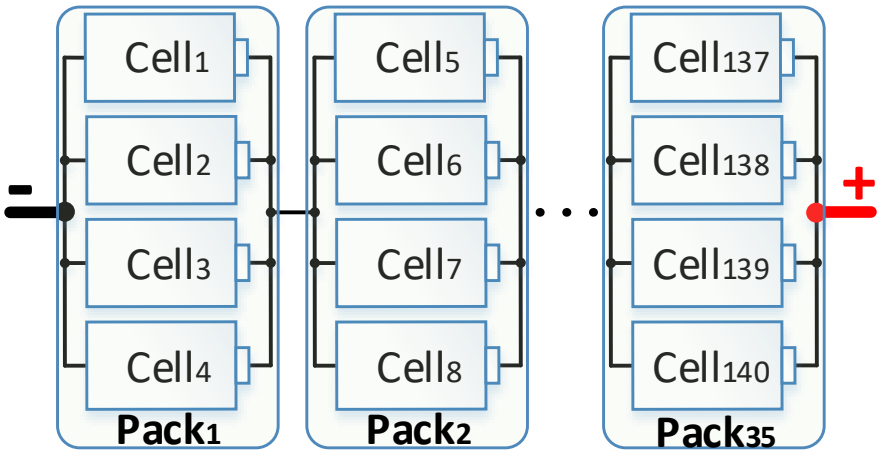

Fig.3.26. The scooter battery configuration

For each group of four parallel cells a plastic casing was designed using SolidWorks, a modeling computer-aided design and computer-aided engineering computer program. The designed model was loaded in Ultimaker Cura software, an open-source model slicing application for 3D printers. The design and the sliced model are presented in Appendix D. After building the parallel packs, the series connection was based on 2.5mm solid cooper conductors. The complete battery pack can be seen in the Appendix D. On the main battery connectors, a 16A two pole over current switch was installed for safety reasons, FAZ-C16/2-DC.

3.4 Conclusions

This chapter presented the designed and built circuits for the testing facility. Also, the Li-ion battery configuration used in the HIL testing as supply is presented. In the first section, the sizing, designing, testing protocols and the results for the built three-phase inverters are detailed. The chapter continues with detailes about the balancing and identification circuits and finishes presenting thebattery pack configuration.

REFERENCES

1. Mamadou Diallo, “Bootstrap Circuitry Selection for Half-Bridge Configurations” Texas Instruments, Application Report SLUA887–August 2018.

2. Jonathan Adams, “Bootstrap Component Selection for Control IC’s”, International Rectifier application note, 233 Kansas Street, El Segundo, CA 90245 USA.

3. STMicroelectronics, Application NOTE, “L63906 High voltage high/low-side driver” March 2018 DocID14493 Rev 11.

4. ON Semiconductor, Application NOTE, “AN-6076 Design and Application Guide of Bootstrap Circuit for High-Voltage Gate-Drive IC” Publication Order Number: AND9674/D, January 2018 − Rev. 2.

5. STMicroelectronics, Application NOTE, “STEVAL-IHM023V3, 1 kW 3-phase motor control evaluation board featuring L6390 drivers and STGP10H60DF IGBT” November 2014 DocID027120 Rev 1..

6. STMicroelectronics, User manual, “UM0580, 100 W 3 phase inverter featuring L6390 and STD5NK52ZD for vector control STEVAL-IHM021V1” September 2008 Rev 1.

4. Experimental results

In this chapter the experimental results are presented and analyzed. The first step is the real-time model in the loop (RTMiL) simulation where the Amesim model was connected with MATLAB/Simulink. In Amesim the dynamic model of the electric vehicle was created, and the driving cycle was imposed. In MATLAB/Simulink the traction motor, the torque control and the battery model were implemented. The link between the two software packages was done using NI VeriStand and the complete simulation is running on the embedded controller NI PXIe. The next step was the hardware-in-the-loop (HIL) tests where the complete platform was broken down into assemblies to test them separately before they are coupled together. The final step was the comparison between the simulation and experimental results.

4.1. Real-time model in the loop results

The first step for the complete system validation was the real-time simulation. Here, all the models of the electric vehicle drive train presented in Chapter two are integrated and simulated on a real-time processor. The hardware used for this simulation was a PXIe 1071 chassis, equipped with a PXIe 8135, 2.3 GHz Quad-Core embedded controller from National Instruments. The two software packages used to implement the models for the complete drive train, MATLAB/Simulink and Amesim, are coupled using NI VeriStand, a software package for real-time test applications. In Fig. 4.1 the real-time simulation platform is depicted, where the models are running on the real-time processor and the PC is used for interface.

To run the models on the real-time processor for both software packages several settings must be fulfilled before the real-time dynamic-link library (DLL) file can be generated. In both simulation software packages the fixed-step solver is selected with the same step size, 1 kHz. For Amesim a VeriStand interface is created to read or write signals in the model. In Simulink, to read or write signals in the model, special input and output ports used for VeriStand interface are added and in the Code Generation tab the system target file NIVeriStand.tlc is set. The PWM used in the torque field-oriented control implemented in Simulink was

discarded because the carrier wave has a frequency of 10 kHz, and the real-time processor is not able to run a model with frequencies higher than 1kHz. After all mentioned settings are done the real-time DLL file can be compiled. In VeriStand the two real-time models are imported in the simulation model tab and the input/output ports can be accessed. In system configuration mappings the connections between the two models is handled. When the models are deployed on the real-time target, these perform like one large simulation. In system explorer, an embedded data logger custom device was created to stream the measurements data in a TDMS file for data post processing. In NI VeriStand an interface was created to display and control the simulation process [1-3].

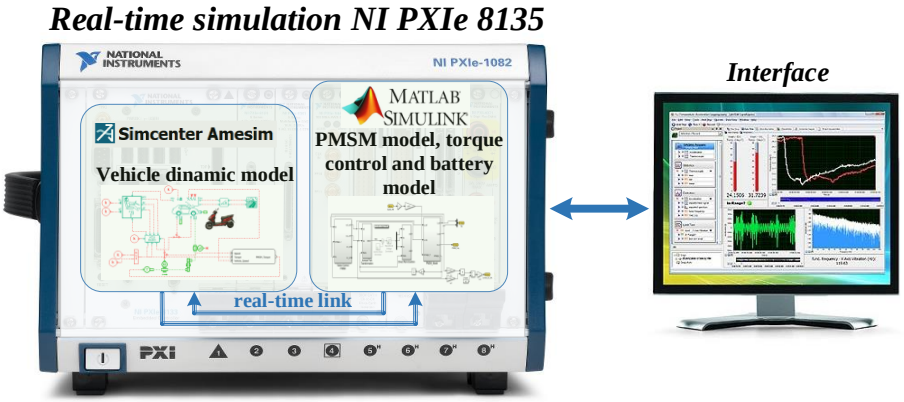

Fig.4.1. RTMiL schematic

For all the simulated and experimental tests, the same operational scenario was applied. The vehicle speed variation was obtained from an urban cycle from Cluj-Napoca, Romania, prerecorded using a GPS recorder. This track is saved in text file and applied in Amesim to the vehicle driver as reference speed. The control unit for the electric vehicle computes the torque needed for the vehicle reaching a speed equal to the reference one. This torque is used as reference for the torque control strategy implemented in Simulink. The computed current on q-axis is calculated from the reference torque, whilethe current on d-axis is set to zero. The reference q-axis current and the one obtained in the simulation are depicted in Fig. 4.2 whilein Fig.4.3 the PMSM torque is plotted. In Simulink the PMSM torque was calculated and transmitted back to the vehicle model in Amesim. Between the traction motor and vehicle wheel a mechanical reducer was introduced in Amesim with a gear ratio of five.

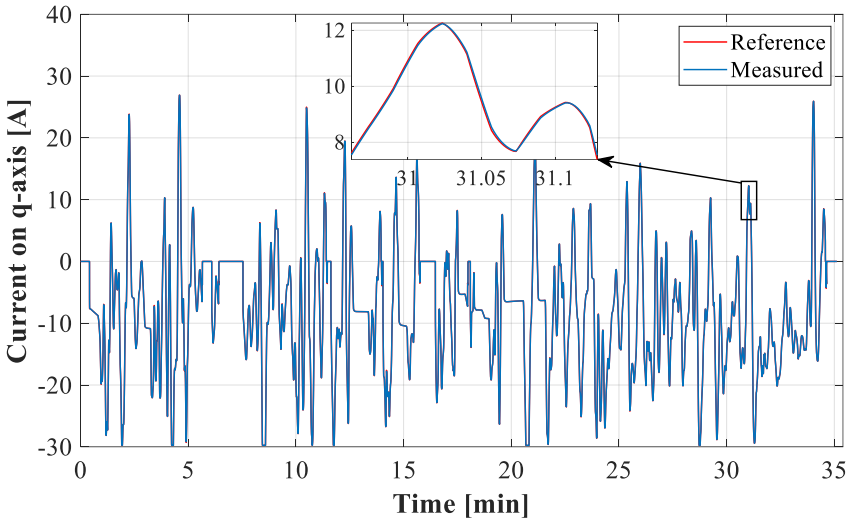

Fig.4.2. The current on q-axis

A very good agreement can be seen in Fig. 4.2, between the reference and simulated current on q-axis. This underlines the robustness of the regulators in charge with the currents control.

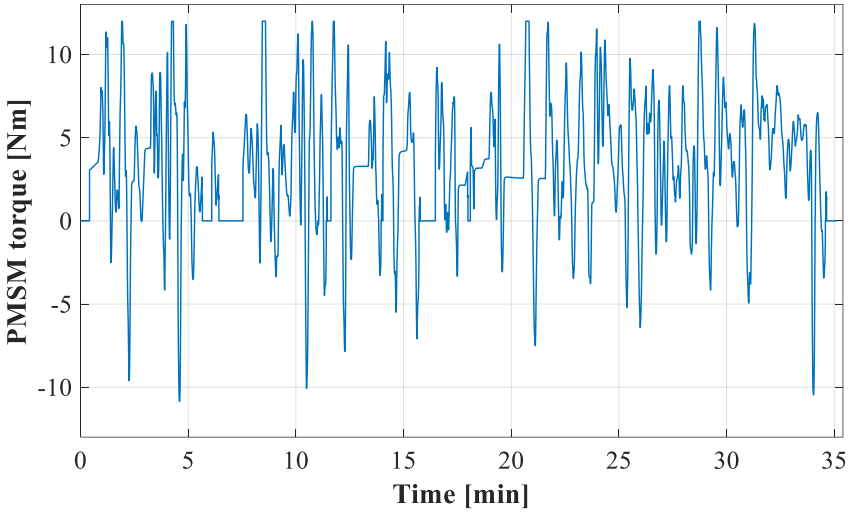

Fig.4.3. The traction motor's developed torque

The PMSM torque presented in Fig. 4.3 is driven through a reducer and the obtained vehicle speed is represented in Fig. 4.4. Because the

reference current and simulation current are in the good agreement, the vehicle speed follows closely the urban cycle as operation scenario.

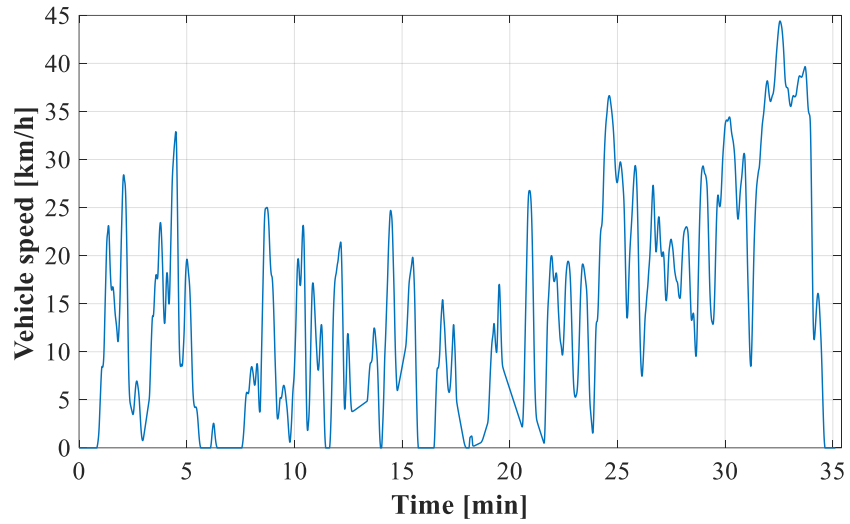

Fig.4.4. The vehicle speed

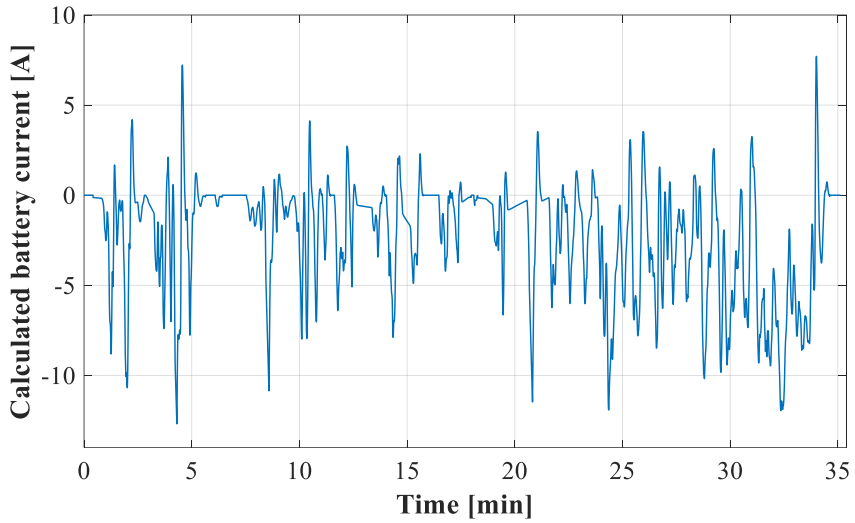

Fig.4.5. The current applied to the battery

In the simulation, the DC-link is supplied from the battery model. The current drained from the battery is calculated by multiplying the modulation index with the three-phase PMSM currents. This DC current is represented in Fig. 4.5 and referenced to the battery model. The battery voltage variations for the first and second order models are depicted in Fig. 4.6 whilein Fig.4.7 the state of charge is plotted.

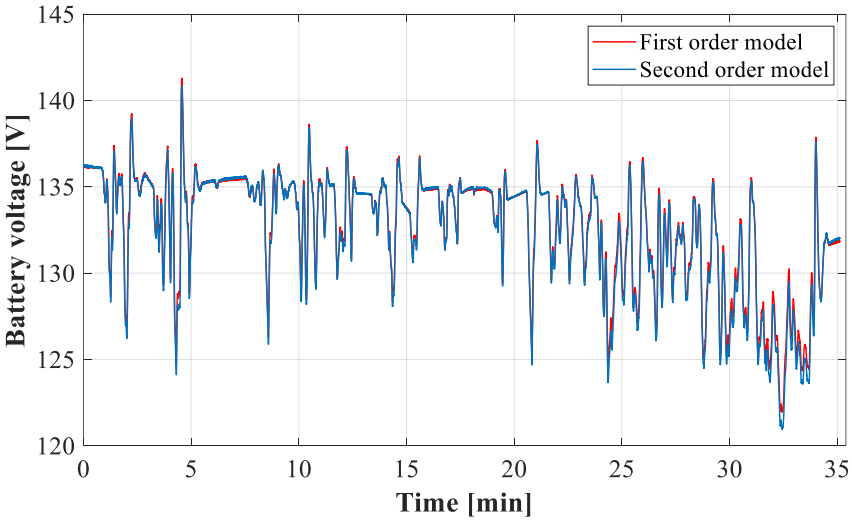

Fig.4.6. The battery voltage variation

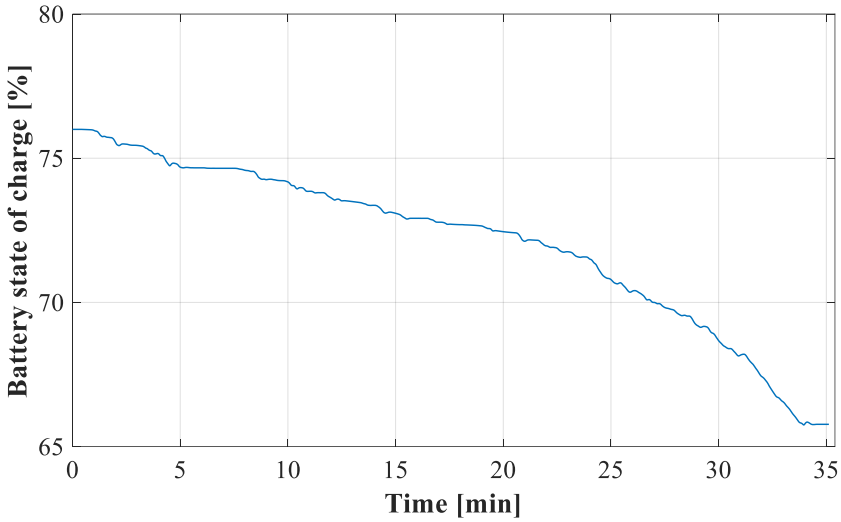

Fig.4.7. The battery state of charge

4.2. Hardware-in-the-loop tests

In the current section the complete hardware testing facility is gradually validated. Before the integration of the complete platform, the main components are separately tested and validated.

In the first configuration the real-time model of battery pack is compared with measurements performed on the real battery. The next step is the torque and speed control validation for the two machines, the traction and the load emulator one. Moving forward, the vehicle battery was emulated using a programable bidirectional DC power supply connected to the traction machine's three-phase inverter to analyze the system behaviour before connecting the real battery. For the ultimate test, the complete platform was validated, and the chapter ends with the comparison of the RTMiL and HIL results.

4.2.1. Battery-in-the-loop results

In the Battery in the Loop (BiL) setup the real battery is connected to a bidirectional power supply that acts as a power source/sink. The VeriStand model is the same as presented in the RTMiL, but the calculated current becomes reference for the bidirectional power supply. This is remotely controlled through the analog interface and behaves like the actual vehicle (seen from the battery's perspective). Using the NI PXI-7841R FPGA reconfigurable I/O module, the calculated current is converted in reference voltage necessary for the analog output port. This is connected to the bidirectional power supply's analog interface by this controlling the current drained or supplied from/to the battery. The actual battery voltage is measured and sent to the Simulink model becoming the DC link voltage in the real-time simulation [4-6].

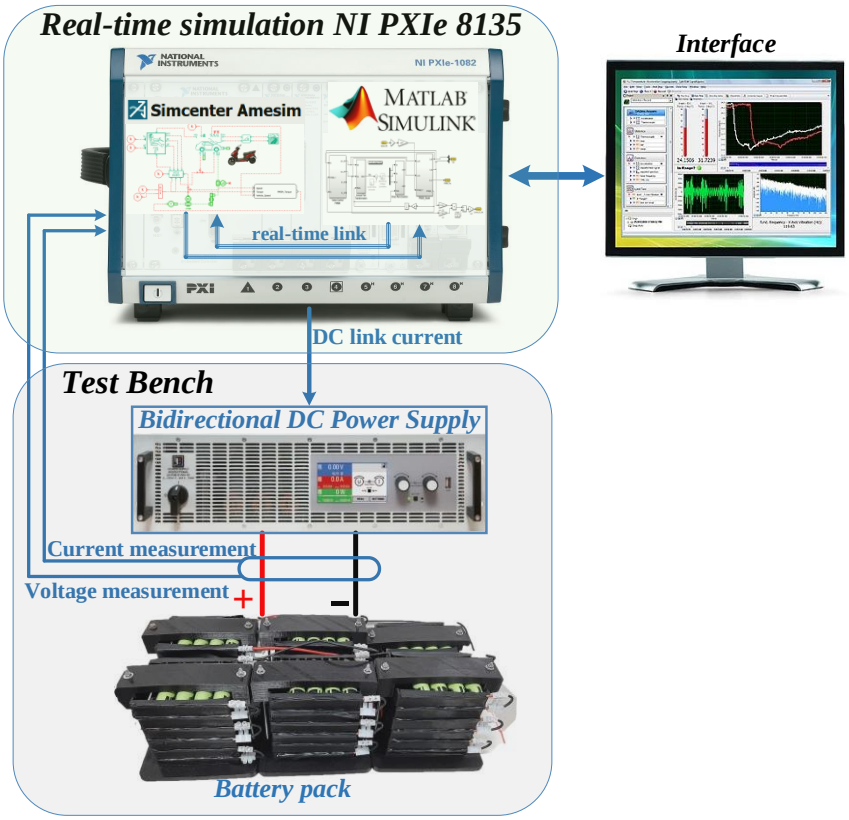

Fig.4.8. Battery HIL scheme

In Fig. 4.8 the configuration of the test bench for battery HIL testing is depicted. In the bottom rounded rectangle, the battery under test is connected to the bidirectional power supply. On top of the setup, the PXIe is running the real-time simulation. This is connected to the PC to control the simulation and to display the signals on the interface. The measured battery voltage variation is represented in Fig. 4.9.

The current drained/sourced to the battery is the same current represented in Fig. 4.5. To validate the battery models, the first, and second order, as well as the measured voltages are plotted on the same graph, Fig. 4.10. Very small disagreements can be observed between the simulation results and the measured voltage. For a better perspective, the absolute error is quantified and depicted in Fig. 4.11. The smallest error is obtained for the second order model.

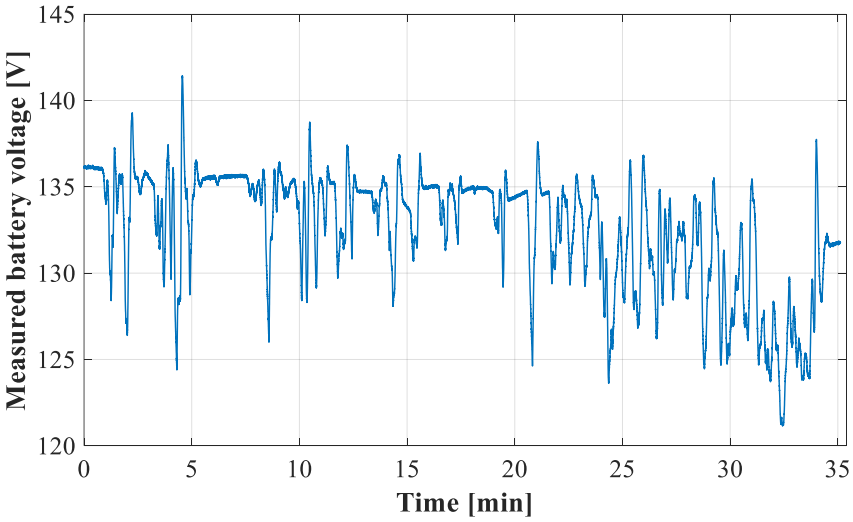

Fig.4.9. The measured battery voltage

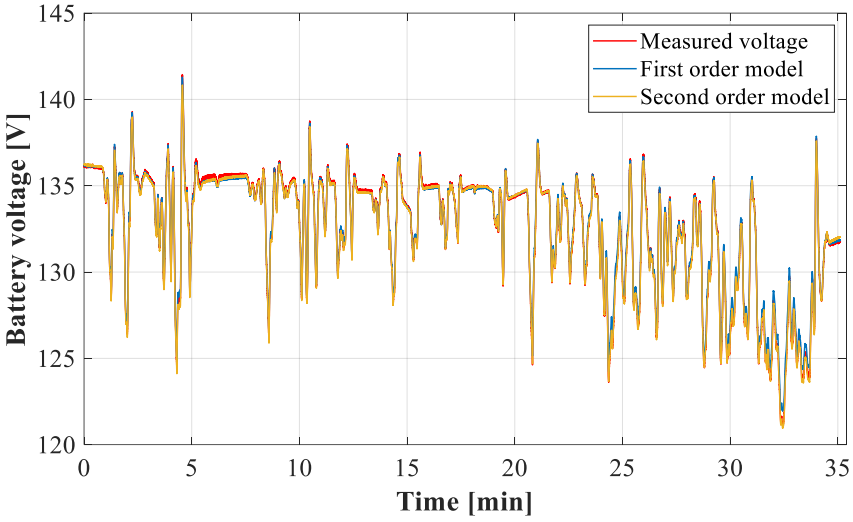

Fig.4.10. The comparison for the resulted voltages

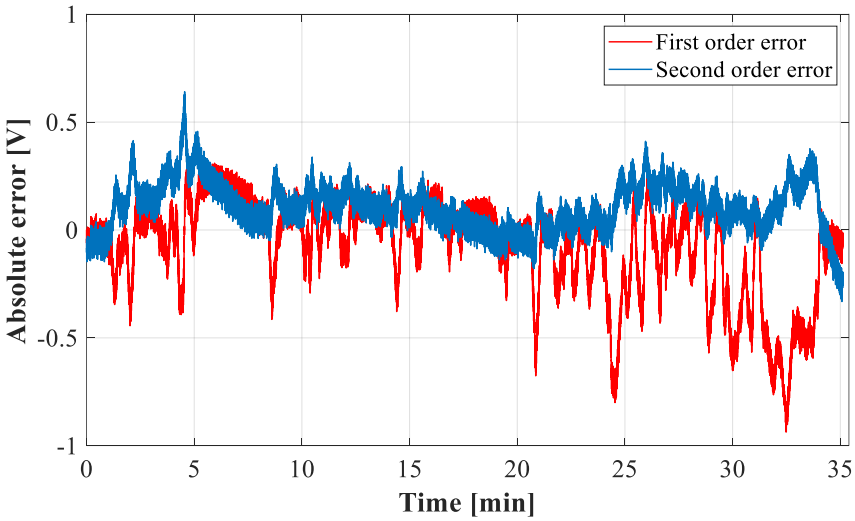

Fig.4.11. The absolute error

4.2.2. PMSM hardware-in-the-loop results

In the configuration presented in Fig. 4.12. the control of the traction motor is tested. Two identical PMSMs are mechanically coupled. One is the traction motor, right side in Fig. 4.12, and the other one is the load emulator, on the left side. The prerecorded driving cycle is sent to Amesim to the driver. The torque needed to follow the speed cycle is computed by the vehicle control unit as reference for the field-oriented torque control used for the traction motor. This is computed in MicroLabBox and transmitted through an analog output port to the NI PXIe. In the Amesim model the traction motor torque is distributed to the vehicle dynamics through a mechanical reducer. From the driving cycle, the motor speed is calculated depending on the wheel dimension and the mechanical reducer. It is then applied to the load emulator's speed control as a reference speed. From both control strategies, the switching signals are obtained for the two three-phase inverters. The common DC link of the inverters is connected to a bidirectional DC power supply. The measured signals, as feedback for the two control strategies, are the currents for each phase, the rotor position and its speed.

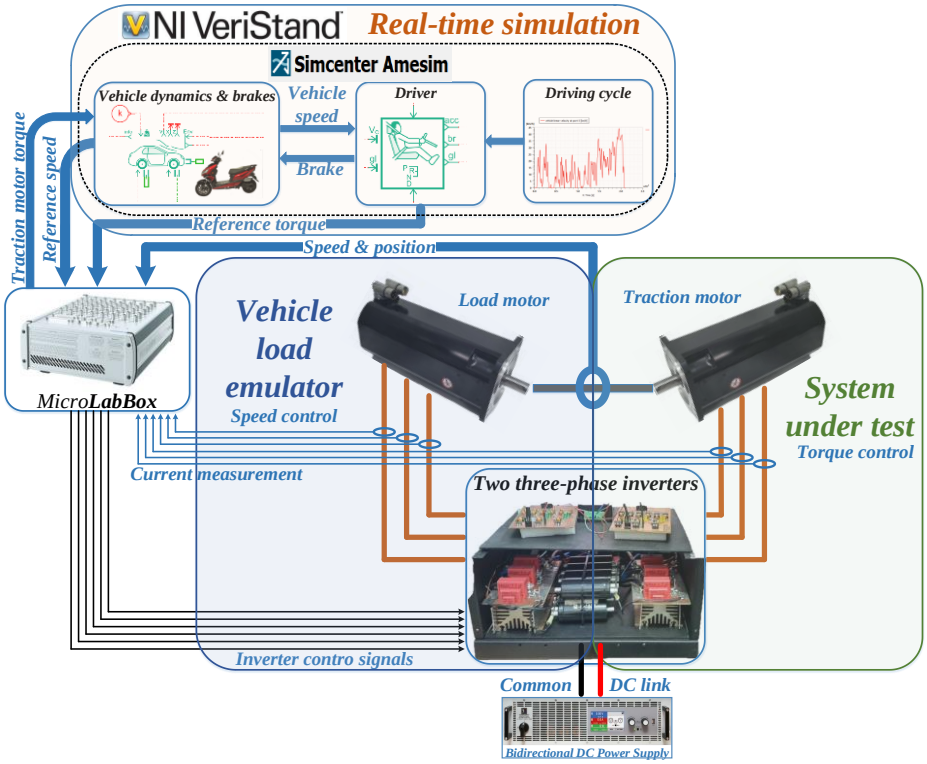

Fig.4.12. PMSM HIL scheme

The same prerecorded driving cycle was considered and thus resulting the reference speed for the load emulator. In Fig. 4.13 the reference and the measured motor speed are superimposed. The good agreement between the two highlights the correct operation of both simulated and experimentally controlled machine.

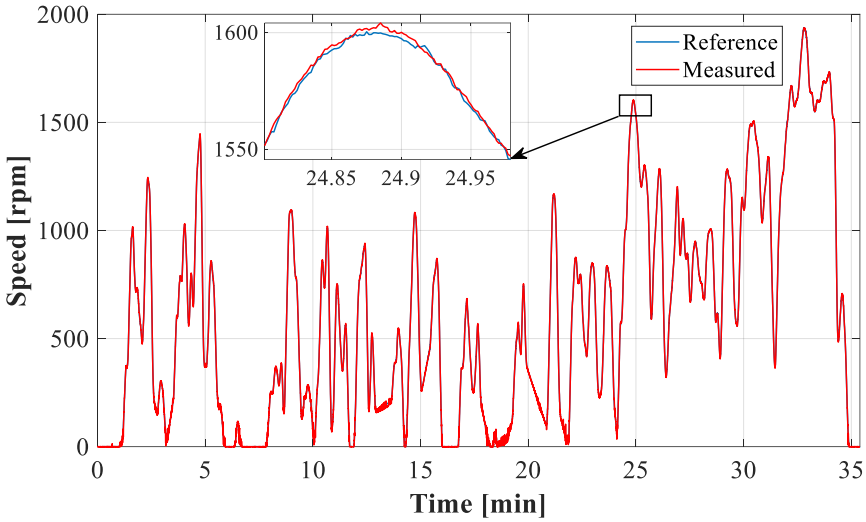

Fig.4.13. The reference and measured speed

From the reference torque computed by the vehicle control unit the reference current for the q-axis is calculated. In Fig. 4.14 the reference and measured currents on q-axis are overlapped. The reference current on d-axis is set to zero. A very good agreement can be seen between the curves in Fig. 4.14. Fig. 4.15 depicts the torque developed by the traction motor.

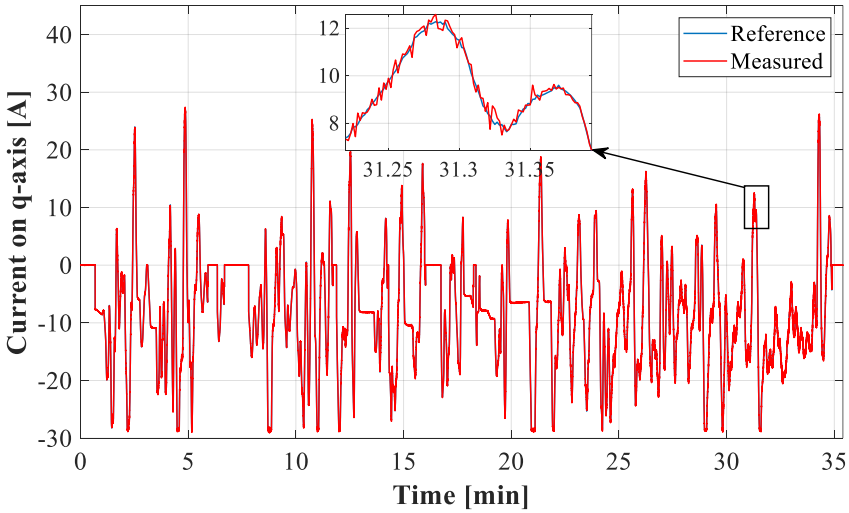

Fig.4.14. The current (reference vs. measured) on q-axis

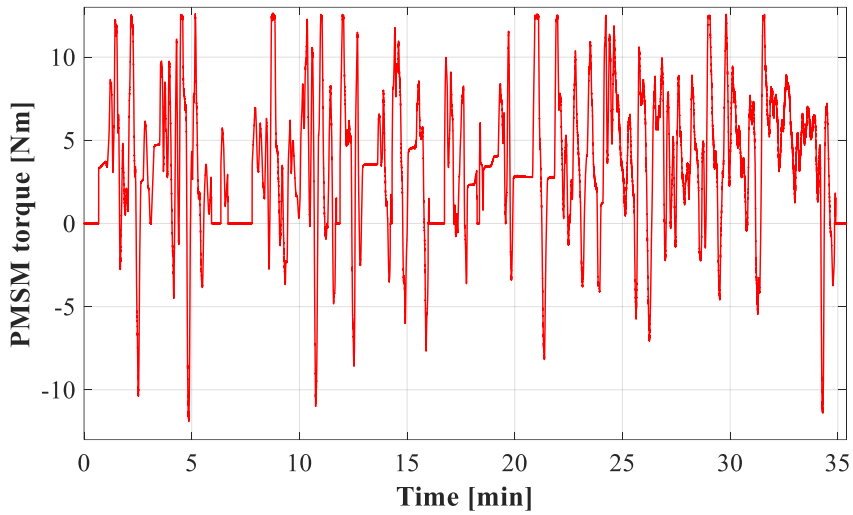

Fig.4.15. The PMSM developed electromagnetic torque

As a conclusion of analyzing the above presented results, the good functionality of the torque controller for the traction motor and the speed controller for the load emulator was experimentally proved.

4.2.3. Battery emulation hardware-in-the-loop results

In this configuration of the testing platform, the vehicle battery normally connected to the traction machine's DC link, is replaced by a bidirectional DC power supply. The voltage output of the bidirectional DC power supply is controlled from the PXIe real-time simulation, where the battery model is running. For the vehicle load emulator, the DC link is supplied by a second bidirectional DC power supply set to constant voltage. The current drained/supplied from/to the battery is calculated from the PMSM currents and supplied to the battery model. This calculation is performed in MicroLabBox and transmitted to the PXIe via an analog port as represented in Fig. 4.17. The battery model voltage variation as response to the imposed current (Fig. 4.17) is depicted in Fig. 4.18 whilethe battery state of charge for the complete driving cycle is depicted in Fig.4.19.

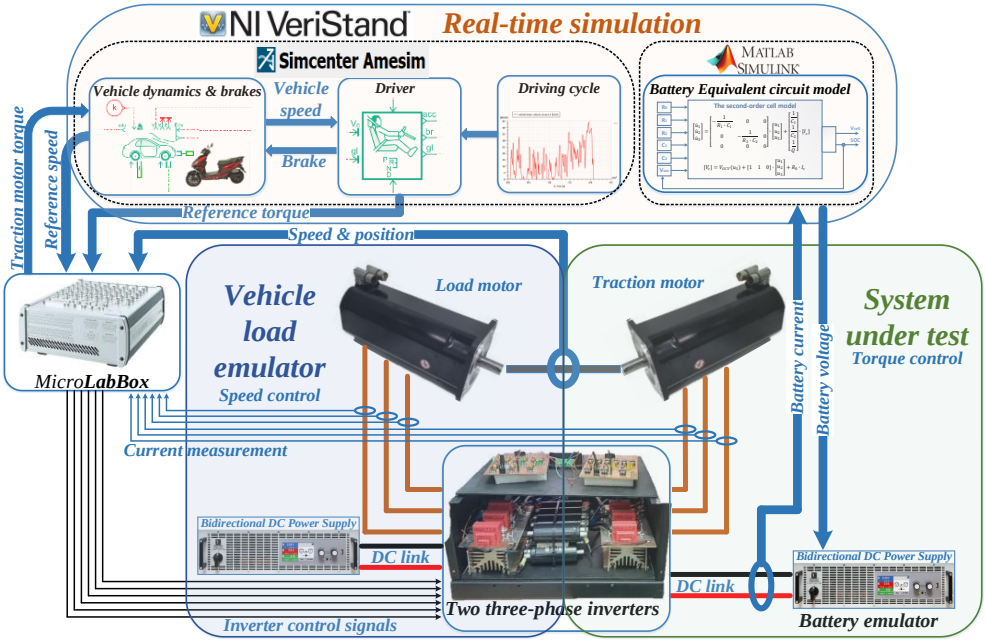

Fig.4.16. Battery emulation HIL scheme

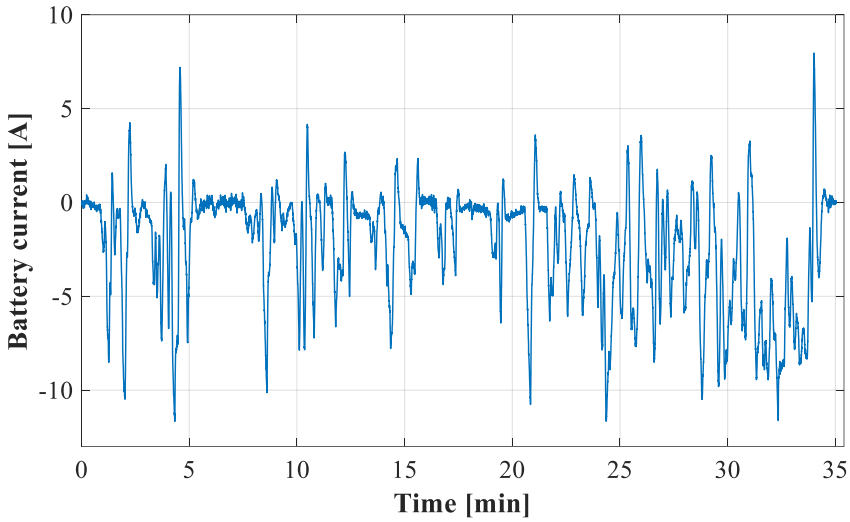

Fig.4.17. The calculated DC link current imposed to the battery model

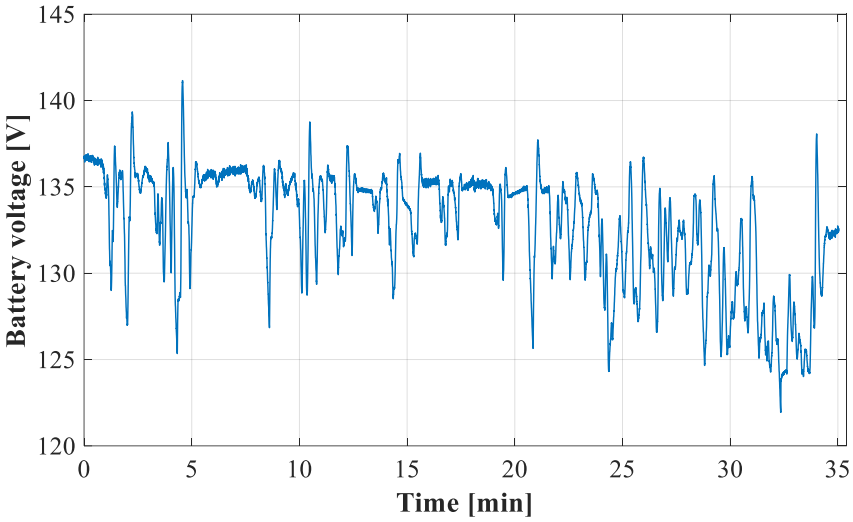

Fig.4.18. The voltage variation of the battery model

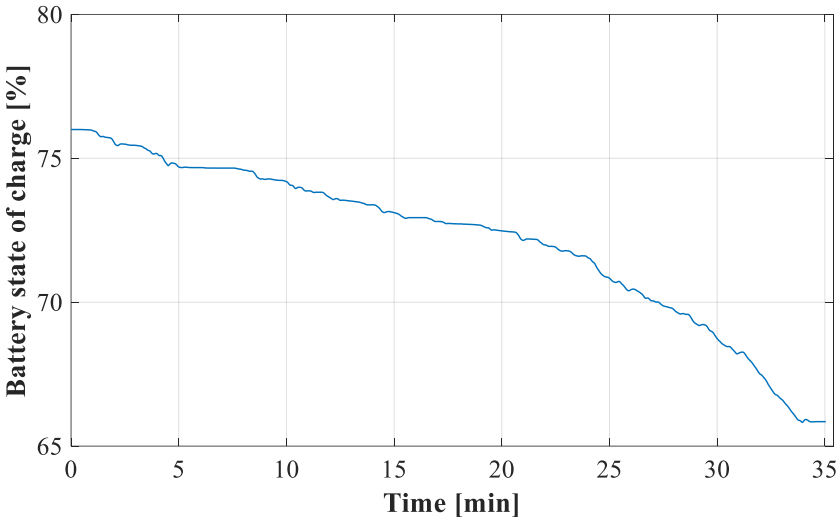

Fig.4.19. The battery state of charge

To avoid redundancy, the vehicle speed and the traction motor torque are not presented as these are identical to those detailed in the PMSM HIL results section.

4.2.4. Complete hardware-in-the-loop results

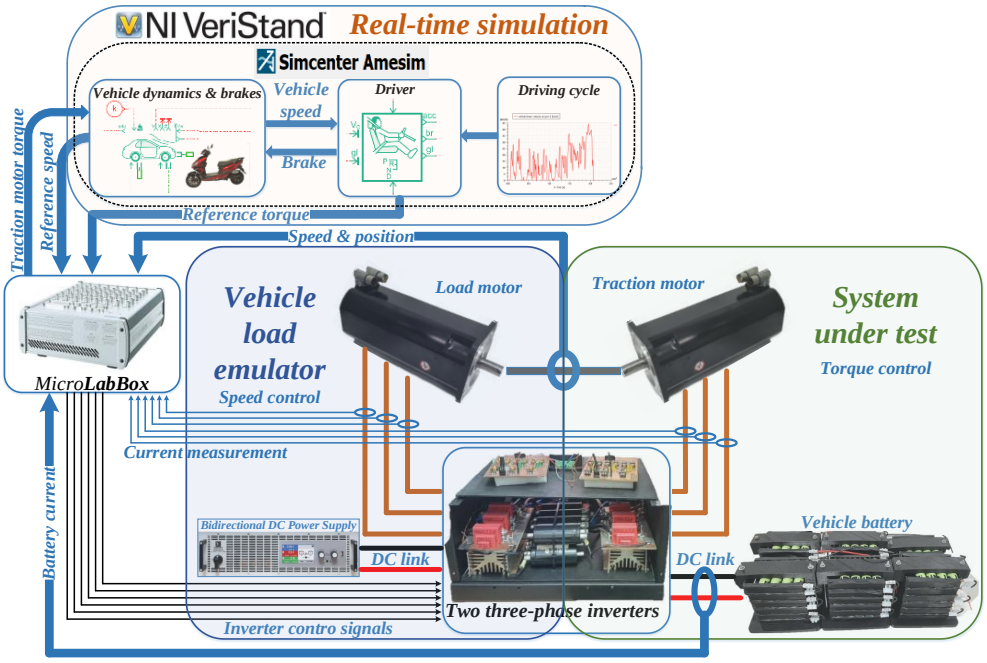

Fig.4.20. The complete HIL scheme

The complete testing facility that integrates all the hardware assemblies into a HIL system is depicted in Fig. 4.20. The 1.6 kWh Li-ion battery is connected to the DC link terminals of the traction machine three-phase inverter. The power supply for the vehicle load emulator is the bidirectional DC power supply as the traction machine is working in both regimes, motor and regenerative braking. The torque required by the scooter to track the imposed driving cycle is calculated in the Amesim model and transmitted to the torque controller in MicroLabBox as reference. From this value the reference current for q-axis is then calculated. In Fig. 4.21 the reference and measured currents for the q-axis are superimposed while Fig. 4.22 depicts the electromagnetic torque developed by the traction motor. Negligible differences can be observed between the curves of Fig. 4.21 proving correct and robust operation of the torque controller. The imposed emulator's load and measured speed variations are depicted in Fig. 4.23. Here too, similarity of the curves proves the good operation of the system. [6]

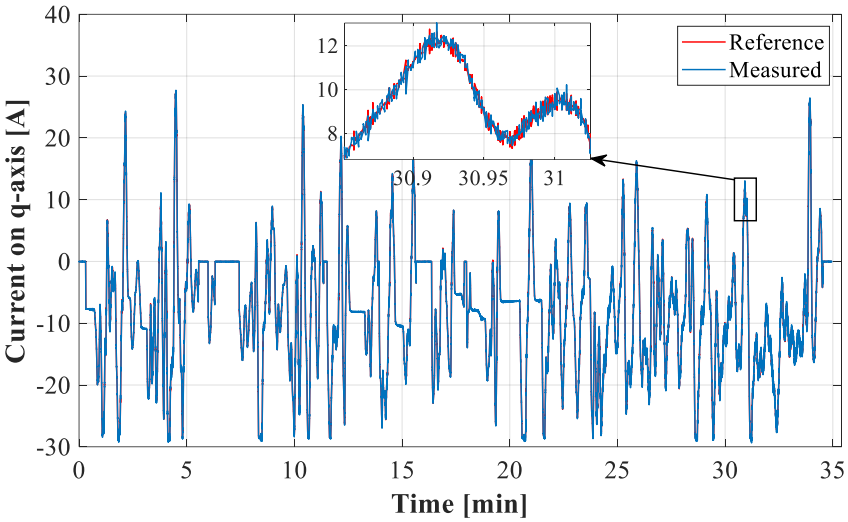

Fig.4.21. The currents on q-axis

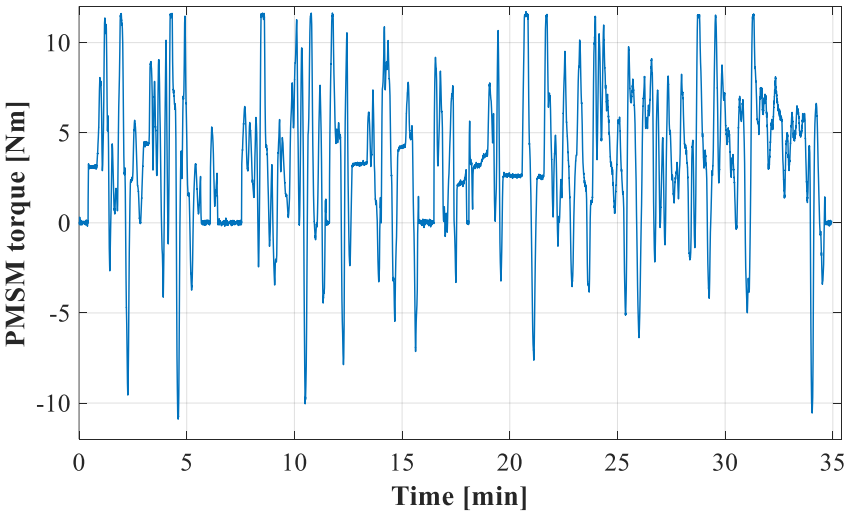

Fig.4.22. The torque developed by the traction motor

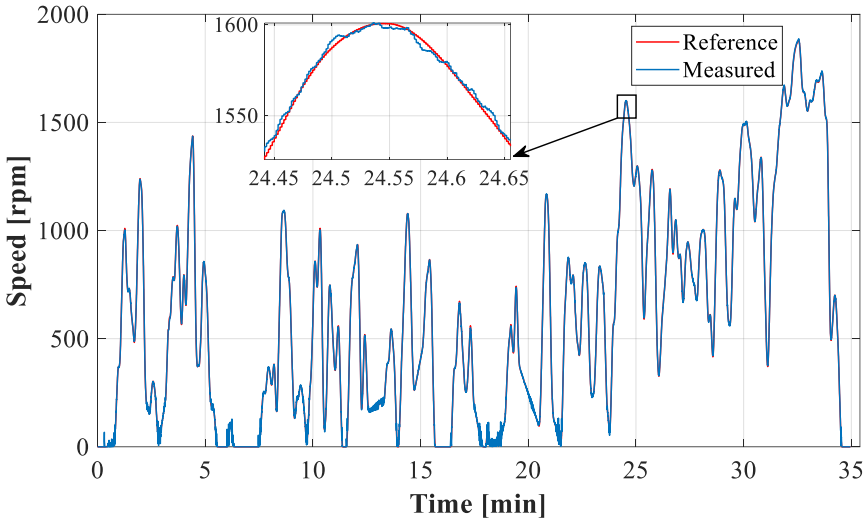

Fig.4.23. The reference and measure speeds for the PMSM 's load emulator

The current drained/supplied from/to the battery by the traction machine was measured with a current sensor being presented in Fig. 4.24. In Fig. 4.25 the measured battery voltage variation during the complete driving cycle is plotted.

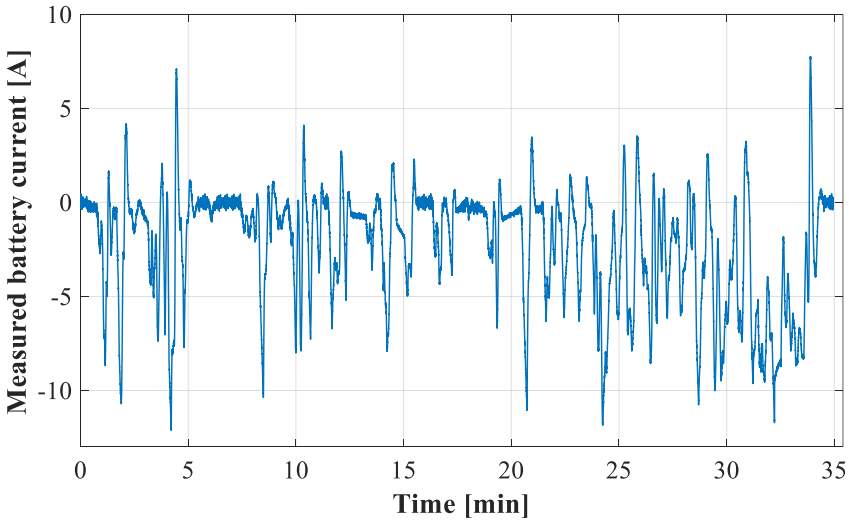

Fig.4.24. The battery current

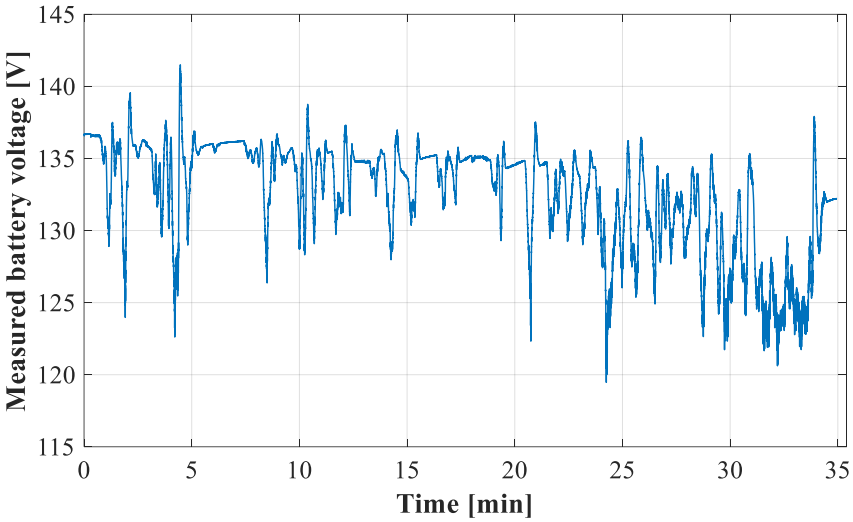

Fig.4.25. The battery voltage

4.3. Comparative analysis of the results of RTMiL vs. HIL

The last step for the platform validation is to compare the results from the real-time simulation with those measured with hardware-in-the-loop testing. The measured battery voltage and current are compared with the values obtained from the real-time simulations. In Fig.4.26 and Fig. 4.27 the current and attery voltage variations are depicted. In both figures, good overlapping of the curves can be noticed concluding that the second-order equivalent circuit model implemented in Simulink is accurate enough to be compared to the real battery.

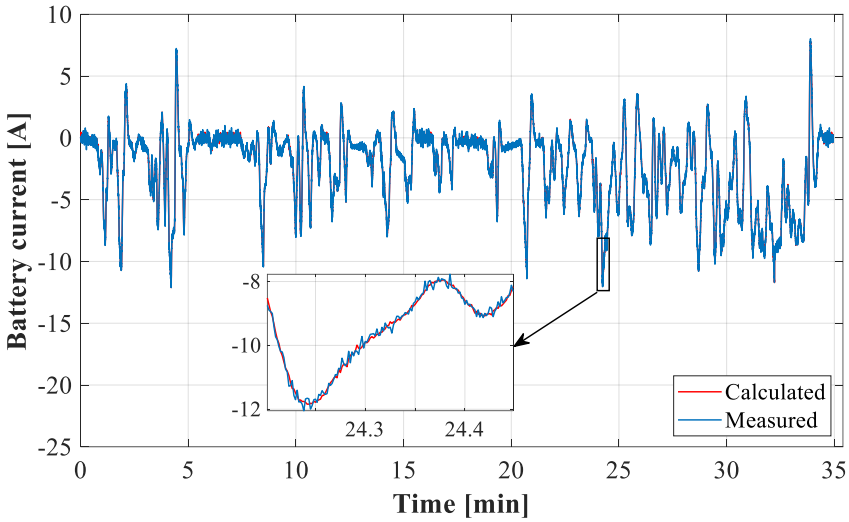

Fig.4.26. Comparison on the battery currents

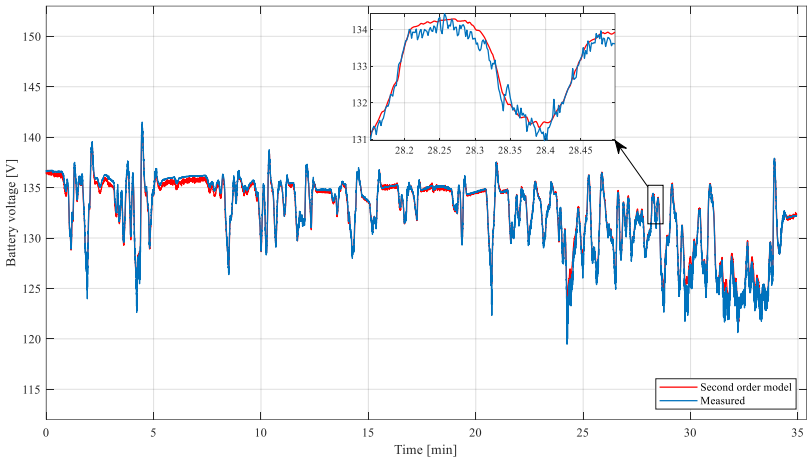

Fig.4.27. Comparison on the battery voltages

For the validation of the traction motor, the current on q-axis from the real-time simulation is compared with the current on the q-axis measured on the real test bench. The comparison between the two is depicted in Fig. 4.28. These are almost the same, the noticeable difference being the noise of the measured current where no filter is applied.

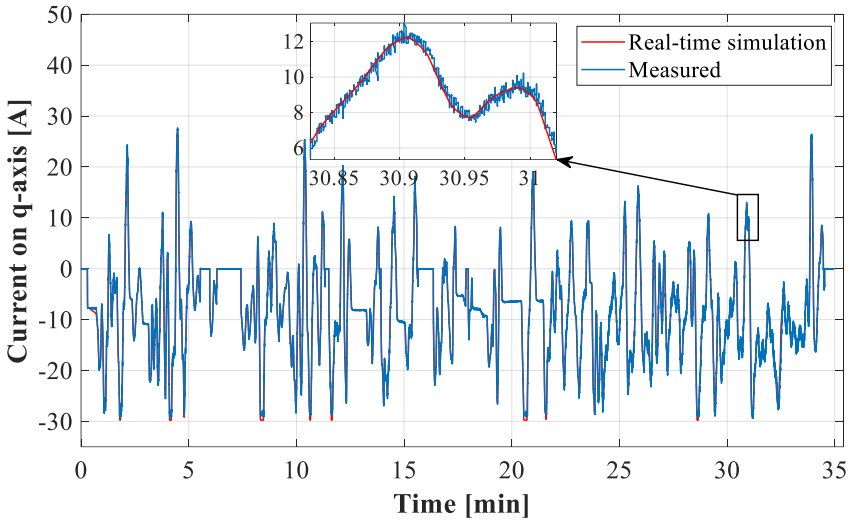

Fig.4.28. The current on the q-axis resulted from the real-time simulation vs. HIL

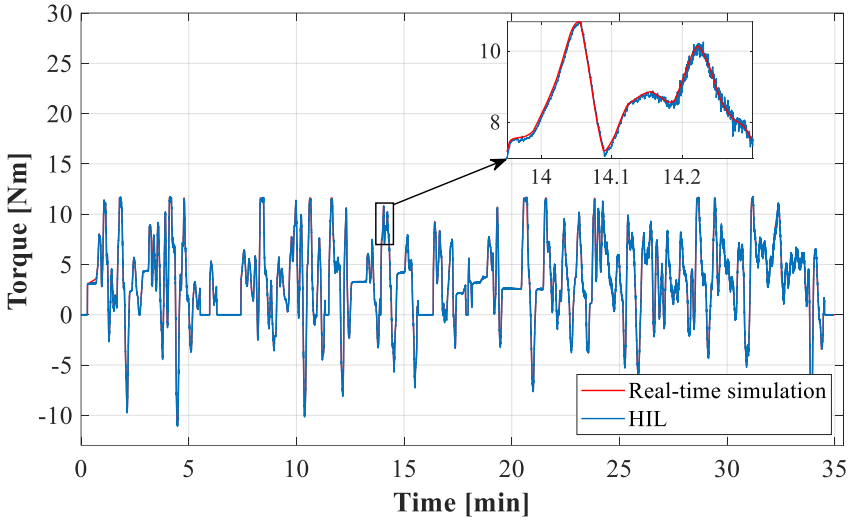

Fig.4.29. The torque of the traction motor resulted from real-time simulation and HIL

The test results detailed in this chapter prove the functionality of the platform and highlights its flexibility to shift from full simulation to partial or total HIL analysis. The transition between virtual or close to real approaches is smooth, fast, accurate and reliable. The results prove

this and not only demonstrate the lucrativeness of the developed tool but also provide information about the design and building pHILosophy of the entire system. The real-time simulation results compared to those from hardware-in-the-loop testing offer a cross validation, RTMiL proves the operational skill with HIL results and vice versa.

4.4. Conclusions

This chapter presented the real-time simulations and the results measured on the testbench. During RTMiL the complete platform simulation is tested applying a driving scenario for the electric scooter.

To validate the platform's components, each element is tested separately engaging different HiL configurations detailed in this chapter. For the final analysis, the complete HiL platform is tested, and the chapter ends with a comparison of the results obtained from RTMiL and HiL. Based on the presented results both the simulations and the platform's functional skills and perfromances are validated.

REFERENCES

1. Raul-Octavian Nemes, Sorina-Maria Ciornei, Mircea Ruba, Claudia Maris, "Real-time simulation of scaled propulsion unit for light electric vehicles", Springer Electrical Engineering Journal Online, 2019, doi:10.1007/s00202-019-00773-1

2. S. Ciornei, R. Nemeş, M. Ruba, C. Husar, H. Hedeşiu and C. Marţis, "Real-Time Simulation of a Complete Electric Vehicle Based on NI VeriStand Integration Platform," 2018 International Conference and Exposition on Electrical And Power Engineering (EPE), Iasi, 2018, pp. 0107-0112.doi: 10.1109/ICEPE.2018.8559919

3. R. Nemeş, S. Ciornei, M. Ruba, C. Marţiş and H. Hedeşiu, "Urban light electric vehicle real-time model architecture using VeriStand Software," 2021 IEEE 19th International Power Electronics and Motion Control Conference (PEMC), doi: 10.1109/PEMC48073.2021.9432634.

4. M. Ruba, R. Nemeş, S. Cionei, C. Marţiş, “Parameter identification, modelling and testing of batteries used in electric vehicles”, chapter of " Applied Electromechanical Devices and Machines for Electric Mobility Solutions”, DOI: 10.5772/intechopen.89256

5. R. O. NEMES, S. Maria CIORNEI, M. RUBA and C. MARTIS, "Parameters identification using experimental measurements for equivalent circuit Lithium-Ion cell models," 2019 11th International Symposium on Advanced Topics in Electrical Engineering (ATEE), Bucharest, Romania, 2019, doi: 10.1109/ATEE.2019.8724878.

6. M. Ruba, S. Ciornei, R. Nemeş and C. Martis, "Detailed Design of Second Order Model of Lithium-Ion Battery Simulator Based on Experimental Measurements," 2019 11th International Symposium on Advanced Topics in Electrical Engineering (ATEE), Bucharest, Romania, 2019, doi: 10.1109/ATEE.2019.8724890.

7. T. Moldovan, R. Inţe, R. O. Nemeş, M. Ruba and C. Marţiş, "Typhoon HIL Real-Time Validation of Permanent Magnet Synchronous Motor’s Control," 2021 9th International Conference on Modern Power Systems (MPS), 2021, pp. 1-6, doi: 10.1109/MPS52805.2021.9492619.

5. Conclusions, contributions, and future work

The global challenge is the reduction of the total greenhouse gas emissions. In Europe the transport sector represents a quarter of the total emissions and within the sector the road transport is the biggest emitter, more than 70%. The main areas for action are the efficiency increasing of the transport system, accelerating the deployment of low-emission alternative energy, and moving towards zero-emission vehicles.

The goal for a low or zero emissions transportation can be achieved by the electric and hybrid vehicles integration. The integration will have a negative impact on the existing power grid, and this is an important research subject treated in many papers.

The manufacurers competition now is for a continuously development of new and more efficient hybrid and full electric electric propulsion systems. For this development high accuracy simulations and testing platforms are used. All the propulsion components are highly optimized to reach the maximum efficiency.

The perspective created in this study proved with theoretical and experimental results underlines the benefits of a genuine platform for EV research, development, testing and optimization available for any OEMs involved in such activities. The "X"-iL philosophy in which it was developed ensures utility on any power, complexity, hardware availability and knowledge scale. The flexibility to transition from MiL, SiL, PiL, or RTMiL to HiL, the ease of usage and the accuracy of the results, strengthens the benefits of using it, ensuring reduced time to market by fast and low-cost development process. The latter ones are attributes of large interest nowadays in the competitive EV industry. The thesis proved concepts developed using certain hardware and software tools, however not these are of interest, but the engineering philosophy built and proved with them.

In the following sections the main contributions of the thesis are presented and, in the end, the future work.

5.1. Contributions

In the second chapter of the thesis the simulation models for each component of the platform are detailed. Two simulation softwares are used, MATLAB/Simulink and Simcenter Amesim and a third software, NI VeriStand, to link the two and run on the real-time processor.

First the dynamic model of the electric scooter was implemented in Amesim and the main parameters are listed. Next the drive train assemblies are presented, starting with the Li-ion cell model. For the cell different equivalent electrical circuit models are described and two are presented in detail including the identification procedure, the model parameters extraction and the two models validation. Moving forward the passive and active cell balancing methods are presented and a novel cell balancing circuit has been built and tested in this section. For the balancing circuit a patent was issued. The chapter continues with the model of the three-phase voltage source inverter, the permanent magnet synchronous machine used as traction motor and the field-oriented control. The tunning process of PI controllers is detailed, and the complete control is validated by comparing the simulation results with the test bench measurements.

The third chapter presents the development of the hardware-in-the-loop testing facility. The design of the three-phase inverter starts with the requirements that must be met by the components that are used to build the inverter. The gate drive and resistance, the bootstrap components, and the current measurement circuit are detailed in this section. The complete schematic and the PCB circuit of the inverter are designed in the Altium Designer software. After the building process, some testing protocols are applied to the inverter to validate the good functionality and the testing results are depicted. First, each leg was tested separately using different loads. The next test was in H-bridge configuration and for the last test the complete inverter. The chapter continues with the design of the novel active cell balancing circuit. Automotive relays are used to switch between the cell for this demonstrator balancing circuit because the purpose was to prove the balancing concept and there were no space constraints. Here the circuit for the relay control and the cell voltage

measurem circuit are presented. Next, the identification circuit is detailed, and the chapter ends with the battery unit configuration.

The fourth chapter has been focused on the experimental results. The chapter starts with the real-time model in the loop results. In this configuration the MATLAB/Simulink and Amesim models are coupled using NI VeriStand and simulated on a real-time processor. The simulation results are depicted.

Moving forward the hardware-in-the-loop (HIL) tests are detailed, starting with the battery-in-the-loop configuration of the platform. In this test only the battery is tested on the test-bench and the rest of the platform is simulated. The objective of this test is to validate the two equivalent circuit battery models by comparing the simulation results with the measured ones on the real battery. The results of the comparison and the errors are detailed.

In the next HIL test the field-oriented torque control applied on the traction motor and the speed control applied to the load emulator are tested. Both PMSM's share the same DC-link, supplied by a bidirectional DC power supply. Each machine is connected to a three-phase inverter and the power switching elements are controlleg from the Mico LabBox controller. The reference torque and speed applied to the two control strategies are obtained from the Amesim simulation. Next the results are depicted and prove the correct behaviour of the two control strategies.

For the next test setup, the real battery used to supply the traction motor is replaced by a battery emulator. This emulator is a bidirectional power DC power supply controlled via the analog input port by the PXIe real-time simulator where the simulated battery model is running. The load machine is supplied by a second bidirectional DC power supply. In this configuration the battery can be tested in extreme conditions to see the behaviour without demage to the real battery.

The last test configuration was the complete platform hardware-in-the-loop, where only the vehicle dynamic model is running in the real-time simulation, the rest of the components are connected on the test-bench. The Li-ion battery is connected to the traction motor three-phase

inverter and for the load emulator was used a bidirectional DC power supply.

The chapter ends with a comparative analysis of the real-time simulation results and the measurements obtained in the hardware-in-the-loop testing. The real-time model in the loop simulation is validated and based on the presented results, high accuracy was obtained.

The most significant contributions of this work to the actual status of research are listed below:

- The speed and torque control algorithms were implemented in simulation and validated on the testbench using the MicroLabBox.
- A PI regulator tunning process using the system transfer function for the speed and current regulators was carried out.
- A back-to-back configuration with two three-phase inverters was designed and builded to be used to supply the traction and the load machine.
- The measurement circuit used for the Li-Ion cell identification procedure was designed, implemented, and tested.
- A novel active cell balancing circuit was developed, implemented, and validated for five cells.
- The identification procedure and the balancing logic was developed using the LabView software and implemented with National Instruments hardware.
- Complete experimental validation of the simulation models/results for different components of the scooter powertrain was carried out.
- The complete hardware-in-the-loop platform implemented and tested was the final outcome of the present study.

5.2. Future Work

The testing platform developed in this thesis proves to be a promising tool for the electric propulsion power train testing. The testing facility can be improved in many directions and these can be some future research subjects.

For the battery unit to increase the accuracy of the model the thermal model can be added, and the state of health can be estimated. The battery

state of charge can be better estimated using the impedance spectroscopy method or using the adaptive systems (back propagation (BP) neural network, radial basis function (RBF) neural network, etc.) because the Coulomb counting method used in this work is highly susceptible to errors.

The control of the traction machine can be improved by applying the predictive torque control. The sensorless control can be implemented to reduce the total cost of the electric propulsion solution. A fault tolerant algorithm can be applied to eliminate the risks if the current measurement is faulty.

The dynamic model of the vehicle developed in Amesim can be upgraded. The energy consumption of the auxiliary systems of the electric vehicle can be added.

LIST OF FIGURES

LIST OF TABLES

Software applications used in the study

MATLAB/Simulink – general description

Simcenter Amesim – general description

NI LabView – general description

NI VeriStand – general description

Altium Designer – general description

APPENDICES

Appendix A. The three-phase inverter details

A.1. Driver circuit

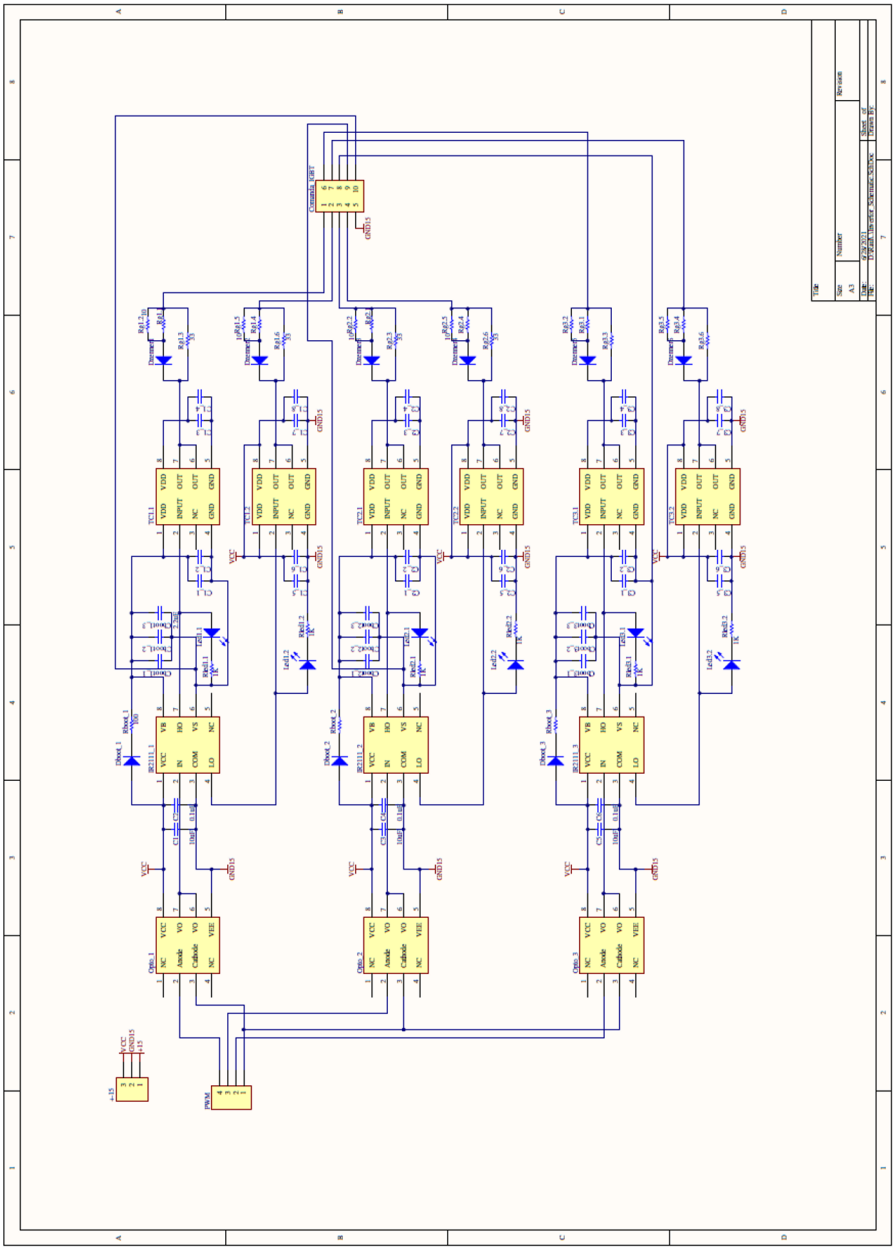

Fig. A.1 The driver schematic

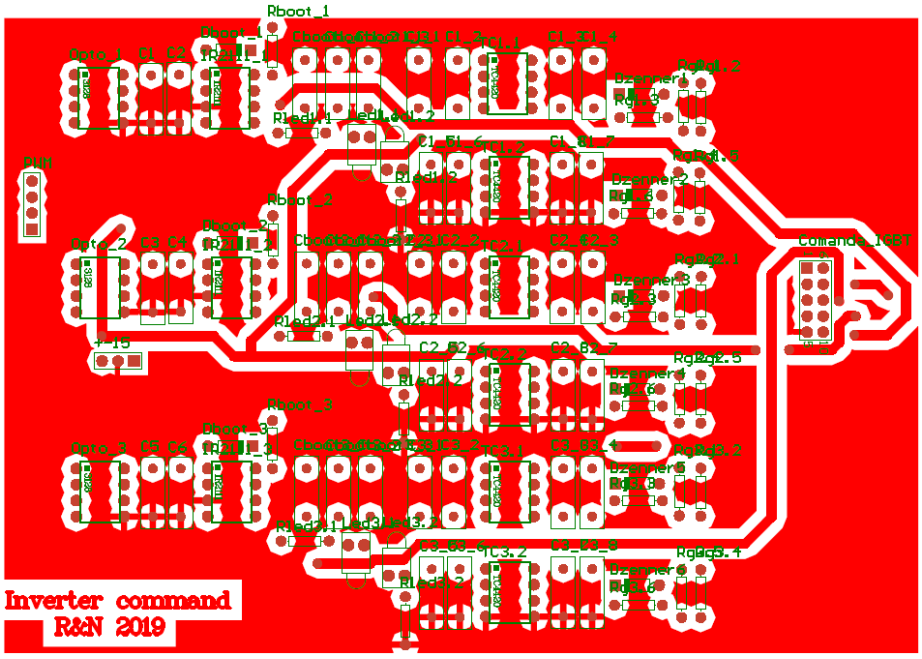

Fig. A.2 Driver PCB design's top view

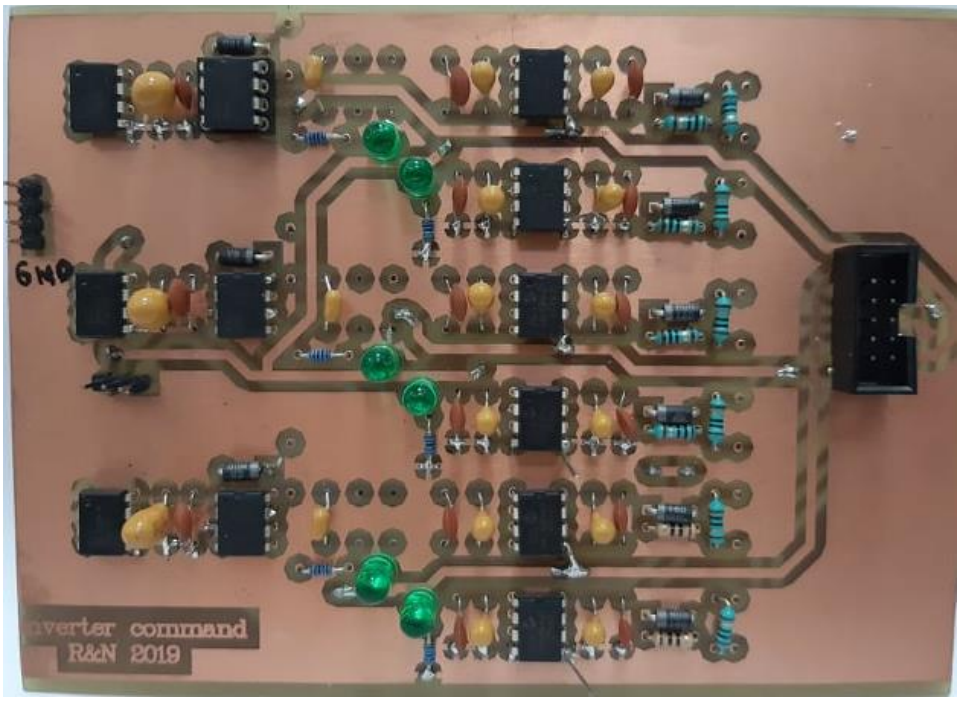

Fig. A.3 The driver circuit top view

A.2. The inverter's power stage

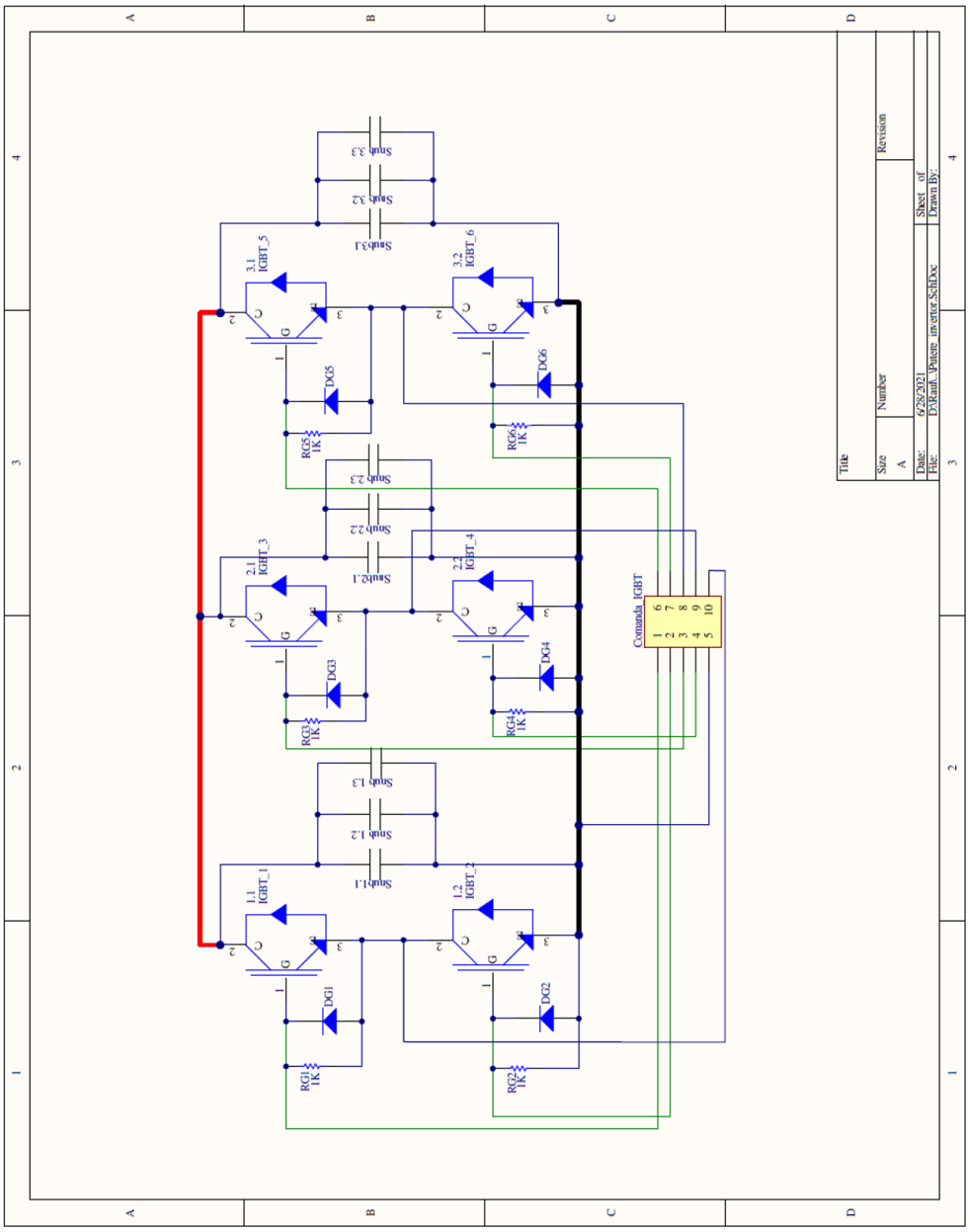

Fig. A.4 The power stage schematic

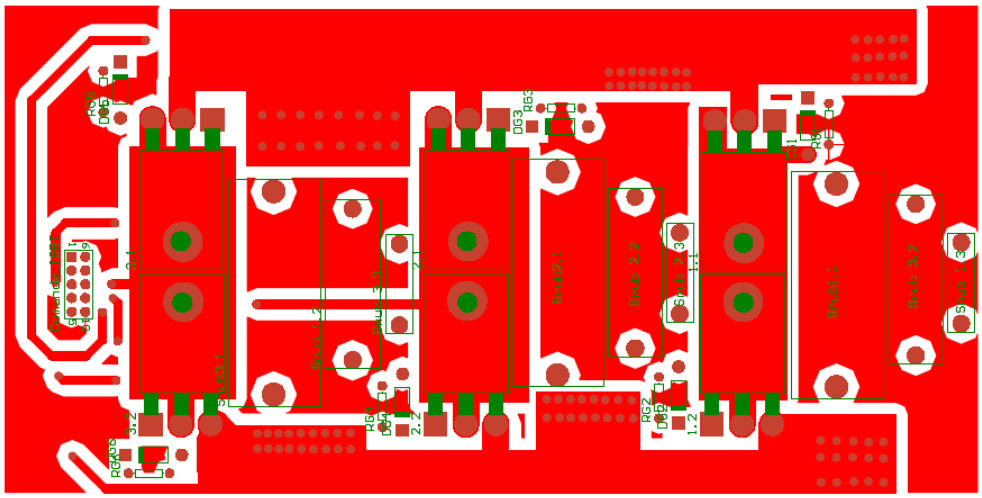

Fig. A.5 The power stage circuit PCB's top view

Fig. A.6 The power stage of the inverter with the DC link capacitors

A.3. The current and voltage measurement circuit

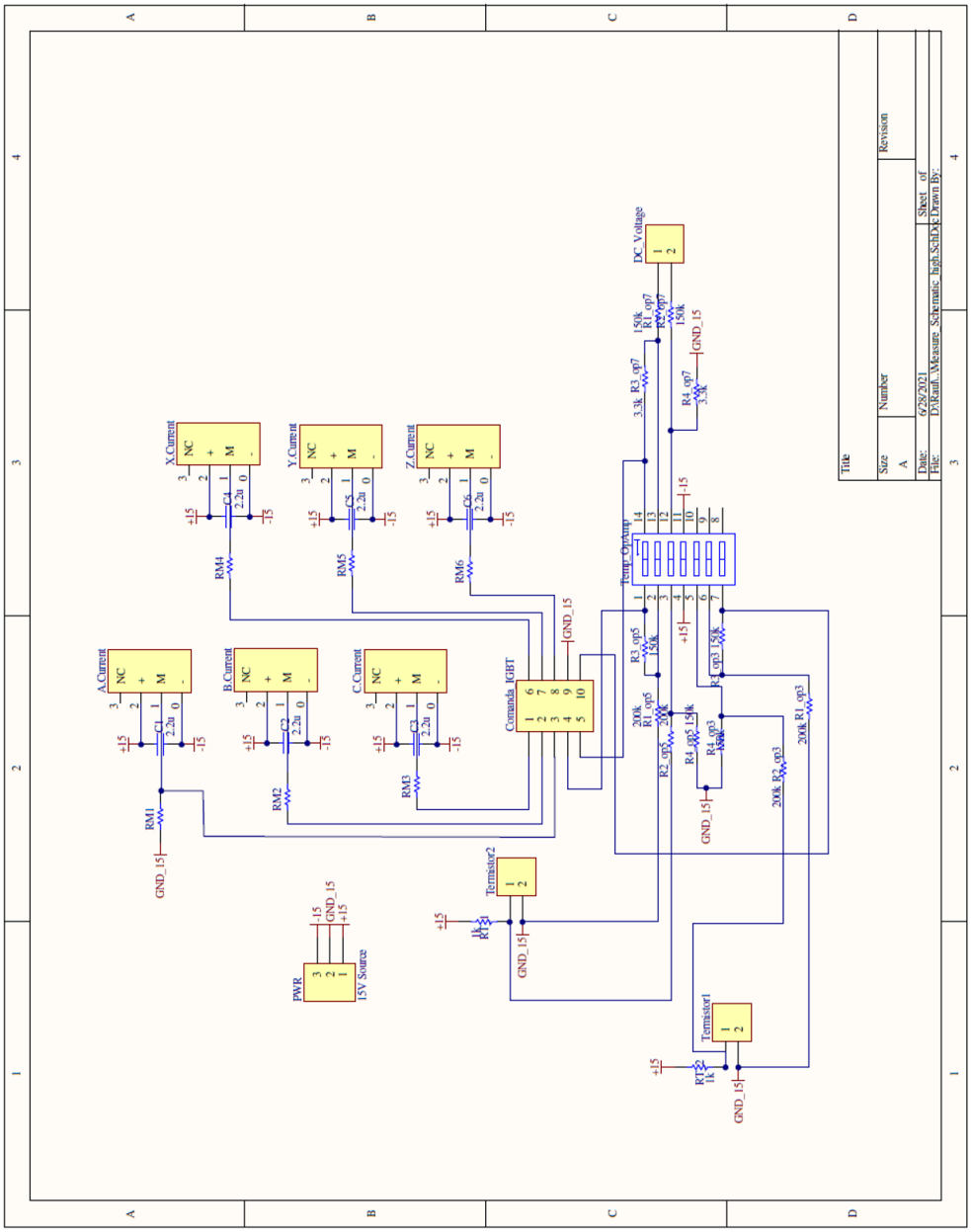

Fig. A.7 The measurement circuit's schematic

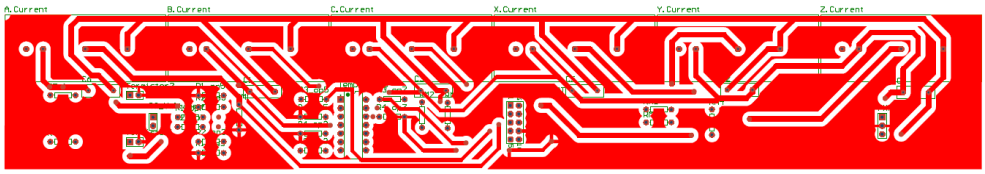

Fig. A.8 The measurement circuit's PCB design

Appendix B. The balancing circuit

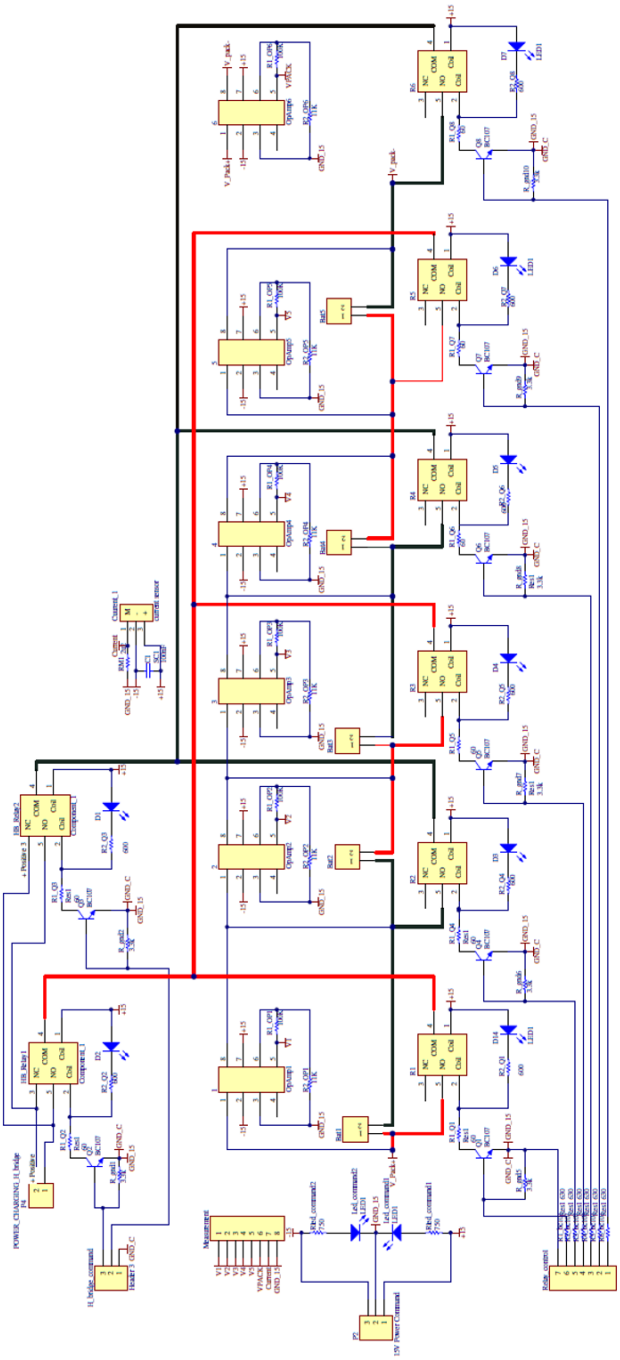

Fig. B.1 The schematic of the balancing circuit

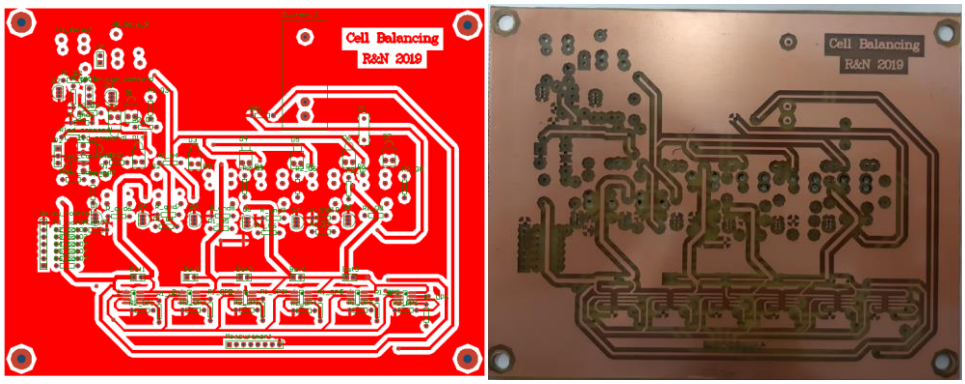

Fig. B.2 The PCB design for the balancing circuit

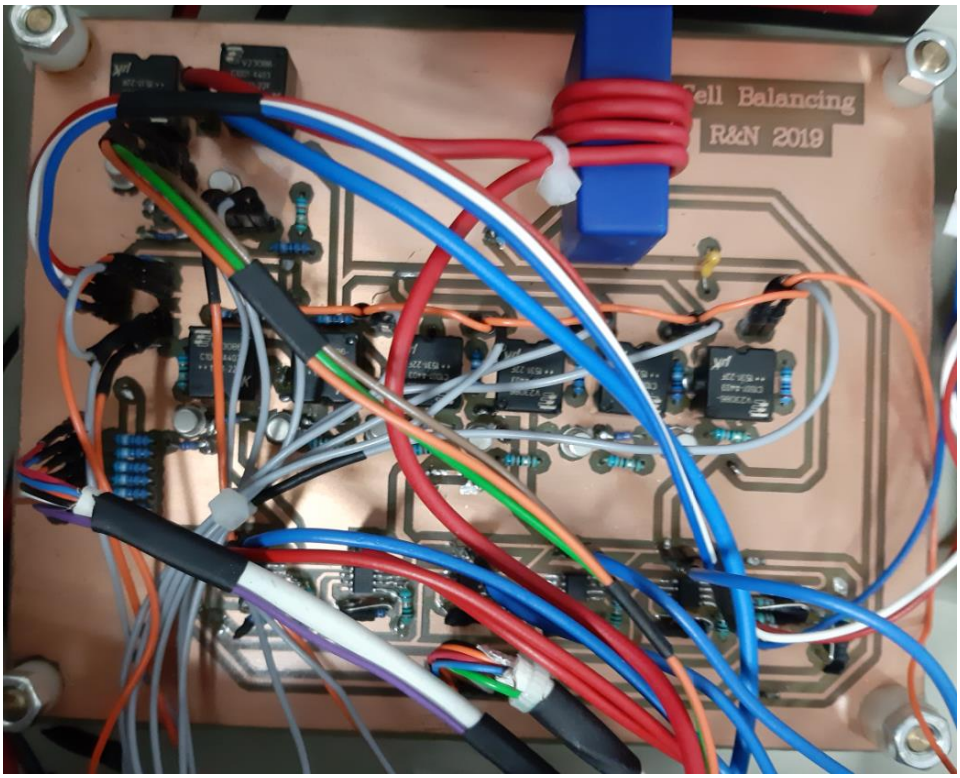

Fig. B.3 The complete cell balancing circuit

Appendix C. The cell parameters identification circuit

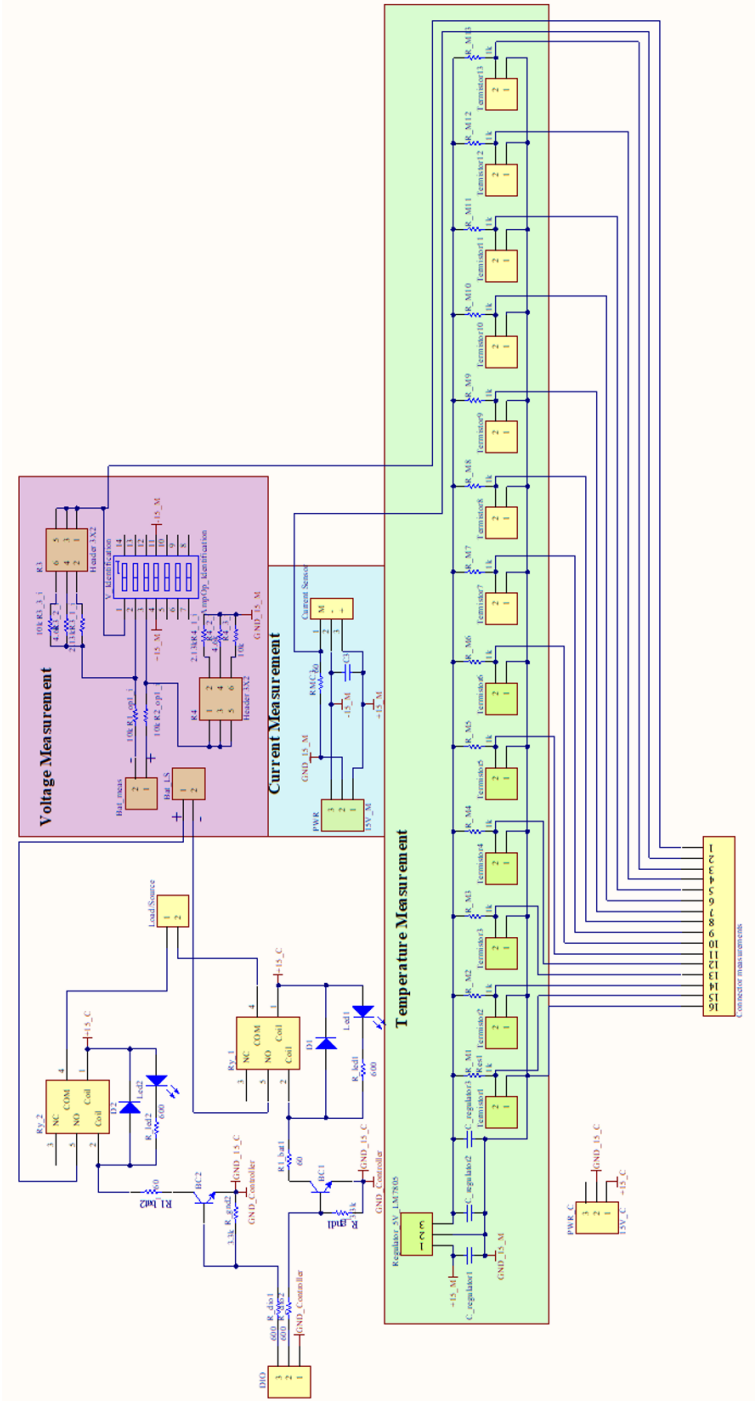

Fig. C.1 The cell parameters identification schematic circuit

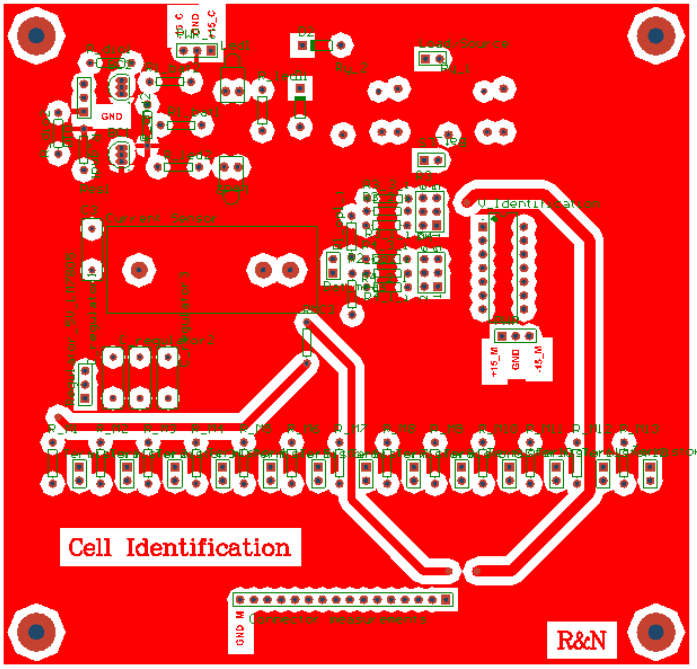

Fig. C.2 The cell parameters identification PCB design

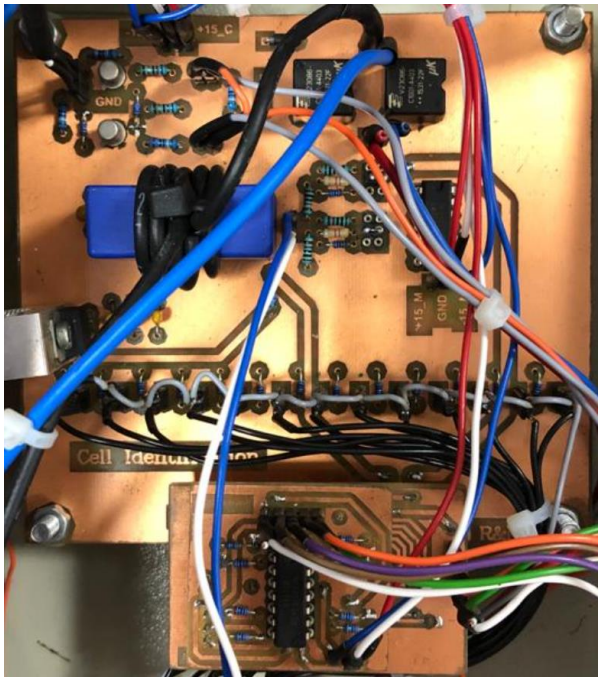

Fig. C.3 The built circuit for cell parameters identification

Appendix D. The battery pack

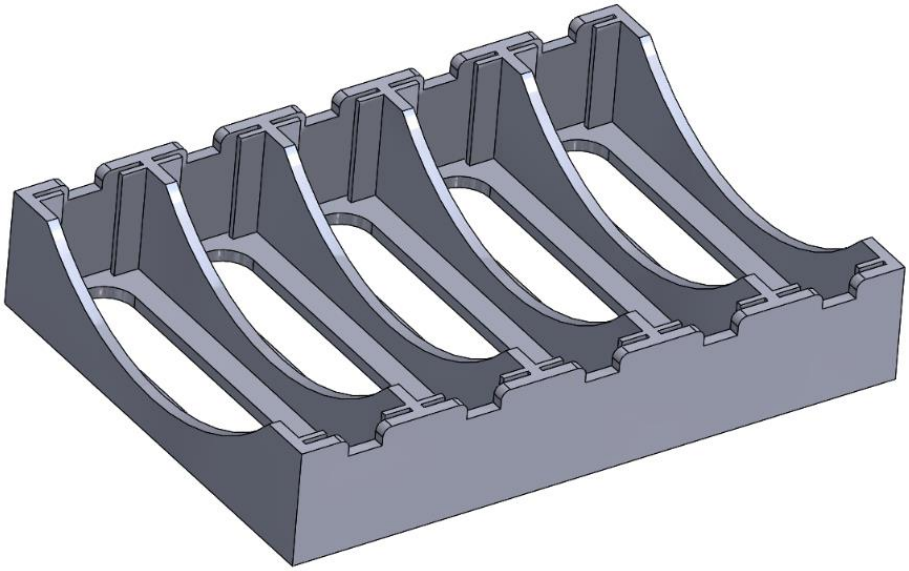

Fig. D.1 The plastic cell support for parallel connection

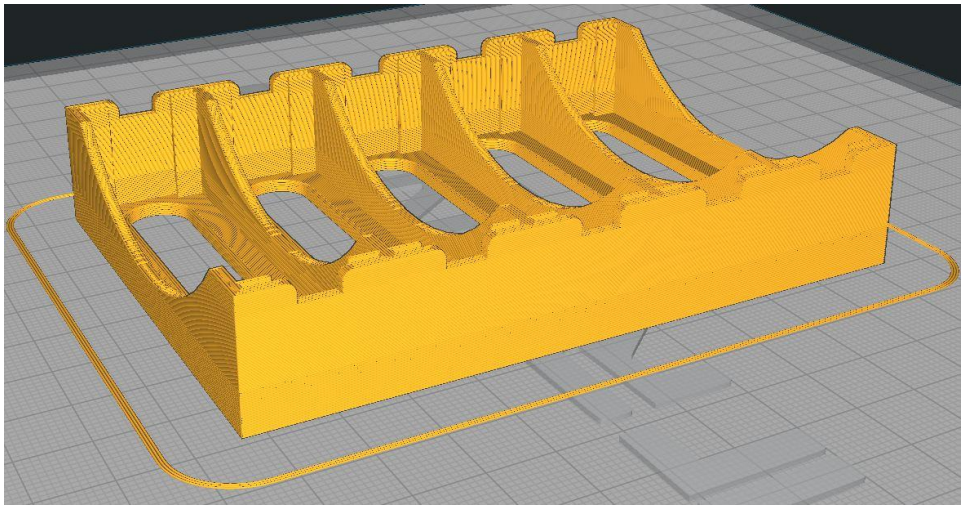

Fig. D.2 The cell support for parallel connection - 3D printer version

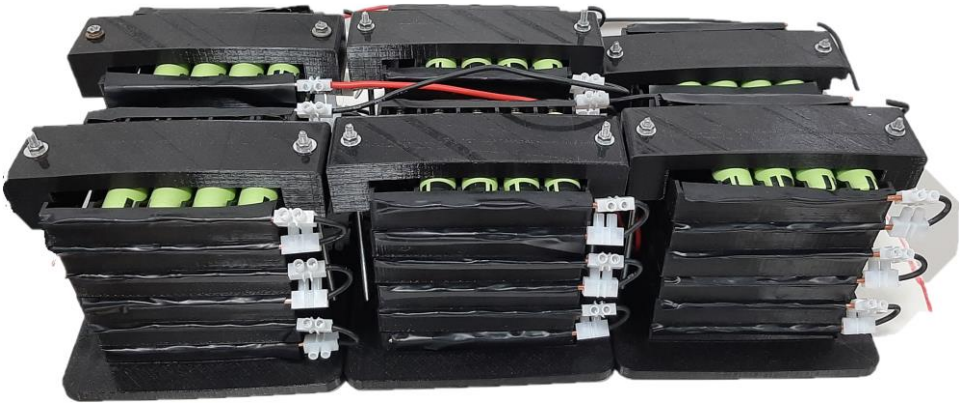

Fig. D.3 The complete battery pack for the electric scooter

LIST OF PUBLICATIONS

Year 2017

1 S. Ciornei, **R. Nemeş**, M. Ruba, H. Hedeşiu and C. Marţiş, "Real-time FPGA simulator for electric vehicle power supply systems," 2017 International Conference on Optimization of Electrical and Electronic Equipment (OPTIM) & 2017 Intl Aegean Conference on Electrical Machines and Power Electronics (ACEMP), Brasov, 2017, pp. 983-988.doi: 10.1109/OPTIM.2017.7975098

2 M. Ruba, **R. Nemes** and C. Martis, "FPGA Based Real-Time Electric Power Assisted Steering Motor-Drive Simulator Designed for HiL Testing in the Automotive Industry," 2017 IEEE Vehicle Power and Propulsion Conference (VPPC), Belfort, 2017, pp. 1-6.doi: 10.1109/VPPC.2017.8331024

Year 2018

1 **R. Nemeş**, S. Ciornei, M. Ruba and C. Martis, "Real-time simulation of scaled propulsion unit for light electric vehicles," 2018 ELEKTRO, Mikulov, 2018, pp. 1-6.doi: 10.1109/ELEKTRO.2018.8398345

2 M. Ruba, **R. Nemes**, F. P. Piglesan, H. Hedesiu and C. Martis, "Complete elecric power steering system real-time model in the loop simulator," 2018 ELEKTRO, Mikulov, 2018, pp. 1-6.doi: 10.1109/ELEKTRO.2018.8398354

3 M. Ruba, F. P. Pigleşan, **R. Nemeş**, H. Hedeşiu and C. Marţiş, "Comparison of electric power steering assistant motor structures using real-time model in the loop analysis," 2018 IEEE International Conference on Automation, Quality and Testing, Robotics (AQTR), Cluj-Napoca, 2018, pp. 1-6.doi: 10.1109/AQTR.2018.8402756

4 S. I. Cosman, M. Dranca, **R. Nemeş** and C. Marţiş, "Design, Building and Testing a High Voltage-Low Current Drive for SRMs Used for Automotive Applications," 2018 IEEE International Conference on Environment and Electrical Engineering and 2018 IEEE Industrial and Commercial Power Systems Europe (EEEIC / I&CPS Europe), Palermo, 2018, pp. 1-6.doi: 10.1109/EEEIC.2018.8494503

5 P. P. Florin, R. Mircea, **N. Raul**, C. Martis and P. Adrian-Cornel, "Real-time Model in the Loop analysis of PMSM for electric power steering system based on FPGA implementation," 2018 International Symposium on Power Electronics, Electrical Drives, Automation and Motion (SPEEDAM), Amalfi, 2018, pp. 1358-1363.doi: 10.1109/SPEEDAM.2018.8445395

6 **R. Nemes**, M. Ruba and C. Martis, "Integration of Real-Time Electric Power Steering System Matlab/Simulink Model into National Instruments VeriStand Environment," 2018 IEEE 18th International Power Electronics and Motion Control Conference (PEMC), Budapest, 2018, pp. 700-703.doi: 10.1109/EPEPEMC.2018.8521888

7 **R. Nemes,** M. Ruba, S. Ciornei, H. Hedesiu, C. Martis and C. Husar, "Real-Time Co-simulation of Electric Power Steering System," 2018 International Conference and Exposition on Electrical And Power Engineering (EPE), Iasi, 2018, pp. 0103-0106.doi: 10.1109/ICEPE.2018.8559877

8 S. Ciornei, **R. Nemeş,** M. Ruba, C. Husar, H. Hedeşiu and C. Marţis, "Real-Time Simulation of a Complete Electric Vehicle Based on NI VeriStand Integration Platform," 2018 International Conference and Exposition on Electrical And Power Engineering (EPE), Iasi, 2018, pp. 0107-0112.doi: 10.1109/ICEPE.2018.8559919

Year 2019

1 **Raul-Octavian Nemes**, Sorina-Maria Ciornei, Mircea Ruba, Claudia Maris, "Real-time simulation of scaled propulsion unit for light electric vehicles", Springer Electrical Engineering Journal Online, 2019, doi:10.1007/s00202-019-00773-1

2 M. Ruba, S. Ciornei, **R. Nemeş** and C. Martis, "Detailed Design of Second Order Model of Lithium-Ion Battery Simulator Based on Experimental Measurements," 2019 11th International Symposium on Advanced Topics in Electrical Engineering (ATEE), Bucharest, Romania, 2019, doi: 10.1109/ATEE.2019.8724890.

3 **R. O. NEMES**, S. Maria CIORNEI, M. RUBA and C. MARTIS, "Parameters identification using experimental measurements for equivalent circuit Lithium-Ion cell models," 2019 11th International Symposium on Advanced Topics in Electrical Engineering (ATEE), Bucharest, Romania, 2019, doi: 10.1109/ATEE.2019.8724878.

4 M. Ruba, **R. Nemeş**, S. Cionei, C. Marţiş, "Parameter identification, modelling and testing of batteries used in electric vehicles", chapter of " Applied Electromechanical Devices and Machines for Electric Mobility Solutions", DOI: 10.5772/intechopen.89256

5 **R. Nemes**, S. Ciornei, M. Ruba, H. Hedesiu and C. Martis, "Modeling and simulation of first-order Li-Ion battery cell with experimental validation," 2019 8th International Conference on Modern Power Systems (MPS), Cluj Napoca, Romania, 2019, doi: 10.1109/MPS.2019.8759769

6 S. M. Ciornei, M. Ruba, **R. O. Nemes**, C. Husar and C. Martis, "Modeling. control and simulation of a light electric vehicle propulsion system based on EMR," 2019 AEIT International Annual Conference (AEIT), Florence, Italy, 2019, pp. 1-6. doi: 10.23919/AEIT.2019.8893394

7 M. Ruba, **R. O. Nemes**, S. M. Ciornei, C. Martis, A. Bouscayrol and H. Hedesiu, "Digital Twin Real-Time FPGA Implementation for Light Electric Vehicle Propulsion System Using EMR Organization," 2019 IEEE Vehicle Power and Propulsion Conference (VPPC), Hanoi, Vietnam, 2019, pp. 1-6. doi: 10.1109/VPPC46532.2019.8952428

Year 2020

1 M. Ruba, **R. O. Nemeş**, S. M. Ciornei and C. Marţiş, "Simple and Robust Current Sensor Fault Detection and Compensation Method for 3-Phase Inverters," in IEEE Access, vol. 8, pp. 34820-34832, 2020. doi: 10.1109/ACCESS.2020.2974769

2 S. Ciornei, R. Nemeş, M. Ruba, C. Marţiş and H. Hedeşiu, "Performance analysis of urban light electric vehicle propulsion system's multi-level modelling," 2020 IEEE International Conference on Automation, Quality and Testing, Robotics (AQTR), Cluj-Napoca, 2020, doi: 10.1109/AQTR49680.2020.9129938.

3 S. M. Ciornei, M. Ruba, **R. O. Nemeş** and C. Marţiş, "Multi-level models for a light electric vehicle propulsion system using EMR organisation," 2020 International Symposium on Power Electronics, Electrical Drives, Automation and Motion (SPEEDAM), Sorrento, Italy, 2020, pp. 357-362, doi: 10.1109/SPEEDAM48782.2020.9161855.

4 C. Husar, M. Grovu, C. Irimia, M. Ruba, S. Ciornei and **R. Nemes**, "Simulation of a Fuel Cell Hybrid Electric Minibus under Simcenter Amesim," 2020 International Conference and Exposition on Electrical And Power Engineering (EPE), Iasi, Romania, 2020, pp. 248-252, doi: 10.1109/EPE50722.2020.9305658.

5 C. Husar, C. Irimia, M. Grovu, C. Martis, S. Ciornei and **R. Nemes**, "Model based design of an Urban Electric Minibus," 2020 International Conference and Exposition on Electrical And Power Engineering (EPE), Iasi, Romania, 2020, pp. 242-247, doi: 10.1109/EPE50722.2020.9305539.

Year 2021

1 **R. Nemeş,** S. Ciornei, M. Ruba, C. Marţiş and H. Hedeşiu, "Urban light electric vehicle real-time model architecture using VeriStand Software," 2021 IEEE 19th International Power Electronics and Motion Control Conference (PEMC), 2021, pp. 292-297, doi: 10.1109/PEMC48073.2021.9432634.

2 M. Ruba, **R. Nemeş**, S. Ciornei, C. Marţiş and H. Hedeşiu, "A review on analytical methods for multilevel simulation of urban light electric vehicles," 2021 IEEE 19th International Power Electronics and Motion Control Conference (PEMC), 2021, pp. 377-382, doi: 10.1109/PEMC48073.2021.9432513.

3 **Raul Nemeş**, Mircea Ruba, Claudia Steluta Martis, Radu A. Munteanu, "Sensorless Field-Oriented Control MRAS Based of Interior Permanent Magnet Synchronous Motor with MTPA ", ACTA ELECTROTEHNICA, Volume 61, Number 4, 2020, ISSN 1841-3323

4 **NEMES Raul**, RUBA Mircea, CIORNEI Sorina, RAIA Raluca, MARTIS Claudia "A Survey on Multi-level Simulation Approaches for Electric Vehicle Assemblies" JOURNAL OF COMPUTER SCIENCE

AND CONTROL SYSTEMS VOLUME 14 NR 1 MAY 2021, ISSN 1844-6043

5 **Raul Octavian Nemeş**, Mircea Ruba, Sorina Maria Ciornei, Raluca Maria Raia, "Powerful Multilevel Simulation Tool for HiL Analysis of Urban Electric vehicle's Propulsion Systems", chapter of "New Perspectives on Electric Vehicles", DOI: 10.5772/intechopen.98532

6 M. R. Raia, M. Ruba, **R. O. Nemes** and C. Martis, "Artificial Neural Network and Data Dimensionality Reduction based on Machine Learning Methods for PMSM Model Order Reduction," in IEEE Access, doi: 10.1109/ACCESS.2021.3095668.

7 T. Moldovan, R. Inţe, **R. O. Nemeş**, M. Ruba and C. Marţiş, "Typhoon HIL Real-Time Validation of Permanent Magnet Synchronous Motor's Control," 2021 9th International Conference on Modern Power Systems (MPS), 2021, pp. 1-6, doi: 10.1109/MPS52805.2021.9492619.